Proceedings of the 16th International Conference on Soil Mechanics and Geotechnical Engineering

doi:10.3233/978-1-61499-656-9-47

Computational modeling of large deformations and the failure of geomaterials

Modélisation numérique des géomatériaux en grandes déformations et ruptures

Fusao Oka
Department of Civil & Earth Resources Engineering, Kyoto University, Japan

ABSTRACT

Studies on constitutive modeling and numerical analysis methods have been well developed. Nowadays, numerical and analytical methods play a very important role in Geotechnical Engineering and in a related activity called Computational Geotechnics. Due to large deformations and failure, however, several issues are encountered in Computational Geotechnics. They include constitutive modeling and its calibration, mechanical instabilities: strain localization and progressive failure, the modeling of chemo-thermo-hydro-mechanical coupled behavior, and the verification and the validation of the mathematical modeling. In the present paper, we deal with the recent progress that has been made to solve these problems, in particular, the constitutive modeling of soil for rate-dependent models with structural degradation, strain localization, liquefaction of soil and their applications in the context of large deformations and the failure of geomaterials.

RESUME

Les études sur les modèles constitutifs ainsi que sur les méthodes d'analyse numérique se sont fortement développées dans les vingt dernières années. Actuellement, les méthodes analytiques et numériques jouent un rôle très important dans l'Ingénierie de la Géotechnique et, également, dans une autre activité liée appelée la Géotechnique Numérique. Dues aux grandes déformations et à la rupture, plusieurs questions ont cependant été soulevées dans la Géotechnique Numérique. Elles incluent la modélisation constitutive et son étalonnage, les instabilités numériques : localisation des déformations et les ruptures progressives, la modélisation de comportement chemo-thermo-hydro-mécanique couplé, et la vérification et la validation de la modélisation mathématique. Le présent document porte sur les récents progrès pour résoudre ces problèmes, en particulier, la modélisation constitutive de sols pour des modèles dépendent de gradient prenant en compte la dégradation structurelle, la localisation des déformations, la liquéfaction des sols et leurs applications dans le contexte de grandes déformations et la rupture des géomatériaux.

1 INTRODUCTION

In the last two decades, studies on constitutive modeling and numerical analysis methods have been well developed. Nowadays, numerical methods play a very important role in Geotechnical Engineering and in a related activity called Computational Geotechnics. Due to large deformations and failure, however, several issues are encountered in Computational Geotechnics. They include constitutive modeling and its calibration, mechanical instabilities (strain localization and progressive failure), the modeling of chemo-thermo-hydro-mechanical coupled behavior, and the verification and the validation of the mathematical modeling. In the present lecture, we deal with the recent progress that has been made to solve these problems, in particular, the constitutive modeling of soil for rate-dependent models, strain localization and liquefaction and their applications in the context of large deformations, and the failure of geomaterials. Other problems are presented in the report on the State-of-the-Art report by TC34 of ISSMGE (2005).

1. Constitutive modeling of geomaterials and its calibration
2. Mechanical instabilities, namely, strain localization and progressive failure
3. Coupled effects of internal pore-fluid flow and the large deformations of geomaterials: Chemo-thermo-hydro-mechanically coupled analysis
4. Reconsideration of conventional analyses and design methods
5. Application and advanced computational methods

1.1 *Constitutive modeling*

Various constitutive models for soil have been developed over the last four decades. In particular, many elasto-plastic models have been proposed since Cam-clay models were established by Roscoe et al. (1963, 1968). The constitutive model for soil should be able to describe all types of soil behavior. The behavior of soil is complex, however, due to its nature, i.e., its granularity, its multiphase structure, and its inhomogeneity. The typical characteristics of soil can be listed as follows:

1. Multi-phase mixture of soil particles, pore water and pore air, saturated and unsaturated soil, and effective stress
2. Elasticity and hypo-elasticity
3. Plasticity, hypo-plasticity and dilatancy characteristics
4. Rate sensitivity, viscoelasticity and viscoplasticity
5. Density dependency and confining pressure dependency
6. Strain-hardening and strain-softening characteristics
7. Cyclic deformation characteristics
8. Structural and induced anisotropy
9. Non-coaxiality
10. Deformation localization, bifurcation, and instability
11. Discontinuity
12. Degradation and the growth of microstructures
13. Inhomogeneity and nonlocality
14. Temperature dependency
15. Electric characteristics, the dieletric constant, and conductivity

Some of the characteristics have been included in the formulation of the constitutive models. In particular, elasto-plasticity and dilatancy are now included in almost all of the models. However, some of them are not well incorporated into the models. In the present lecture note, the characteristics of soil, such as rate dependency, structural degradation, and cyclic plasticity, are discussed with regard to constitutive modeling and its use in numerical analyses.

(a) Rate dependency: The time-dependent behavior of soil, manifested as creep, relaxation, and rate sensitivity, comprises indispensable factors for predicting the long-term settlement behavior of soft clay deposits, slope stability, and landslides. Rate-dependent models, such as viscoplasticity models, are overviewed. It is shown that elasto-viscoplastic models are applicable to soil.
(b) Degradation of the soil microstructures: Strain-softening behavior is due not only to strain localization, but also to material degradation. The typical degradation of geomaterials is observed for soft rock and cemented soil. In order to accurately simulate deformation behavior, in particular, shear and compressive strain localization behavior, it is necessary to account for the soil degradation, namely, the failure of the microstructures. Strain softening during shearing is a well-known type of behavior that is brought about by both material degradation and geometrical instability. A drop in stress is observed after the stress has reached its peak during the displacement control shearing of the geomaterials. Due to the strain-softening strain, localization manifests as "shear bands". In addition to that, we can observe volumetric strain localization which is referred to as "compaction bands" and which arises from the volumetric softening in porous rock and cemented soil. In addition, a diffuse mode of deformation is also taken into account. Elasto-viscoplastic models with structural degradation are presented and validated.
(c) Cyclic plasticity: Cyclic constitutive models for sand and clay are of great importance in the numerical simulation of such dynamic phenomena as liquefaction and vibrational problems. For a dynamic analysis of sand deposits, the model has to be well calibrated against the behavior of loose to dense sands.

1.2 *Strain localization and progressive failure*

It has been recognized that such strain localization as shear banding is of great importance, because it is a precursor to the failure of geomaterials. Numerical modeling methods have been developed for the analysis of post-failure behavior. In the analysis of strain localization, the prediction of the onset direction and the size of the localization zone are very important. If we take the usual approach, such as applying elasto-plastic models with strain softening, we encounter ill-posedness of the boundary value problems at hand. In the numerical analysis, the results strongly depend on the mesh size; they do not converge with mesh refinement. These defects derive from the violation of mathematical well-posedness, which requires a uniqueness of the solution and a continuous dependency of the solution on the boundary data. In order to rectify these shortcomings, several methods have been developed and used in the analysis such as:
(a) Non-local constitutive models, strain-gradient dependent models, Cosserat models, and integral type models
(b) Elasto-viscoplastic formulations and generalized elasto-viscoplastic formulations
(c) Discontinuous numerical methods, such as discontinuous FEM, DEM, DDA, etc.
(d) Introduction of pore-water pressure migration which leads to the weak removal of ill-posedness
(e) Dynamic formulation and the introduction of acceleration

For the presentation of these methods, numerical examples and comparisons with experimental or field data are shown in order to discuss the advantages and the accuracy of these approaches. Strain localization is not only observed in shear, but also under compression and/or compaction. When porous sandstone compaction bands are observed, compaction strain is localized for cemented soil and soft porous rock. The compaction bands are the result of unstable volumetric behavior.

1.3 *Coupled analysis*

Thermo-hydro-mechanical coupling is very important for predicting the behavior of the fluid contained in soil and for assessing the stability of geomaterials, i.e., slope stability, landslides, and liquefaction. Contractive soil, such as loose sand, may easily lead to liquefaction. If we consider the problem of soil-structure interaction, we may encounter a more complex coupled behavior. If the soil has dilatant characteristics, the strength of the soil will increase due to a rise in the effective stress. Thus, the existence of pore water may delay strain localization and failure. A more interesting point regarding the time-dependent behavior is the comparison between the effects of the inherent rate dependency of geomaterials and the pore-water migration. For the thermal effects, the fluidization of soil is affected by the thermal coupling in rapid flow problems such as landslides.

1.4 *Reconsideration of conventional methods*

Conventional analysis methods and design codes should be re-examined using the recent developments in new prediction methods. For example, the bearing capacity has been restudied and is compared with the conventional criteria. In addition, conventional methods of consolidation behavior are recast with respect to the unusual pore-water pressure response, etc.

1.5 *Application and advanced computational methods*

Slope stability, landslides, soil liquefaction problems, bearing capacity problems, excavation problems, and large settlement problems of the ground are major examples of when computational methods may be applied. Advanced computational methods such as FDM, FEM, BEM, Mesh Free Method, and FVM are among those that have been used.

2 ELASTO-VISCOPLASTIC COMPUTATIONAL MODELING

2.1 *Viscoelastic constitutive modeling*

The modeling of many kinds of materials has been carried out within the framework of viscoelasticity for polymers, metals, concrete, soil, and rock. The well-known linear models are the Maxwell model, the Voigt-Kelvin model, and the spring-Voigt three-parameter model. It has been reported that the linear spring-Voigt model can describe the dynamic nature of soil (Kondner and Ho, 1965; Hori, 1974). By introducing the concept of the distribution of relaxation time into the linear model, it is possible to model the wide range of time-dependent behavior of soil. Murayama and Shibata (1964) have proven the time dependency of clay in high-frequency regions by considering the distribution of relaxation time. Murayama (1983) proposed non-linear viscoelastic and viscoplastic models based on the original model (Murayama and Shibata, 1964; Sekiguchi, 1977).

Di Benedetto et al. (1997) proposed a simple asymptotic body (SAB) for the simplification of the viscoelastic model for soil which can be classified into three-parameter models. In the range of small strain, the linear viscoelastic approach is valid. However, in the range of large strain, the features include both viscoelasticity and visoplasticity. Oka, Kodaka and Kim (2004e) have succeeded in describing the behavior by a viscoelastic-viscoplastic model for clay which can explain the dynamic behavior of clay for a wide range of strain levels.

2.2 *Elasto-viscoplastic constitutive modeling*

2.2.1 *Overstress models*

To describe both the viscous nature and the plastic nature of soil, viscoplastic modeling is necessary. Perzyna (1963) proposed a viscoplastic theory which generalizes the linear theory for the

viscoplasticity theory by Hohenemser and Prager (1932). Prager and Hohenemser (1932)'s model, a linear extended viscoplastic model, is based on Bingham's fluid and plasticity model.

Yong and Yapp (1969) indicated the possibility of applying the viscoplasticity theory to the dynamic behavior of clay. Then, Adachi and Okano (1974) first proposed an elasto-viscoplastic theory for clay based on Perzyna's theory and the original Cam-clay model (1963). They assumed that the hardening parameter is an axial strain. They showed that viscoplasticity is an applicable theory to the rate-dependent behavior of water-saturated clay. However, a quantitative description had not yet been successively given with the model. Oka (1981), Adachi and Oka (1982a)'s newly proposed elasto-viscoplastic model is based on both Perzyna's model and Cam-clay model. It incorporates the assumption that in the stress state, after the completion of consolidation, the soil has not yet reached the equilibrium state, but has still been in a non-equilibrium state with the strain-hardening parameter of the inelastic volumetric strain, although the inelastic void ratio has been taken as a hardening parameter in Cam-clay model. The model is capable of describing the rate sensitivity, the creep, and the relaxation of cohesive soil, in particular, the volumetric relaxation behavior reported by Arulanandan et al. (1971).

The model is a rigorous combination of two theories, namely, Cam-clay model and Perzyna's model. However, the model has a shortcoming, namely, it cannot describe conventional accelerated creep behavior, i.e., creep failure. Professor S.Sture of the University of Colorado pointed out this shortcoming at the Int. workshop in Grenoble (Oka, 1982). Aubry (1985) experimentally showed that the critical state line is not rate sensitive. It can be understood that the rate dependency fades out at the critical state. Giving consideration to the rate independency at the critical state leads to the fact that the viscosity asymptotically becomes zero when approaching the critical state. Following the above point, Adachi, Oka and Mimura (1987) constructed an improved viscoplastic model by considering the variations in viscosity. The derived model is very capable of describing creep failure, i.e., accelerating creep behavior. The prediction obtained through this model indicates that the drop in stress is rather small in comparison to the experimental evidence on sensitive clay and natural soil during strain softening. During the strain-softening behavior of natural clay, it is observed that strain softening follows a rather large decrease in the mean effective stress. This indicates that the soil exhibits both shear and volumetric softening. In order to incorporate these features, a new model has been developed considering the degradation of soil structures and rate dependency by Kimoto (2002) and Kimoto, Oka and Higo (2004). This new viscoplastic model will be introduced in the following section.

Many other models have been proposed to describe the time-dependent behavior of soil. For the overstress models, Dafalias (1982), Katona (1984), Baladi and Rohani (1984), and Zienkiewicz et al. (1975) have proposed elasto-viscoplastic models within the framework of an overstress type of theory. Another type of overstress model has been proposed by Duvaut and Lions (1976). Although their model is linear overstress type of model, Duvaut and Lions's model is advantageous in that the plasticity model can easily be transferred into a viscoplastic one using the projection rule. Phillipes and Wu (1973)'s model is a non-linear viscoplastic model using a similar projection technique to obtain the overstress. Sawada et al. (2001) proposed a Cosserat viscoplasticity model for clay.

2.2.2 *Time-dependent viscoplastic model*

Sekiguchi (1977) proposed an elastic-viscoplastic model that clearly includes real time. Sekiguchi's model was originally proposed as a creep model which included failure. Nova (1982), Dragon and Mroz (1979), and Matsui and Abe (1985) derived time-dependent models which are called non-stationary models. It should be pointed out that these models include time and explicitly violate the principle of objectivity. Yin and Graham (1999) proposed an elasto-viscoplastic model based on the modified Cam-clay model and the flow surface.

2.2.3 *Viscoplastic model based on the stress history tensor*

Oka (1985) proposed a viscoplastic model with the stress history tensor which is based on the assumption that the state of materials depends on the stress and the stress history. He assumed that the yield function depends on the stress history tensor and not on just the current stress or the internal variables. The stress history tensor is given by the convolution integral of the stress tensor with respect to the generalized time measure which is inherent to the materials. Oka and Adachi (1985) developed an elasto-viscoplastic model using the stress history tensor for the analysis of the strain softening behavior of soft rock, and of frozen sand (Adachi et al., 1990; Oka et al., 1994c), and generalized it as the viscoplastic model (Adachi and Oka, 1995; Adachi et al., 2003, Adachi et al., 2005). This type of model can be applicable to the rate independent behavior adopting a special timemeasure for defining the stress history tensor. The application of the model is discussed in chapter 3.10.3.

2.3 *Microrheology models for clay*

The viscous behavior of clay has been analyzed in the field of Microrheology. Murayama and Shibata (1964) applied the rate process theory by Eyring (1936) to clay and derived a rheological model. Then, Singh and Mitchell (1968, 1969), and Mitchell, Singh and Campanella (1968) successfully described the creep behavior of clay based on the rate process theory. Using the rate process theory, an exponential type of non-linear flow law, between the shear force acting on each flow unit and the strain rate when the shear force is found to be larger than the thermal energy, was created.

2.4 *Adachi and Oka model*

Oka (1981), Adachi and Oka (1982a) developed an elasto-viscoplastic constitutive model for clay based on Cam-clay model and an overstress type of viscoplastic theory (Perzyna, 1963). The important assumption taken in the derivation of the model is that "At the end of consolidation, the state of the clay does not reach the static equilibrium state but is in a non-equilibrium state". In the followings, Terzaghi's effective stress is used as

$$\sigma'_{ij} = \sigma_{ij} - u_w \delta_{ij} \tag{2.1}$$

where σ'_{ij} is the effective stress and u_w is the pore water pressure.

It is assumed that the strain rate tensor consists of elastic strain rate tensor $\dot{\varepsilon}^e_{ij}$ and viscoplastic strain rate tensor $\dot{\varepsilon}^{vp}_{ij}$, such that

$$\dot{\varepsilon}_{ij} = \dot{\varepsilon}^e_{ij} + \dot{\varepsilon}^{vp}_{ij} \tag{2.2}$$

The elastic strain rate is given by a generalized Hooke type of law, i.e.,

$$\dot{\varepsilon}^e_{ij} = \frac{1}{2G}\dot{S}_{ij} + \frac{\kappa}{3(1+e_0)\sigma'_m}\dot{\sigma}'_m \delta_{ij} \tag{2.3}$$

where S_{ij} is the deviatoric stress tensor, σ'_m is the mean effective stress, G is the elastic shear coefficient, e_0 is the initial void ratio, κ is the swelling index, and the superimposed dot denotes the time differentiation.

The viscoplastic flow rule is given by

$$\dot{\varepsilon}^{vp}_{ij} = \gamma\langle\Phi_1(F)\rangle\frac{\partial f}{\partial \sigma'_{ij}}, \qquad F = \frac{f-\kappa_s}{\kappa_s} \tag{2.4}$$

$$\langle \Phi_1(F) \rangle = \begin{cases} \Phi_1(F) & : F > 0 \\ 0 & : F \le 0 \end{cases} \tag{2.5}$$

$$f = \overline{\eta}^*_{(0)} + \tilde{M}^* \ln \frac{\sigma'_m}{\sigma'^{(s)}_{my}} = 0 \tag{2.6}$$

$$\overline{\eta}^*_{(0)} = \sqrt{(\eta^*_{ij} - \eta^*_{ij(0)})(\eta^*_{ij} - \eta^*_{ij(0)})} \tag{2.7}$$

in which (0) denotes the state at the end of the consolidation, in other words, the initial state before deformation occurs. η^*_{ij} is the stress ratio tensor

$$\eta^*_{ij} = S_{ij} / \sigma'_m \tag{2.8}$$

and M^*_m is the value of $\eta^* = \sqrt{\eta^*_{ij}\eta^*_{ij}} = \sqrt{2J_2}/\sigma'_m$ ($J_2 = S_{ij}S_{ij}/2$) when the volumetric strain increment changes from compression to swelling. $\sigma'^{(s)}_{my}$ is the hardening parameter. $\dot{\varepsilon}^{vp}_{ij}$ is the viscoplastic strain rate tensor, γ is the viscosity parameter, σ_{ij} is the total stress tensor, σ'_{ij} is Terzaghi's effective stress tensor, f is the dynamic yield function, δ_{ij} is Kronecker's delta, Φ_1 is a material function which accounts for the strain rate sensitivity, $\langle\ \rangle$ is Macaulay's bracket, $F = 0$ denotes the static yield function, and κ_s is the hardening parameter.

2.5 *The extended viscoplastic model considering stress ratio dependent softening*

As mentioned above, Adachi, Oka and Mimura (1987) extended the original model to describe the acceleration creep behavior of clay by introducing a second material function into the model. Oka et al. (1994d, 1995b) studied the instability of the extended model during the undrained conventional creep process and strain localization analysis.

$$\dot{\varepsilon}^{vp}_{ij} = \gamma \langle \Phi_1(F) \rangle \Phi_2(\xi) \frac{\partial f}{\partial \sigma'_{ij}} \quad , \quad F = \frac{f - \kappa_s}{\kappa_s} \tag{2.9}$$

where Φ_2 is the second material function.

The second material function is introduced to explain that the rate dependency of clay vanishes at the failure state. In other words, the stress ratio at the failure state does not depend on the strain rate. In the present study, the following form for the second material function is adopted:

$$\Phi_2 = 1 + \xi \tag{2.10}$$

Internal variable ξ expresses the deterioration of the materials and obeys the following evolutional equation:

$$\dot{\xi} = \frac{M^{*2}_f}{G^*_2 (M^*_f - \eta^*)^2} \dot{\eta}^* \tag{2.11}$$

where M^*_f is the value of stress ratio η^* at the failure state, G^*_2 is a material parameter.

We can write Eq. (2.9) in an alternative form as

$$f - \kappa_s = \kappa_s \left[\Phi_1^{-1} \left\{ \frac{I^{vp}_2}{\gamma \Phi_2} \left(\frac{\partial f}{\partial \sigma'_{ij}} \frac{\partial f}{\partial \sigma'_{ij}} \right)^{1/2} \right\} \right] \tag{2.12}$$

where I^{vp}_2 is the second invariant of the viscoplastic strain rate tensor (stretching tensor). From Eq. (2.12), we can see that the yield function depends implicitly on both the hardening parameter and the strain rate.

2.6 *Elasto-viscoplastic model for cohesive soil considering degradation*

The prediction by the extended model with the second material function (Adachi et al., 1987) indicates that the drop in stress is rather small compared with the experimental evidence on sensitive clay and natural soil during strain softening. During the strain-softening behavior of natural clay, it is observed that strain softening follows a rather large decrease in mean effective stress. This indicates that the soil exhibits both shear and volumetric softening. In order to incorporate these features, a new model has been developed considering the degradation of soil structures and the rate dependency by Kimoto (2002), Kimoto and Oka (2004), and Kimoto and Oka (2005).

We assume an overconsolidation (OC) boundary surface which delineates the OC region ($f_b < 0$) from the normal consolidated (NC) region ($f_b \ge 0$), namely,

$$f_b = \overline{\eta}^*_{(0)} + M^*_m \ln \frac{\sigma'_m}{\sigma'_{mb}} = 0 \tag{2.13}$$

in which M^*_m is the value of $\eta^* = \sqrt{\eta^*_{ij}\eta^*_{ij}}$ when the volumetric strain increment changes from compression to swelling. σ'_{mb} is the hardening parameter.

Originally, the hardening rule for the σ'_{mb} surface was defined with respect to the viscoplastic volumetric strain. In order to describe the degradation of the material caused by structural changes, strain softening with viscoplastic strain is introduced in addition to strain hardening with viscoplastic volumetric strain as

$$\sigma'_{mb} = \sigma'_{ma} \exp\left(\frac{1 + e_0}{\lambda - \kappa} \varepsilon^{vp}_v \right) \tag{2.14}$$

$$\sigma'_{ma} = \sigma'_{maf} + \left(\sigma'_{mai} - \sigma'_{maf} \right) \exp\left(-\beta z \right) \tag{2.15}$$

where σ'_{ma} is assumed to decrease with an increasing viscoplastic strain in Eqs. (2.14) and (2.15), and σ'_{mai} and σ'_{maf} are the initial and the final values for σ'_{ma}, respectively. σ'_{mai} corresponds to the consolidation yield stress and σ'_{maf} is determined from the difference between the peak stress and the residual stress. Material parameter β controls the rate of the structural changes and z is an accumulation of the second invariant of the viscoplastic strain rate as

$$z = \int_0^t \dot{z} dt \ , \ \dot{z} = \sqrt{\dot{\varepsilon}^{vp}_{ij} \dot{\varepsilon}^{vp}_{ij}} \tag{2.16}$$

The mechanical behavior of clay at its static equilibrium state is assumed to be described by the original Cam-clay model (Adachi and Oka, 1982a). The following static yield function is used:

$$f_y = \bar{\eta}^*_{(0)} + \tilde{M}^* \ln \frac{\sigma'_m}{\sigma'^{(s)}_{my}} = 0 \tag{2.17}$$

In a similar way for OC boundary surface f_b, strain softening is defined in order to express the effect of a structural collapse through changes in $\sigma'^{(s)}_{my}$ with the viscoplastic strain, namely,

$$\sigma'^{(s)}_{my} = \left\{ n + (1-n)\exp(-\beta z) \right\} \sigma'^{(s)}_{myi} \exp\left(\frac{1+e_0}{\lambda - \kappa} \varepsilon^{vp}_v \right) \tag{2.18}$$

where $n = \sigma'_{maf} / \sigma'_{mai}$ describes the degree of structure at the initial state and β is the rate of degradation.

The decrease in $\sigma'^{(s)}_{my}$ leads to the shrinking of the static yield function according to the structural collapse.

The viscoplastic potential function is given as

$$f_p = \bar{\eta}^*_{(0)} + \tilde{M}^* \ln \frac{\sigma'_m}{\sigma'_{mp}} = 0 \tag{2.19}$$

where $\tilde{M}^*$ is assumed to be constant in the NC region. σ'_{mp} is determined automatically from the stress state in the NC region, and it coincides with σ'_{mb} in the OC region. The value varies with the current stress in the OC region as

$$\tilde{M}^* = \begin{cases} M^*_m & : NC \quad region \\ -\dfrac{\sqrt{\eta^*_{ij}\eta^*_{ij}}}{\ln(\sigma'_m / \sigma'_{mc})} & : OC \quad region \end{cases} \tag{2.20}$$

where σ'_{mc} denotes the mean effective stress at the intersection of the overconsolidation boundary surface and the σ'_m axis as

$$\sigma'_{mc} = \sigma'_{mb} \exp \frac{\sqrt{\eta^*_{ij(0)}\eta^*_{ij(0)}}}{M^*_m} \tag{2.21}$$

The viscoplastic strain rate tensor is given as the following equation based on the overstress type of viscoplastic theory (Perzyna, 1963):

$$\dot{\varepsilon}^{vp}_{ij} = \gamma \left\langle \Phi_1(f_y) \right\rangle \frac{\partial f_p}{\partial \sigma'_{ij}} \tag{2.22}$$

where the symbol $\langle\ \rangle$ is the Macaulay's bracket.

Based on the experimental results of strain-rate constant triaxial tests, material function Φ_1 is defined as

$$\begin{aligned} \gamma \Phi_1(f_y) &= C_0 \sigma'_m \exp\left\{ m' \left(\bar{\eta}^*_{(0)} + \tilde{M}^* \ln \frac{\sigma'_m}{\sigma'^{(s)}_{my}} \right) \right\} \\ &= C\, \sigma'_m \exp\left\{ m' \left(\bar{\eta}^*_{(0)} + \tilde{M}^* \ln \frac{\sigma'_m}{\sigma'_{mb}} \right) \right\} \end{aligned} \tag{2.23}$$

$$C = C_0 \exp\left(m' \tilde{M}^* \ln \frac{\sigma'_{mai}}{\sigma'^{(s)}_{myi}} \right) \tag{2.24}$$

in which C is the viscoplastic parameter corresponding to the viscoplastic strain rate at the initial stress state.

In the above formulation, we assumed that viscoplastic parameter C was scalar. However, we can generalize this assumption with a tensorial value for C such as fourth order isotropic tensor $C_{ijkl} = C_1 \delta_{ij}\delta_{kl} + C_2(\delta_{ik}\delta_{jl} + \delta_{il}\delta_{jk})$, as has been adopted by Oka (1982, 1992) and Oka et al. (2003).

2.7 *Determination of the material parameters*

There are ten material parameters for the proposed constitutive model. The procedure for determining these parameters is as follows. Initial void ratio e_0 can be obtained from tests for physical properties. Compression index λ and swelling index κ are given by the slope of the isotropic consolidation and swelling tests, respectively. Compression yield stress σ'_{mbi} is assumed to be determined from the yield point of the isotropic consolidation tests. Elastic shear modulus G_0 can be determined from the initial slope of the triaxial compression tests.

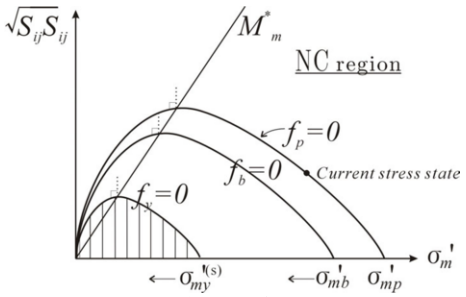

(a) NC region

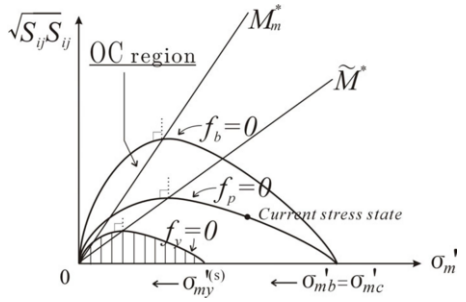

(b) OC region

Figure 2.1. Yield surface and potential surface for isotropically consolidated clay.

The stress ratio at maximum compression M^*_m is defined as the stress ratio whereby maximum compression occurs in the drained compression tests. For clay, however, it has been assumed to equal the stress ratio at the critical state. Herein, M^*_m is determined from the stress ratio at the residual state in the undrained triaxial compression tests.

Viscoplastic parameter m' can be determined from undrained triaxial compression tests with different strain rates as

$$\frac{\dot{\varepsilon}^{(1)}_{11}}{\dot{\varepsilon}^{(2)}_{11}} = \exp\left[m' \sqrt{\frac{2}{3}} \left\{ \left(\frac{q}{\sigma'_m} \right)^{(1)} - \left(\frac{q}{\sigma'_m} \right)^{(2)} \right\} \right]$$

$$m' = \sqrt{\frac{3}{2}} \frac{\ln \dot{\varepsilon}^{(1)}_{11} - \ln \dot{\varepsilon}^{(2)}_{11}}{\left(\frac{q}{\sigma'_m} \right)^{(1)} - \left(\frac{q}{\sigma'_m} \right)^{(2)}} \tag{2.25}$$

where $q\ (= \sigma'_{11} - \sigma'_{33})$ is the deviator stress, σ'_m is the mean effective stress, and superscripts (1) and (2) denote two stress

states on the stress paths with different strain rates and the same mean effective stress.

When m' is determined, viscoplastic parameter C is obtained from the deviatoric strain rate by the constitutive equation.

Alternatively, we can determine parameters m' and C through the secondary compression rate and the initial volumetric strain rate as

$$m' = \frac{\lambda - \kappa}{(1+e)\alpha} \tag{2.26}$$

$$C = \dot{\varepsilon}^{vp}_{kk(0)} / M^*_m \tag{2.27}$$

where α is a secondary compression rate, namely,

$$v^p = \alpha \ln t/t_0 + v^p_0, \quad v^p = \varepsilon^{vp}_{kk}$$

The relationship given by Eq. (2.26) can be rewritten by the secondary compression index as

$$m' = \frac{C_c - C_s}{C_\alpha} \tag{2.28}$$

where C_c is the compression index, C_s is the swelling index, and C_α is the secondary compression rate, namely, $e - e_0 = C_\alpha \log t/t_0$ in the one-dimensional consolidation tests.

When it can be assumed that $C_s = 0.1 \times C_c$, the viscoplastic parameter is approximately given as $m' = 0.9 \times C_c / C_\alpha$.

Leroueil and Hight (2003, p. 126) have shown that based on Mesri's work, C_c / C_α is between 17 - 35. For these values, m' becomes 15 - 30. m' is larger for the inorganic clay than for the organic clay. For example, Mesri et al. (1995) have experimentally obtained experimental evidence for the ratio of $C_\alpha / C_c = 0.03$ for Batiscan and Saint-Hilaire clays.

Structural parameter σ'_{maf} is determined by the decrease from the peak stress to the residual stress in the undrained tests. Structural parameter β is determined by curve fitting for the strain-softening process in the undrained tests.

2.8 *Application to Osaka pleistocene clay*

The model is applied to Osaka Pleistocene clay, namely, Kyuhoji clay. It was sampled from the upper Pleistocene layer called Ma12, which is distributed widely in the western and eastern parts of Osaka at a depth of 20 - 40 meters. This is marine clay containing diatoms, and it exhibits sensitive behavior due to the effect of the structures formed during the sedimentation process. Fig. 2.2 compares the undrained compression test results between the undisturbed and the reconstituted samples of Kyuhoji clay (Yashima et al., 1999; Shigematsu, 2002). Both the undisturbed and the reconstituted clays were sheared with an axial strain rate of 0.005% / min after isotropic consolidation at a confining pressure of 392 kPa, which is a little larger than the compression yield stress of 340 kPa. The initial void ratio of the undisturbed clay is larger than that of the reconstituted clay, specifically, 1.41 for the undisturbed clay and 1.02 for the reconstituted clay. The undisturbed clay exhibits larger strength and the deviator stress decreases after the peak stress in Fig. 2.2. Fig. 2.3 shows the results of simulations, by giving compressive strain rates under the triaxial stress state. An axial strain rate of $\dot{\varepsilon}_{11}$ = 0.005% / min is provided for the calculations. The material parameters used in the simulations are shown in Table 2.1. Structural parameter σ'_{maf} is set to be 280 kPa for the undisturbed clay, and β is set to be 10 for the undisturbed clay and 0 for reconstituted clay. β = 0 provides the original model which does not describe structural changes. The values for C contain $\sigma^{(s)}_{myi}$ concerning the degree of initial structures in the derivation. Since the degree of the initial structure of the reconstituted clay is thought to be lower than that of the undisturbed clay, a larger value for C is given for the reconstituted clay. Fig. 2.3 confirms that the proposed model can describe the difference in behavior between the highly structured and the lowly structured soil.

Table 2.1: Material parameters for Kyuhoji clay

	Undisturbed	Reconstituted
Elastic shear modulus G_0	8333 (kPa)	6330 (kPa)
Compression index λ	0.327	
Swelling index κ	0.028	
Initial void ratio e_0	1.41	1.02
Compression yield stress	$\sigma'_{mbi} = \sigma'_{mai}$ =392 (kPa)	
Stress ratio at failure M^*_m	1.22	
Viscoplastic parameter m'	21.5	
Viscoplastic parameter C	4.5×10^{-11} (1/s)	2.5×10^{-8} (1/s)
Structural parameter σ'_{maf}	280 (MPa)	392 (MPa)
Structural parameter β	10.0	0

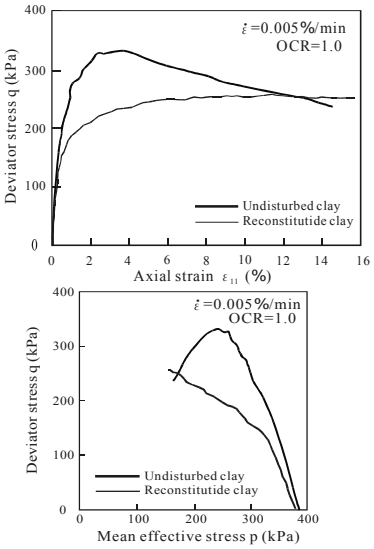

Figure 2.2. Experiments of undrained triaxial tests for Kyuhoji clay (Yashima et al., 1999).

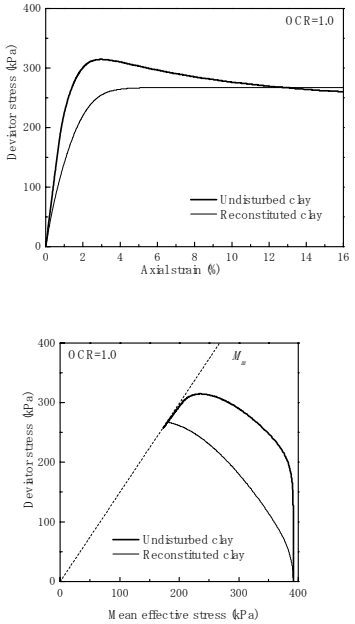

Figure 2.3. Simulations of undrained triaxial tests for Kyuhoji clay.

2.9 *Consolidation analysis*

It is well known that there are two types of time-dependent behavior for soil. One is consolidation and the other is brought about by the inherent viscous nature of the soil skeleton. The interaction between the pore water and the soil skeleton results in consolidation. The viscous properties of the soil skeleton are related to the microstructure of the soil particles. Although many problems due to the consolidation of various types of soil have been solved, some problems still exist. One of them is the interaction between the viscosity and the changes in the soil structure. In the following, two problems will be discussed. One is the influence of the soil specimen thickness on consolidation and the other is the interaction between the viscoplastic properties and the strain softening due to structural changes.

It has been reported that the influence of the specimen thickness on consolidation plays an important role in the prediction of the actual settlement due to the consolidation (e.g. Ladd et al., 1977; Aboshi, 1973; Aboshi and Matsuda, 1981; Oka et al. 1986; Leroueil, 1995; Mesri et al., 1995; Tang and Imai, 1995, etc.). As is well known, in the general report for the 9th ICSMFE, Ladd et al. (1977) showed two hypotheses for consolidation behavior by compiling the previous results (Fig. 2.4). Curve A is supported by Ladd et al. (1977) and Mesri and Rokhsar (1974). Curve B is based on the hypothesis that there is a unique strain-time relationship with respect to time-dependent characteristics and that creep deformation occurs from the beginning of the consolidation. Curve C is between Curves A and B, and appears to correspond to the experimental results of Aboshi (1973, 1995, 2004) (Fig. 2.5).

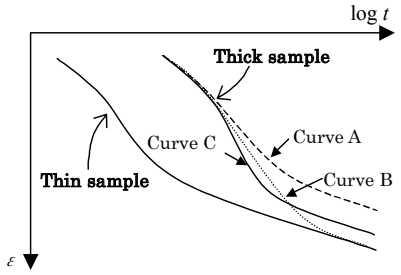

Figure 2.4. Schematic diagram of the average strain to time.

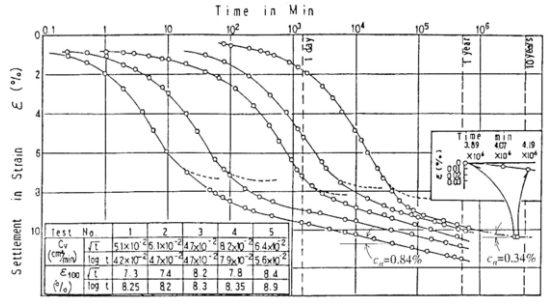

Figure 2.5. Comparison of settlement curves (Aboshi, 1973).

Many researchers have reported that the behavior which appears to be associated with the collapse of the soil structure can be recognized during the consolidation process. Bishop and Lovenbury (1969) conducted constant stress creep tests under drained conditions on undisturbed clay, and observed a sudden increase in the strain rate. Concerning field cases, the anomalous pore-pressure behavior during the consolidation of soft clay has been reported by many researchers. Mitchell (1986) reported that pore-pressure stagnation or a continuous increase after all the fill placement occurred because of a structural breakdown during compression. Furthermore, Leroueil (1988) and Kabbaj et al. (1988) observed increases in the pore water after the completion of the construction of test embankments, reflecting the fact that the effective stress temporarily diminished in the stress-strain curve. The prediction of these phenomena by numerical methods has been studied since the 1980s. Kabbaj et al. (1985) analyzed one-dimensional creep tests by the finite difference method using an elasto-viscoplastic constitutive model (Oka, 1981). They showed that the strain rate remained momentarily constant during creep simulations around the preconsolidation pressure.

In this section of the present study, one-dimensional consolidation behavior is simulated using an elasto-viscoplastic constitutive model taking into account the effect of structural degradation. We will discuss the influence of the sample thickness with respect to the soil structure and the initial strain rate.

2.9.1 One dimensional consolidation problem

One-dimensional consolidation has been numerically examined by a finite element analysis. For boundary value problems related to the soil-water coupled consolidation problem, Biot's two-phase mixture theory is adopted. The infinitesimal strain is valid for these problems since large deformations are not expected. A four-node quadrilateral element with a reduced Gaussian integration is used for the displacement, and the pore-water pressure is defined at the center of each element. The top of the specimen is set to be permeable while the bottom and the sides are set to be impermeable. The size of each element is 0.4 cm×0.4 cm for all the calculations.

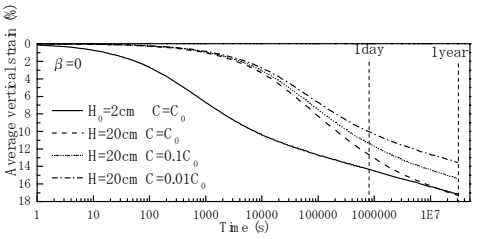

a) Average vertical strain with time

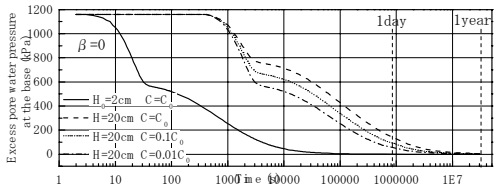

b) Generated pore-water pressure with time

Figure 2.6. Effects of parameter C (without structure β =0, C_0 =1.3×10^{-13}).

Table 2.2: Initial conditions and material parameters

Initial mean effective stress:	$\sigma'_{m(0)}$ =580 kPa
Coefficient of earth pressure:	K_0=0.5
Coefficient of permeability:	k_0=0.8×10^{-9} m/s
Permeability change index:	C_k=0.1
Elastic shear modulus:	G_0=360 kPa
Compression index:	λ =0.508
Swelling index:	κ =0.0261
Initial void ratio:	e_0=1.70
Compression yield stress:	σ'_{mbi} (=σ'_{mai})=580 kPa
Stress ratio at maximum compression:	M^*_m=1.09
Viscoplastic parameter:	m'=18.5
Viscoplastic parameter:	C=1.3×10^{-13} 1/s (=C_0)
Structural parameter:	σ'_{maf} =290 kPa
Structural parameter:	β =0, 5, 20, 40

2.9.2 Effect of sample thickness

Simulations have been performed for normally consolidated clay. The initial stress conditions of the calculations and the material parameters are shown in Table 2.2. Elastic modulus G_0 was set at 36100 kPa in the previous calculations (Kimoto, 2002), and the settlement during the first consolidation was much smaller than that obtained during the secondary consolidation. For comparison, G_0 is supposed to 360 kPa in the present study. Viscoplastic parameter C, which describes the initial viscoplastic strain rate, is set to be 1.0×10^{-13} (1/s) ($=C_0$) at first. An excess pore-pressure level of 1160 kPa, which is twice as large as the compression yield stress, is applied as the initial loading for all the analyses.

In the first calculation, viscoplastic parameter C is assumed to be C_0 for samples with different heights (H =2, 20cm). Vertical strain reaches almost the same value at 6×10^6 seconds (= 70 days). The results correspond to curve B as shown in Fig. 2.6.

In the next calculation, initial viscoplastic strain rate C is assumed to be inversely proportional to H^2, that is, $C=C_0\left(H_0/H\right)^2$ (H is the height of the specimen and H_0 is set at 2 cm). The results are shown in Fig. 2.6. The two lines (C=C_0 for H_0=2 and C=0.01C_0 for H=20) are parallel to each other; this corresponds to Curve A.

Aboshi (1973) experimentally observed that the initial strain rate for the thick sample is lower than that for the thin one. Fig. 2.5 illustrates the consolidation curves obtained by loads (19.6 - 78.4 kPa) for samples with different thicknesses (Aboshi 1973). The strains $\varepsilon_{v(0)}$ are just after the preparatory consolidation. The strain rates $\dot{\varepsilon}_{v(0)}$ are average values between consolidation stress of 9.8-19.6 kPa except No.5. For No.5, the strain rate is calculated between consolidation pressures of 0-19.6kPa (private communication with Aboshi is presented in Oka, 2000):

Specimen No.1 (H=2cm):

$\dot{\varepsilon}_{v(0)}=2.36\times10^{-3}$ %/min (9.8-19.6kPa), $\varepsilon_{v(0)}=4.7\%$

Specimen No.2 (H=4.8cm):

$\dot{\varepsilon}_{v(0)}=1.736\times10^{-3}$ %/min (9.8-19.6kPa), $\varepsilon_{v(0)}=5.3\%$

Specimen No. 3 (H=20cm):

$\dot{\varepsilon}_{v(0)}=1.05\times10^{-4}$ %/min (9.8-19.6kPa), $\varepsilon_{v(0)}=4.1\%$

Specimen No. 4 (H=40cm):

$\dot{\varepsilon}_{v(0)}=6.43\times10^{-5}$ %/min (9.8-19.6kPa), $\varepsilon_{v(0)}=5.0\%$

Specimen No. 5 (H=100cm):

$\dot{\varepsilon}_{v(0)}=7.58\times10^{-5}$ %/min (0-19.6kPa), $\varepsilon_{v(0)}=4.7\%$

As shown in the above, the initial strain rate of the thick sample just before consolidation is smaller than that of the thin sample, although the strain just after the preparatory consolidation is almost equal. The reason for the difference in strain rates is that the periods of preconsolidation are different, namely, from 1 day for the thinner sample to 4 months for the thicker one.

In the last calculation in Fig.2.6, we assumed that $C_0\left(H_0/H\right)^2<C=C_0(H_0/H)<C_0$, namely, C=0.1 C_0 for H=20. In this case, Curve C is obtained when the value of C is larger than $C_0\left(H_0/H\right)^2$ and smaller than C_0, which is consistent with Aboshi's experiments. Consequently, it was found that the effect of the sample thickness depends on the value of C, that is,

$$C=C_0\left(H_0/H\right)^2 \quad \text{(for Curve A)}$$

$$C_0\left(H_0/H\right)^2<C=C_0(H_0/H)<C_0 \quad \text{(for Curve C)}$$

$$C=C_0 \quad \text{(for Curve B)}$$

The effect of the sample thickness on the time-settlement curve is mainly due to the difference in strain rates before consolidation. This explanation was first pointed by Oka, Adachi and Okano (1986) and was confirmed by Tang and Imai (1995). Of course there might be other reasons such as sample disturbance and the natural variability (Leroueil, 1995; Mesri and Choi, 1985).

2.9.3 Effect of degradation

In the calculations in Fig. 2.7, β is set at zero. Next, let us discuss the effect of the parameter on structural degradation β.

Calculations are performed for different values of parameter β (= 0, 5, 20, 40). The case of β=0 corresponds to the original model without considering structural changes. The vertical settlement with time and pore-water generation with time are shown in Fig. 2.7. The excess pore pressure shows a temporary increase when the rate of structural changes takes a high value, in other words, β = 40 (Fig. 2.7(b)). The average void ratio e-log σ'_m relations for β = 0, 20, 40 are shown in Fig. 2.8. It shows a temporary decrease in the mean effective stress for the e-log σ'_m relations for β = 20 and 40. A similar tendency is obtained from the test embankment (Leroueil, 1988). The bending points in the curve correspond to points where the pore-water pressure begins to be stagnant or to increase in Fig. 2.7(b), at about 40 s for β = 0 and 66 s for β = 40.

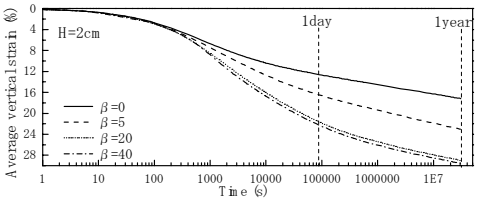

(a) Average vertical strain with time

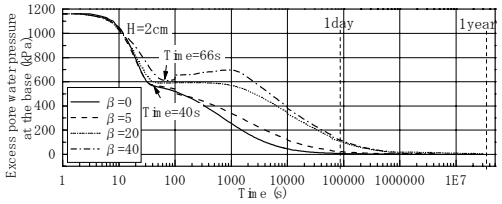

(b)Generated pore-water pressure with time

Figure 2.7. Effects of structural parameter β.

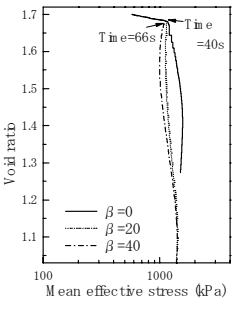

Figure 2.8. Average e-log σ'_m curve.

2.9.4 Two-dimensional consolidation problem

Stagnation and/or an increase in the pore-water pressure after loading and during the consolidation of soft clay is called "anomalous pore pressure" and it has been observed after loading and during consolidation by Professor J.K. Mitchell in his 20th Terzaghi Lecture (1986). This problem has hitherto been studied, but it has not yet been fully solved. Asaoka (2003) tried to analyze a similar problem by an elasto-plastic approach considering the degradation of materials. We would say that the reason is the rate-dependent structural degradation of soft clay,

as discussed above. Oka, Leroueil and Tavenas (1991) numerically analyzed such a phenomenon observed in the clay foundation at St. Alban's test embankment D using an elasto-viscoplastic model (Fig.2.9). They used a model with volumetric strain softening and a comparatively better solution than the conventional model. However, the stagnation or the temporary increase in pore-water pressure after the construction of the embankment could not be reproduced. In this section, we have analyzed the same problem using an elasto-viscoplastic model with the above-mentioned structural degradation (Karim et al., 2005).

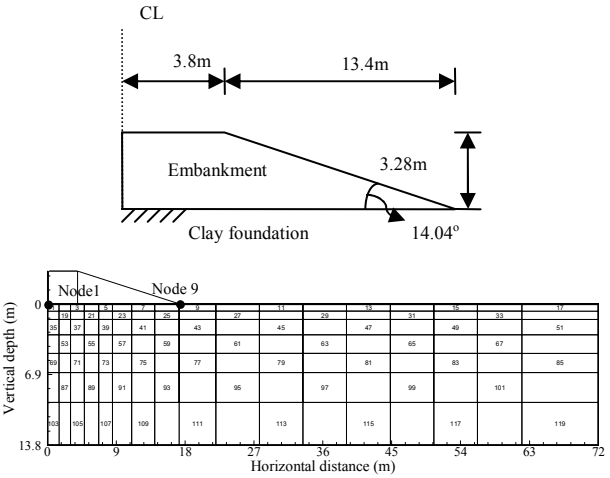

Figure 2.9. FEM mesh.

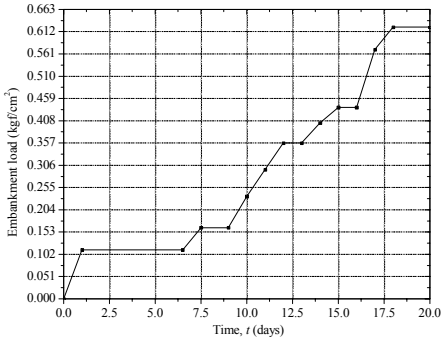

Figure 2.10. Construction process for embankment D.

The finite element mesh is shown Fig. 2.9. At the base of the soil layers, the displacements are fixed. Fig. 2.10 illustrates the loading history of this embankment.

The parameters used in the analysis and related formulas are listed in Tables 2.3 and 2.4.

We assumed that the top layer is modeled as being elastic with ν =0.25 and κ =0.01125(1+e) (2.5 times higher than the other layers). In addition, we modified the equation that controls the structural degradation as follows:

$$\sigma'_{ma} = \sigma'_{maf} + \left(\sigma'_{mai} - \sigma'_{maf}\right)\exp\left(-\beta\sqrt{z}\right) \tag{2.29}$$

instead of Eq. (2.15).

Fig. 2.11 shows the development of the pore-water pressure in the analysis and in the field. The numerically predicted pore-water pressure at a depth of 3 m (element No. 35) agrees well with the observed value in the field. We can see the stagnation and the temporary increase in pore-water pressure in the sensitive clay. The lateral displacement at the toe of the embankment is shown in Fig. 2.13. The predicted results match the measured ones quite well.

Table 2.3: Material parameters

Layer	*Depth* (m)	λ_0	λ_1	λ_2
1	0 ~ 0.66	0.02	0.300	0.100
2	0.66 ~ 1.50	0.0523	1.000	0.363
3	1.50 ~ 3.00	0.0719	1.140	0.495
4	3.00 ~ 4.80	0.0387	1.040	0.411
5	4.80 ~ 6.70	0.0246	0.560	0.282
6	6.70 ~ 9.60	0.0104	0.409	0.175
7	9.60 ~ 13.50	0.008	0.409	0.100

Layer	e_0	$\sigma'_{22(0)}$ (kgf/cm^2)	σ'_p (kgf/cm^2)	G_0 (kgf/cm^2)
1	1.10	10.0062	0.739	8.97
2	1.70	13.0473	0.582	15.3
3	2.30	18.0504	0.469	21.2
4	1.80	25.9965	0.720	30.7
5	1.80	35.0217	0.900	41.2
6	1.40	45.0279	0.140	57.1
7	1.40	70.0434	0.180	112

Table 2.4: Dependency of the parameters on the volumetric plastic strain

Volumetric viscoplastic strain ε^{vp} (%)	m'	λ	C (1/sec)
$\varepsilon^{vp} < 0.01$	26.7	λ_0	1.2×10^{-12}
$0.01 \le \varepsilon^{vp} \le 22.2$	26.7	λ_1	5.9×10^{-11}
$\varepsilon^{vp} > 22.2$	26.7	λ_2	5.9×10^{-11}

κ =0.00451(1+ e)	$OCR = 2.2$
C_k^* =0.5 e	$\sigma'_{mai} = \left(2K_0+1\right)\sigma'_p/3$
$K_0 = 0.8$	$\sigma'_{maf} = \sigma'_{mai}/OCR$
$M^* = 0.98$	$\beta = 4.15$
k_0 =1.05 × 10^{-8} m/s	γ_w = 9.81 kN/m^2

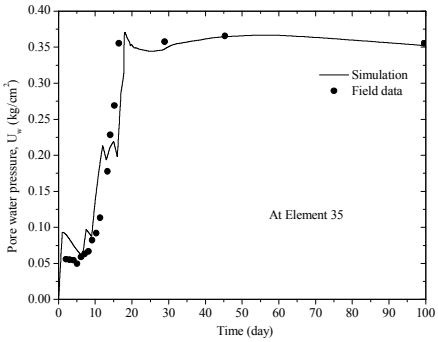

Figure 2.11. Observed and calculated pore-water pressure levels of element 35 beneath the center of the embankment at a depth of 3 m.

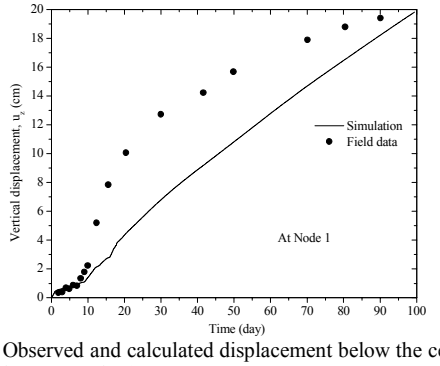

Figure 2.12. Observed and calculated displacement below the centerline of the embankment (Node 1).

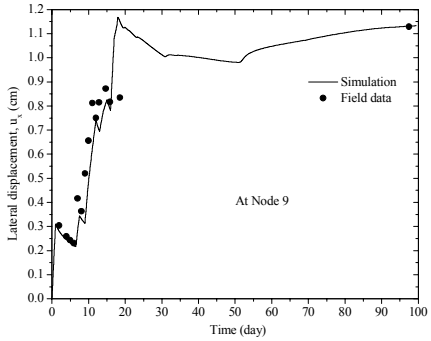

Figure 2.13. Observed and calculated lateral displacement at the toe of the slope (Node 9).

The settlement at the bottom of the embankment is illustrated in Fig. 2.12. During the early stage of loading, the predicted value agrees well with the observed data. However, there is some difference after the end of the construction, namely, we can see a smaller value for the settlement and it reaches the measured value again. This tendency is similar to that in the last analysis by Oka et al. (1991). Possible reasons for this difference are thought to be

1) The analysis was carried out using the infinitesimal strain theory,
2) The property of the first layer is not relevant,
3) Viscoplastic parameter C is not scalar, but tensorial,
4) Degradation of elastic modulus, etc.

Although more studies are needed to predict the settlement, the analysis brought out the fact that the introduction of structural degradation affects the unstable behavior of sensitive clay such as an increase in pore-water pressure or stagnation after the end of construction, as was pointed out by Professor Mitchell and others.

ble 2.5: Material parameters

ial suction s (kPa)	200	400
ial void ratio e	0.599	0.577
mpression index λ	0.13	0.091
elling index κ	0.03	0.015
ial mean average skeleton ss σ''_{me} (kPa)	354	496
coplastic parameter m'	22.0	22.0
coplastic parameter C_1 (1/s)	1.3×10^{-14}	1.3×10^{-13}
coplastic parameter C_2 (1/s)	4.0×10^{-14}	3.3×10^{-13}
ess ratio at critical state M_m^*	0.91	0.89
stic shear modulus G (kPa)	11100	18000
mpression yield stress σ''_{mbi} (kPa)	474	692
uctural parameter σ''_{maf} (kPa)	474	692
uctural parameter β	0	0
terial parameter b	0	0
tion effect parameter S_{i1}/S_{i1r}	1	10
tion effect parameter S_{i2}/S_{i2r}	1	8.25

2.10 *Cyclic elasto-visoplastic model*

We need a cyclic plasticity model for the dynamic analysis of clay. For that purpose, we have developed a cyclic viscoplasticity model with a non-linear kinematic hardening model (Oka, 1992) and a cyclic viscoelastic-viscoplastic model with a kinematic hardening model (Oka, Kodaka and Kim, 2003). The models have been successively applied to the dynamic analysis of the ground during earthquakes, considering liquefaction, and

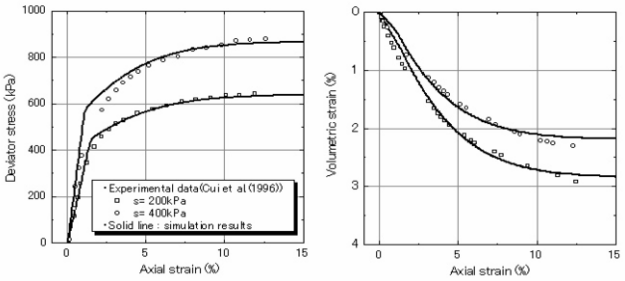

(a) Stress-strain relations (b) Volume changes

Figure 2.14. Stress-strain realations and volume change characteristics.

shown in the last chapter (Oka et al., 2003b). The cyclic elasto-viscoplastic model was applied to undrained triaxial tests with step-changed strain rates. It was found that the model can describe the isotaches characteristics well (Oka et al., 2003a).

2.11 *Elasto-viscoplastic model for unsaturated soil*

For unsaturated soil, we have applied the viscoplastic model considering the effect of suction and extended viscoplastic parameter C (Kim, Kimoto, Oka and Kodaka, 2005).

Starting from the effective stress by Bishop (1960), several considerations have been given to the stress variables (Fredlund and Morgenstern, 1977; Alonso et al. 1990; Kohgo et al. 1993; Wheeler and Karube, 1995). We have adopted an average skeleton stress for the model. The definition for the average skeleton stress, which includes the average fluid pressure acting on the soil pores, incorporates the first above-mentioned point in a direct manner (Houlsby, 1997; Jommi, 2000). However, it is noted that the unsaturated behavior of collapsible soil cannot be reproduced by merely adopting the average skeleton stress in a constitutive model. The collapsing behavior of unsaturated soil is macroscopic evidence of the structural instability of the soil skeleton, and it is totally independent of the stress variables adopted in the constitutive modelling (Oka, 1988; Jommi, 2000). This interpretation was explained by the experimental results of Matiotti et al. (1995). Therefore, it is necessary to consider the suction effect in order to include the collapsing behavior. In this section, we have considered the effect of suction within the framework of a constitutive model. In the proposed model, the basic stress variable is the average skeleton stress, σ''_{ij}, which is defined by the following equations (Bolzon et al., 1996; Ehlers, 2002):

$$\sigma_{ij}^s = \sigma''_{ij} + (1-n)P^F\delta_{ij} \tag{2.30}$$

$$\sigma_{ij}^f = nS_r u_w \delta_{ij} \tag{2.31}$$

$$\sigma_{ij}^g = n(1-S_r)u_a\delta_{ij} \tag{2.32}$$

$$\sigma_{ij} = \sigma_{ij}^s + \sigma_{ij}^f + \sigma_{ij}^g = \sigma''_{ij} + P^F\delta_{ij} \tag{2.33}$$

where σ_{ij}^s, σ_{ij}^f, and σ_{ij}^g are the partial stress values for the solid phase, the fluid phase, and the gas phase, respectively. n is the volume fraction, u_a is the pore-air pressure, u_w is the pore-water pressure, S_r is the degree of saturation, δ_{ij} is Kronecker's delta, and P^F is the averaged pore pressure, which is given through Dalton's law as follows:

$$P^F = (1-S_r)u_a + S_r u_w \tag{2.34}$$

Therefore, the average skeleton stress may be rewritten in the following way:

$$\sigma''_{ij} = \sigma_{ij} - \left[(1-S_r)u_a + S_r u_w\right]\delta_{ij} \tag{2.35}$$

It is worth noting that this cannot be called “effective stress”, since the average skeleton stress is used with the suction in the constitutive parameter.

In the model, we assumed the following flow rule:

$$\dot{\varepsilon}_{ij}^{vp} = C_{ijkl}\left\langle \Phi_1(f_y)\right\rangle \frac{\partial f_p}{\partial \sigma''_{kl}} \tag{2.36}$$

$$C_{ijkl} = a'\delta_{ij}\delta_{kl} + b'(\delta_{ik}\delta_{jl} + \delta_{il}\delta_{jk})$$

$$C_1 = 2b',\ \ C_2 = 3a' + 2b' \tag{2.37}$$

$$C_1 = \left[\frac{S_{i1}}{S_{i1r}}\right] \times C_{01},\quad C_2 = \left[\frac{S_{i2}}{S_{i2r}}\right] \times C_{02} \tag{2.38}$$

in which $\langle\ \rangle$ are Macaulay's brackets, $\langle \Phi_1(x)\rangle = \Phi_1(x)$, if $x > 0$, $\langle \Phi_1(x)\rangle$ =0, if $x \le 0$, and S_i denotes the suction effect. C_{01} and C_{02} are the viscoplastic parameters when the suction is S_{i1r} and S_{i2r} , respectively.

C_1 and C_2 are the viscoplastic parameters considering the suction effect.

A series of triaxial compression tests on unsaturated compacted silt is numerically simulated. Material parameters used in the analysis is listed in Table 2.5 The results show that the model is very applicable for describing the behavior of unsaturated soil. The average skeleton stress is not an effective stress, because it has to be used with both the suction-saturation relation and the introduction of suction into the material parameters in the constitutive model when the suction exists.

2.12 *Summary*

Elasto-viscoplastic models for soil have been developed and successively applied to the behavior of saturated and unsaturated cohesive soil. In particular, the proposed model considers structural changes and reproduces the unstable behavior encountered during consolidation, such as the temporary increase in pore pressure after stagnation. The effect of the sample thickness on the consolidation is reproduced by considering the difference in the initial strain rates. In the next section, the models are used to reproduce the strain localization behavior in the laboratory and such boundary value problems as the bearing capacity and an excavation analysis.

3 STRAIN LOCALIZATION

3.1 *Strain localization problems in geomechanics*

In order to analyze failure, we have to deal with strain localization near and/or after failure. It is well known that the strain localization of geomaterials causes such important problems as slope failure. In slope failure, deformation occurs in a narrow zone, namely, strain localization is closely related to the onset of failure (e.g., Scott 1987). The development of a failure surface is a classical issue in soil mechanics. Coulomb (1773) considered a failure surface in order to determine the collapse load in his famous work. Sokolovsky (1942) analyzed a slip plane as a stress characteristic at the limit equilibrium. As has been pointed out by Taylor (1948), the failure phenomenon of geomaterials is progressive. Hence, strain localization is a precursor to the development of a failure surface, and is a very important subject to investigate. Over the last three decades, the problem of strain localization in geomaterials such as soil and rock has been extensively studied within the context of experimental, theoretical, and numerical approaches. Many researchers (i.e., Hill, 1962; Rice, 1975, 1976; Rudnicki and Rice, 1975; Mühlhaus and Vardoulakis, 1987; Oka et al., 1994d; Muir Wood, 2002; Gudehus and Nübel 2004; etc.) have been working in this area from both experimental and analytical points of view. Rice (1976) and Rudnicki and Rice (1975) pointed out that the nature of this problem can be solved under the general framework of bifurcation problems and that localization problems should be studied within a wider framework of mechanics, including the rapid degradation of the material strength.

Angle of a shear band

The classical Mohr-Coulomb law gives the angle of the failure surface (shear band) as

$$\theta_M = \frac{\pi}{4} + \frac{\phi}{2} \tag{3.1}$$

where ϕ is the internal friction angle.

On the other hand, as is well known, Roscoe (1970) reported in his Rankine lecture that the rupture (failure) surface does not coincide with the stress characteristics, but with the zero-extension lines. This means that the angle of a shear band to major principle stress plane θ (see Fig. 3.1) is given by

$$\theta_R = \frac{\pi}{4} + \frac{\psi}{2} \tag{3.2}$$

where ψ is the dilatancy angle.

In addition, Roscoe (1970) pointed out that the thickness of a shear band is approximately 10 grains.

For the angle of a shear band, Arthur et al. (1977) proposed a shear band angle based on the experiments as

$$\theta_A = \frac{\pi}{4} + \frac{1}{4}(\phi + \psi) \tag{3.3}$$

Since $\psi < \phi$ and $\theta_R < \theta_A < \theta_M$. The angles experimentally obtained by Arthur et al. (1977) were supported by theoretical works (Vardoulakis, 1980; Vermeer, 1982). Vardoulakis (1980) reported that the experimental results coincide with Eq. (3.3). However, the experimental results for sand, obtained by Desrues (1990) and Lade (2003), are close to θ_M . Vardoulakis (1977) illustrated that the shear band angle depends on the particle diameter, in other words, the larger the soil particle size, the smaller the shear band angle. Tatsuoka et al. (1990) showed the shear band angle depends on *b*-value and anisotropy. These indicate the other effects on the angle of the shear band. For clay, Oka et al. (2004d) numerically indicated that the angle of a shear band depends on the strain rates and the permeability, as shown in Sections 3.8 and 3.9.

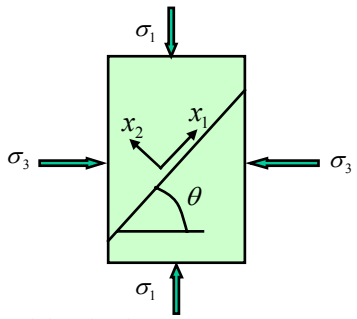

Figure 3.1. Angle of shear band

3.2 *Localization analysis*

It has been theoretically found that the onset conditions for strain localization can be captured by a bifurcation analysis (e.g., Hill, 1962; Rice, 1976). Rice (1976) showed that shear band formation is a problem because a shear band is the result of bifurcation from a homogeneous deformation. The onset conditions for localization are given by linear and non-linear

incremental constitutive models. For static problems, the conditions involve a loss of the elliptic onset condition, the thickness, the angel, and the distribution. Post localization behavior and the loss of ellipticity correspond to the loss of uniqueness, namely, the instability discussed within the framework of bifurcation and material instability.

Within the framework of a linear incremental model, the onset conditions are derived as the condition of equilibrium which requires the time rate of change in stress traction $\dot{\sigma}_{ij}n_j$ at the shear band to be zero, namely,

$$[\dot{\sigma}_{ij}]n_j = 0 \tag{3.4}$$

where n_j is the unit normal to the shear band. The bracket [ ] of a quantity denotes the difference in values of that quantity across the shear band.

The velocity is continuous, but the gradient of velocity is discontinuous.

$$[v_{i,j}] = \lambda_i n_j \tag{3.5}$$

where $v_{i,j}$ is the velocity gradient.

The incremental constitutive model is given by

$$\dot{\sigma}_{ij} = M_{ijkl}v_{k,l} \tag{3.6}$$

From Eqs.(3.4), (3.5) and (3.6),

$$H_{ik}\lambda_k = 0\ , \quad H_{ik} = M_{ijkl}n_j n_l \tag{3.7}$$

where M_{ijkl} is the stiffness tensor.

The onset conditions for non-zero λ_k are

$$\det[H_{ik}] = 0 \tag{3.8}$$

From these conditions, we can obtain shear band angle θ in a two-dimensional case. $n_1 = \cos\theta, n_2 = \sin\theta$ are the angle between the unit normal to the shear band and the major principle stress plane, respectively.

It is seen that Rice's bifurcation condition is the same as the singularity of the acoustic tensor (Mandel, 1964). This means that the occurrence of a shear band coincides with the accelerated wave trapping in the narrow zone. For the propagation of an acceleration wave [propagation of the discontinuity of acceleration], it is necessary for the eigenvalues to be positive and real. Acceleration is discontinuous across the wave front for the acceleration wave, although the displacement and the velocity are continuous. When the eigenvalues are negative and zero, discontinuity cannot propagate and it is referred to as stationary discontinuity, namely, shear bands or complex (flutter) instability.

The zero determinant of the accoustic tensor by Eq. (3.7) corresponds to a change in the type of partial differential governing equations from elliptic to hyperbolic (Hill and Hutchinson, 1975). Bigoni and Hueckel (1991) found that the loss of strong ellipticity coincides with the nullity of the determinant of the symmetric part of the acoustic tensor.

Strain localization has been well recognized as the development of shear bands. On the other hand, another type of strain localization has also been observed, namely, compaction bands (Mollema and Antonellini, 1996; Olsson, 1999). Compaction bands were experimentally found for sandstone as a tabular zone that exhibits closure, but no shear offset (Mollema and Antonellini, 1996). The compaction bands comprise a kind of volumetric strain localization due to a pore collapse. The compaction bands of porous sandstone exhibit a sharp reduction in permeability that causes difficulties in oil production. Olsson (1999) has shown that compaction bands can be described by the strain localization theory of Rudnicki and Rice (1975) as well as by shear localization problems. The re-examination of Rudnicki and Rice's theory comes from the corrections of the Rudnick and Rice theory by Perrin and Leblond (1993). They showed that the possible range for the sum of the dilatancy factor and the coefficient of internal friction is wider than that shown in Rudnicki and Rice's paper, in other words, $\beta + \mu \le \sqrt{3}/2$ should be read as $-\sqrt{3} \le \beta + \mu \le \sqrt{3}$.

Rudnicki and Olsson (1998) re-examined the fault angles predicted by the shear localization theory and obtained the following convenient form:

$$\theta = \frac{\pi}{4} + \frac{1}{2}\arcsin\alpha\ ,\ \alpha = \frac{(2/3)(1+\nu)(\beta+\mu) - N(1-2\nu)}{\sqrt{4-3N^2}} \tag{3.9}$$

$$N = \sigma'_{II}/\bar{\tau} \tag{3.10}$$

where $\bar{\tau} = \sqrt{s_{ij}s_{ij}/2}$, s_{ij} is the deviatoric stress tensor, ν is Poisson's ratio, β is the gradient of the plastic potential surface, σ'_{II} is the intermediate principal deviatoric stress and μ is the gradient of the yield surface.

Using Eq. (3.9), it has been realized that the smaller angle of the compaction bands can be described.

In order to observe compaction bands for soil, Castellanza and Nova (2004) reported a compaction band forming in the cemented granular soils during the oedometer test. They observed a stress-strain relation with a plateau that occurred after the peak stress had been reached, which is a typical stress-strain relationship for compaction bands. Oka and Kimoto (Kimoto and Oka, 2004; Kimoto and Oka, 2005) pointed out that the large compression of structured clay is due to the development of compaction bands, and they numerically analyzed the unstable consolidation of clay with degradation. This problem will be discussed in the following section.

3.3 *Instability of geomaterials*

As mentioned above, strain localization can be described as bifurcation conditions by Eq. (3.8), namely, a zero determinant of the acoustic tensor (Rice, 1976; the loss of the positive definiteness of constitutive matrix D). The loci on the π plane for which the determinant of the acoustic tensor is zero, namely, the loci of the localization conditions, never intersect the stress axes. This means that shear banding cannot occur in conventional triaxial compression tests before the failure state. On the other hand, shear bands may easily develop in plane strain tests. The stress state reaches the surface by the zero determinant of the acoustic tensor before it reaches the limit state. The limit state is characterized by the conditions under which the determinant of the constitutive matrix equals zero (Tokuoka, 1971) and it is called the failure condition.

Nova (1994) studied the other bifurcation criteria and found that the conditions for the loss of controllability are obtained as a zero determinant of the symmetric part of stiffness tensor D_s :

$$\det[D_s] = 0 \tag{3.11}$$

In general, for the non-associated plasticity model, $\det[D_s] = 0$ even when $\det[D] \neq 0$. $[D]$ is the stiffness tensor ($\{\dot{\sigma}\} = [D]\{\dot{\varepsilon}\}$).

In the experiments on soil, we can choose the variables for controlling the system; e.g., we control the axial strain rates and maintain the lateral stress constant in the strain control triaxial tests. When the conditions are satisfied, we cannot continue the experiments. For instance, we cannot execute triaxial tests for strain hardening-softening material after the peak stress by the axial stress control. Nova found that the loss of controllability is

equal to the negative second-order work. This indicates that if the stress states satisfy the zero determinant of the symmetric part of the material stiffness matrix, $\det[D_s] = 0$, bifurcation may occur. Lade's instability condition (1992) is equivalent to the conditions under which the volumetric compliance is zero under the isotropic loading of the material. This state comes after the peak stress in the triaxial tests.

Since the non-associative flow rule of plasticity is not symmetric, a variety of unstable conditions may arise. They are the strain localization condition (the loss of the determinant of the acoustic tensor, Rice, 1976), the zero secondary work condition (Hill, 1958), and the loss of the controllability condition (Nova 1994), etc. The zero secondary work condition and the loss of the controllability condition may lead to diffuse bifurcation or instability that manifests as a barreling or bulging type of phenomenon (Nova, 1998; Darve, 2001). The surfaces that define these types of instability are inside the failure surface (Imposimato and Nova, 2001). Benallal and Comi (2003) studied using a perturbation approach and found that the failure mode of non-associated material exhibit either diffuse(long wavelength) mode and localization mode (short wavelength).

For the incremental strongly non-linear law, the onset conditions for a shear band have been obtained by Chambon et al. (2000) and Kolymbas et al. (1989). The incrementally non-linear model has been proposed as hypoplastic models by Kolymbas et al. (1989) and Chambon et al. (2000).

For the hypoplastic models,

$$\dot{\sigma}_{ij} = M_{ijkl}\dot{F}_{kl} + b_{ij} \| D_{kl} \| \tag{3.12}$$

where M_{ijkl} is the constitutive fourth order tensor, b_{ij} is the constitutive second order tensor, $\dot{F}_{kl}$ is the rate of deformation gradient, D_{ij} is the stretching tensor, and $\| \ \|$ denotes the Euclidian norm.

For the hypoplastic models, several criteria for bifurcation have been obtained based on the invertibility of $M_{ijkl}n_k n_l$. Namely, three types of bifurcation criteria were given as: 1) the norm criteria, 2) the determinant criteria, and 3) the tangential criteria. The norm criteria are first met and the determinant criteria are never met (Chambon et al., 2000; Tamaganini et al., 2001) .

3.4 *Non-coaxiality*

It is known that the direction of the principle strain rates does not need to coincide with the direction of the stress rates even for anisotropic materials. However, even for isotropic materials, the direction of the principle strain rates does not need to coincide with the direction of the stress rates; this is called non-coaxiality. The yield vertex that comes from the micromechanical consideration leads to the non-coaxiality. Rudnicki and Rice (1975) introduced this vertex effect into the model by a non-coaxial term called the Mandel-Spencer modulus term. The non-coaxial term was naturally derived into the planer model from the double slip theory by de Josselin (1971). Spencer (1964) proposed a double shearing model by assuming a micromechanical slip along the stress characteristic lines obtained from the equilibrium equations and Mohr-Coulomb failure criteria (Sokolovsky, 1942). The double shearing model was generalized to be a model with dilatancy by Mehrabadi and Cowin (1978). They have resulted in the non-coaxial term which is workless, e.g., purely deviatoric. Anand （1983）generalized it into the isotropic hardening model. This non-coaxial model has accounted for the vertex of the plastic potential surfaces (Rudnicki and Rice, 1975). Yatomi et al. (1989) used the non-coaxial term in Cam-clay model and showed that the non-coaxial term easily led to instability as shear banding or as accessibility to bifurcation from an elliptic to a hyperbolic type of governing equation. Papamichos and Vardoulakis (1995) developed a different type of non-coaxial theory by introducing a kinematical concept. Hashiguchi et al. (2004) developed a tangential plasticity theory accounting for non-coaxiality. All of the models are rate-independent plasticity theories. Oka (1993b) developed a rate-dependent non-coaxial viscoplastic model using a transformed stress tensor with the current stress-induced quasi-anisotropy shown in the next paragraph. The other source of non-coaxiality is the anisotropy of the materials (Nemat-Nasser, 1983).

3.5 *Current stress-dependent characteristics and anisotropy*

As mentioned above, the non-coaxial term called the Mandel-Spencer modulus term is derived from the characteristic plane. There are several constitutive models based on the characteristic plane. Matsuoka and Nakai (1974) proposed a model in which the failure criteria depend on the interim principal stress, although Mohr-Coulomb's criteria depend on the maximum and the minimum principal stresses. Oka (1993a, 1993b) proposed a transformed stress tensor to describe the current stress-dependent behavior of soil, by which Matsuoka and Nakai's failure criteria (1985) can be derived. In addition, the deviatoric flow rule can be reproduced by which the direction of the strain rate is different from the direction of the stress path. The transformed stress tensor

$$\sigma_{ij}^{A} = F(\sigma_{ij}, A_{ij}) \tag{3.13}$$

is derived from Wang's representation theorem as a function of the stress tensor and the structural tensor (Spencer, 1987). The structural tensor was first adopted by Boehler and Sawczuk (1977) as

$$A_{ij} = m_i m_j \tag{3.14}$$

where m_i is a unit normal to the characteristic plane.

Considering Matsuoka and Nakai's well-known failure criteria (1974), m_i can be taken as the unit normal to the spatial mobilized plane. If we take the sedimentation plane as the characteristic plane, we can construct a transversely isotropic theory (Oka, 1993a; 1993b; Oka et al., 2002c). Nakai's t_{ij} theory can be classified as being similar to the transformed stress tensor (Nakai and Mihara, 1984; Chowdhury and Nakai, 2001), although they originally proposed the theory based on physical considerations.

3.6 *Regularization of ill-posedness*

The onset conditions for a shear band can be obtained analytically or numerically, but it is also necessary to predict the post-localization behavior. After a shear band has occurred, the boundary value problem becomes ill-posed. Hence, ellipticity (well-posedness) must be retrieved. Well-posedness is the uniqueness of a solution and the continuous dependence on the boundary conditions. In the finite element analysis, this instability leads to a strong mesh-size dependency and, in turn, the thickness of the shear band becomes zero, although the thickness of a shear band is finite in the experiments.

There are several methods for the regularization of the ill-posedness of governing equations.

1) Non-local formulation of constitutive models
   Non-local models, such as the higher order strain gradient-dependent model (Aifantis, 1984; Mühlhaus and Aifantis, 1991; Vardoulakis and Aifantis, 1991), and micropolar models, such as the Cosserat model (Mühlhaus, 1986; Teichman and Wu, 1993; Bauer and Huang, 2001), have been used for the post-localization analysis. An integral type of non-local model has been developed to account for the non-local effect. The feature of non-local models is that they contain the material length scale. Mühlhaus and Oka (1996) clarified that the higher strain gradient term naturally comes from the fact that the material is discrete and has an inherent length scale.

2) Solid-fluid two-phase formulation
For water-saturated soil, a Biot type of two-phase mixture theory can be applied with an elasto-plastic model for the soil skeleton. In this type of formulation, Zhang and Schrefler (2001) found that the critical hardening moduli become smaller than those for a single material (the permeability is large). This indicates that the localization is delayed for the case of water-saturated soil. They also pointed out that there exists a domain of permeability where stability is lost, but the hyperbolicity remains in the dynamic analysis of water-saturated soil.

Vardoulakis (1996a, 1996b) reported that the boundary value problem encountered ill-posedness even when the two-phase formulation was adopted. However, from the numerical studies, it was found that the strain localization is depressed in the case of low permeability (Loret and Prévost, 1991; Oka et al., 1995b; Asaoka et al., 1997).

3) Viscoplastic regularization
An elasto-viscoplastic formulation can retrieve the ill-posedness of the governing equations through the instantaneous elastic response. For example, Loret and Prévost (1991) adopted a viscoplastic regularization technique using Duvaut and Lions's theory (1976) by which the invisid model can be transformed into a viscoplastic model with one viscous parameter.

The elasto-viscoplastic model which is transformed from an elasto-plastic model can maintain the well-posedness, namely, it can avoid the strong mesh-size dependency in the finite element analysis if the growth of viscoplastic strain is bounded. It is worth noting that the elasto-viscoplastic models can delay the instability, e.g., shear bands but cannot stabilize the catastrophic instability.

4) Dynamic formulation
The dynamic formulation of boundary value problem has been successfully used to solve static boundary value problems. This may be due to the fact that the type of governing equations remains to be hyperbolic. Vardoulakis (1996a, 1996b) proposed a regularization method that introduced micro-inertial and strain gradients into the non-associated plasticity model called the "2nd grade elastoplasticity model".

5) Discrete model and finite element analysis with strong discontinuity
Since discrete analyses such as DEM (e.g., Cundall and Strack, 1979; Kishino, 1988; Thornton, 1998) include an internal length scale, the instability could be avoided, although it needs many degrees of freedom. Oda and Kazama (1998) clearly showed that the shear band was able to be reproduced by DEM through the weak restriction of the moment between the particles. The finite element method with strong discontinuity has been developed to capture the slip surface without mesh-size dependency (e.g., Regueiro and Borja, 2001; Oliver et al., 1999).

As mentioned above, large amounts of studies have been done on the strain localization problems of geomaterials, both experimentally and theoretically (e.g., Geomaterials, Darve ed. Elsevier Appl. Sci. 1993; Vardoulakis and Sulem, Blackie Academic & Professional, 1995). However, many of them are for cohesionless soils. On the other hand, comparatively fewer studies have been performed for cohesive soil, such as clay, although Palmer and Rice (1973) pointed out the strain localization of overconsolidated clay as a slip surface.

It is well known that cohesive soil such as clay exhibits strain-rate sensitivity. Hence, in the modeling of clayey soils, it is more natural to adopt elasto-viscoplastic models instead of elasto-plastic ones, although the elasto-plastic models are extreme models for such materials. As has been mentioned above, elasto-viscoplastic models have been developed for clay to take into account the rate sensitivity.

Strain localization has been found to be the change in the type of partial differential equations of the governing equations of boundary value problems for the rate-independent modeling of materials such as sand. In other words, the type changes from elliptic to hyperbolic for static problems. On the other hand, for elasto-viscoplastic modeling, such instability as strain localization can be treated as the exponential growth of fluctuation, i.e., Lypunov instability, and as the growth of kinetic energy and momentum for dynamic cases (see Table 3.1).

Table 3.1: Classification of plastic and viscoplastic instability

	Rate-independent model	Rate-dependent model
Body	Elasto-plastic body	Elasto-viscoplastic body
Static conditions	Loss of ellipticity Loss of controllability Zero secondary order work Loss of Lyapunov stability	Exponential growth of fluctuation Loss of Lyapunov stability
Dynamic conditions	Loss of hyperbolicity Loss of Lyapunov stability	Growth of kinetic energy and momentum Loss of Lyapunov stabiity

3.7 *Effects of the transport of pore water and material heterogeneity on strain localization*

In this section, we will clarify the effects of permeability and initial heterogeneity on the strain localization of fluid-saturated cohesive soil modeled by a strain gradient-dependent poro-viscoplastic constitutive model.

The effects of permeability and gradient parameters on the growth rate of the fluctuation were obtained by a linear instability analysis. The deformation behavior of the clay specimens modeled with a viscoplastic model with a second order strain gradient during shear was numerically analyzed by a soil-water coupled FEM under both globally undrained and partially drained conditions. We found that the deformation pattern and the stress-strain curve greatly depend on the permeability, the drainage conditions, and the initial non-homogeneous properties.

Rice (1976) and Rudnicki and Rice (1975) pointed out that the nature of this problem can be solved within a general framework of bifurcation problems and the localization problem should be studied within the wider framework of mechanics, including the rapid degradation of the material strength. In addition, Rice (1975) indicated the importance of local-inhomogeneity and the behavior of pore fluid. The effect of pore fluid on the localization problem has been analyzed by several researchers within the context of a two-phase mixture theory such as Biot's theory (1956) and de Boer (1996). Loret and Prévost (1991), Schrefler et al. (1995, 1996), and Ehlers and Volk (1998) numerically studied the localization problem of water-saturated geomaterials with the rate-independent constitutive model. Vardoulakis (1996a, 1996b) found that boundary value problems with a non-associated rate-independent plastic model become mathematically ill-posed even if the pore water flow is included.

Oka, Adachi and Yashima (1994b) have been dealing with the localization problem of water-saturated clay through the use of viscoplastic constitutive equations due to the rate-dependent nature of cohesive soil. Zhang et al. (1999) and Zhang and Schrefler (2000) investigated the interaction between permeability and a gradient-dependent parameter with a one-dimensional instability analysis and a numerical simulation in the context of the dynamic strain localization of saturated and partially saturated porous media. As for the experimental study, Finno et al. (1998) discussed the effects of drainage conditions on strain localization in sand specimens. In these studies, many points have been clarified such as the effect of dilatancy, permeability, strain rates, etc., for particular constitutive models. Loret and Prévost (1991) and Schrefler et al. (1995) showed that strain localizes in a narrow zone in the case of higher permeability lev-

els. On the other hand, Oka, Adachi and Yashima (1995) reported different results in which deformation was more localized in the case of low permeability levels compared with a material with absolutely very high permeability. Several problems remain which need to be studied. One of them is to clarify the roles of permeability and drainage conditions in the instability of the governing equations and the deformation patterning of non-local viscoplastic materials, such as a higher order strain gradient-dependent model. The other problem is to clarify the effect of the initial heterogeneity.

3.7.1 *Gradient-dependent viscoplastic model for clay*

Herein, we are adopting an elasto-viscoplastic model by Oka (1981), Adachi and Oka (1982), Adachi et al. (1987a), and Oka et al. (2003a) discussed in Chapter 2 and its generalized viscoplastic model with a higher order-strain gradient. The following formulation is based on the model presented in Chapter 2, which is an extended model of the original model (Adachi and Oka, 1982) taking shear softening into account.

The viscoplastic flow rule is given by

$$D_{ij}^{vp} = \gamma \langle \Phi_1(F) \rangle \Phi_2(\xi) \frac{\partial f}{\partial \hat{\sigma}'_{ij}} \quad , \quad F = \frac{f - \kappa_s}{\kappa_s} \tag{3.15}$$

$$\sigma'_{ij} = \sigma_{ij} - u_w \delta_{ij} \tag{3.16}$$

where D_{ij}^{vp} is the viscoplastic stretching, γ is the viscosity parameter, σ_{ij} is the total stress tensor, and σ'_{ij} is Terzaghi's effective stress tensor.

$$\Phi_2 = 1 + \xi \tag{3.17}$$

Internal variable ξ expresses the deterioration of the materials and obeys the following evolutional equation:

$$\dot{\xi} = \frac{M_f^{*2}}{G_2^*(M_f^* - \eta^*)^2} \dot{\eta}^* \tag{3.18}$$

where M_f^* is the value of stress ratio η^* at the failure state, G_2^* is a material parameter, and η^* is the stress invariant ratio defined by $\eta^* = \sqrt{2J_2} / \sigma'_m$, where J_2 is the second invariant of deviatoric stress tensor S_{ij} and σ'_m is the mean effective stress.

It has been experimentally found that the shear strength and the deformation characteristics of clay depend on the volumetric strain. The volumetric plastic strain is used as a hardening parameter in the well-known Cam-clay model (Roscoe et al., (1963)). The volumetric inelastic strain associated with both consolidation and dilatancy is a measure of the deterioration of the granular materials. On the other hand, Mühlhaus and Oka (1995, 1996) demonstrated that the higher order gradients may be attributed to the fact that the soil is discrete. Frantziskonis (1993) also showed that the material inhomogeneity can be described by the constitutive model with higher order strain gradients. Thus, in the present paper, we have introduced the second order gradient of the viscoplastic volumetric strain into the constitutive model to describe more accurately and more sufficiently the deformation of clay by considering the non-local and the viscoplastic effects of the material. In practice, the yield function includes the Laplacian of the viscoplastic volumetric strain and it is proposed as follows:

$$f - \kappa_s = \frac{\sqrt{2J_2}}{M^* \sigma_m} + \ln \frac{\sigma'_m}{\sigma'_{my}} - a_3 \nabla^2 v^p \tag{3.19}$$

in which $f - \kappa_s = 0$ indicates static state ($f = f_s$), κ_s is the hardening parameter, v^p is the viscoplastic volumetric strain ($= \int D_{kk}^{vp} dt$), $a_3 \nabla^2 v^p$ is the gradient term with a_3 defined as a material constant, J_2 is the second invariant of deviatoric stress tensor S_{ij} , and σ'_m is the mean effective stress. σ'_{my} is a hardening parameter. The evolutional equation of σ'_{my} is

$$\frac{d\sigma'_{my}}{\sigma'_{my}} = \frac{1+e}{\lambda - \kappa} dv^p \tag{3.20}$$

where dv^p is an increment of v^p .

We assume that the dynamic yield function is the same as the static yield function. Following the experimental results, $\gamma \Phi_1(F)$ in Eq. (3.15) is given by

$$\gamma \Phi_1(F) = C \exp\left\{ m' \left(\frac{\sqrt{2J_2}}{M_f^* \sigma'_m} + \ln \frac{\sigma'_m}{\sigma'_{me}} - \frac{1+e}{\lambda - \kappa} v^p - \alpha_3 \nabla^2 v^p \right) \right\} \tag{3.21}$$

$$C = C_0 \exp\left(m' \ln \frac{\sigma'_{me}}{\sigma'_{my0}} \right) \tag{3.22}$$

where m' and C are viscoplastic parameters and a gradient coefficient a_3 is assumed to be constant. σ'_{me} is the initial value of σ'_m , σ'_{my0} is the initial value of the hardening parameter, λ is the consolidation index, κ is the swelling index, and e is the void ratio.

Elastic stretching D_{ij}^e (or strain rate tensor $\dot{\varepsilon}_{ij}^e$) is given by an isotropic Hooke's type law, i.e.,

$$D_{ij}^e = \frac{1}{2G} \hat{S}_{ij} + \frac{\kappa}{3(1+e)\sigma'_m} \delta_{ij} \hat{\sigma}_m \tag{3.23}$$

where G is the elastic shear modulus, $\hat{S}_{ij}$ is the deviatoric part of the Jaumann rate of effective Cauchy stress rate tensor, $\hat{\sigma}_m$ is the Jaumann rate of mean effective stress, and δ_{ij} is Kronecker's delta.

The Jaumann rate of Cauchy's effective stress tensor is given by

$$\hat{\sigma}_{ij} = \dot{\sigma}'_{ij} - W_{ik} \sigma'_{kj} + \sigma'_{ik} W_{kj} \tag{3.24}$$

where W_{ij} is the spin tensor.

The total stretching D_{ij} (or the strain rate tensor for the small strain case of $\dot{\varepsilon}_{ij}$) is decomposed into the elastic part and the viscoplastic part as

$$D_{ij} = D_{ij}^e + D_{ij}^{vp} \quad \text{or} \quad \dot{\varepsilon}_{ij} = \dot{\varepsilon}_{ij}^e + \dot{\varepsilon}_{ij}^{vp} \tag{3.25}$$

3.7.2 *Instability analysis of a fluid-saturated viscoplastic material model*

Instability under locally undrained conditions

We can easily discuss the instability of the model given by Eq. (3.15) to study the conventional undrained creep behavior under locally undrained conditions, i.e., the permeability coefficient is zero. Oka, Adachi and Yashima (1995) obtained the time rate of the second invariant of viscoplastic strain rate I_2^{vp} under the undrained creep conditions where the deviatoric stress levels are constant as

$$\dot{I}_2^{vp} = a(\eta^*) [I_2^{vp}]^2 \tag{3.26}$$

where $I_2^{vp} = \sqrt{\dot{\varepsilon}_{ij}^{vp} \dot{\varepsilon}_{ij}^{vp}}$, $\eta^* = \sqrt{2J_2} / \sigma'_m$

When $a(\eta^*) \le 0$, $\dot{I}_2^{vp}$ is negative or zero, namely, the system is stable. On the other hand, when $a(\eta^*) > 0$, the system becomes unstable because the small fluctuation in the viscoplas-

tic strain rates will grow. It is worth noting that $\eta_c^* < M^*$ (M^* is the value of η^* at the critical state and η_c^* is the value of η^* when $a(\eta^*) = 0$). This indicates that the clay will be unstable before the critical state under the locally undrained conditions in which the permeability coefficient is zero in the normally consolidated region.

In addition, Oka, Adachi, and Yashima (1995) obtained the growth rate of small fluctuation ω under plane strain locally undrained conditions using the linear stability analysis as

$$\omega = \frac{-Z_2}{\mu Z_1 \cot^2 2\theta + H_1} \tag{3.27}$$

where θ is the angle of the shear band and $Z_1 > 0$, $\mu > 0$, and $H_1 > 0$.

Hence if $Z_2 < 0$, the material becomes unstable and the fluctuation will grow in the orientation of $\theta = 45°$. This means that the angle of the shear band is 45 degrees. These results coincide with the prediction by the bifurcation analysis for an elasto-plastic model (e.g., Vardoulakis, 1996). The results of the above-mentioned instability are limited in the normally consolidated region (Fig. 3.2). However, the instability analysis for the viscoplastic model with degradation proposed by Kimoto (2002) (Eq. (2.22)) showed that the material is more instable in the overconsolidated regions (Fig. 3.3). This point will be numerically discussed in Section 3.8.

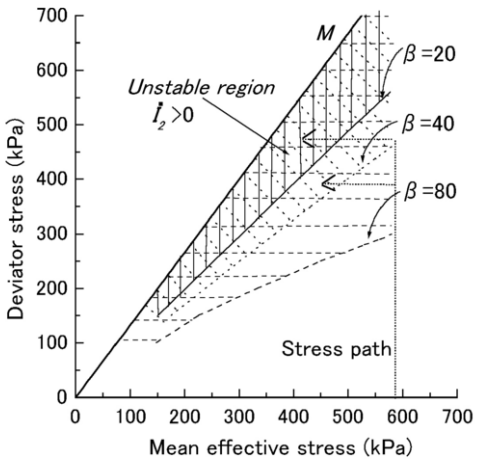

Figure 3.2. Unstable regions ($\eta^* < M^*$).

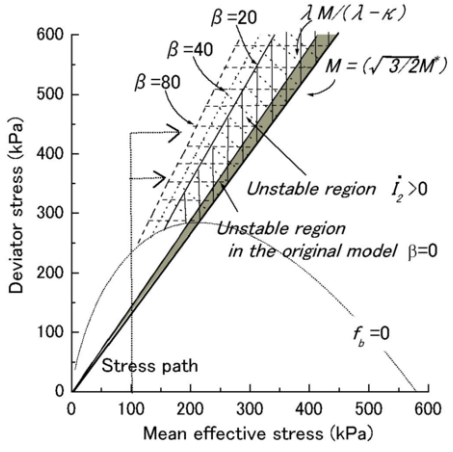

Figure 3.3. Unstable regions ($\eta^* > M^*$).

Instability analysis considering the pore water flow

Let us consider instability considering the pore water flow in the soil. Loret and Prévost (1991) and Schrefler et al. (1995) studied the effects of permeability on the dynamic strain localization analysis using a Mohr-Coulomb law with the associated flow rule. Loret and Prévost (1991) stated that in the case of low permeability levels, the instability may develop more slowly than in the case of high permeability levels. On the other hand, Oka et al. (1995) conducted a numerical analysis of strain localization under quasi-static conditions using an elasto-viscoplastic model. From the numerical results, they pointed out that the distribution of pore-water pressure is moderate with higher permeability levels and the strain localization is weaker. In their paper, the two results were compared and they suggested that the difference between the two results might be due to the different dilatancy characteristics; they pointed out that they took different loading conditions such as quasi-static and dynamic conditions and indicated the difference between rate-dependent and rate-independent models. However, the effects of permeability on the strain localization for a viscoplastic material under quasi-static conditions have not yet been fully studied.

Oka et al. (1995) stated only the effect of permeability on the strain localization obtained through the distribution of pore-water pressure in their conclusions. Hence, it should be pointed out that the effect of permeability on the strain localization using an elasto-viscoplastic model under quasi-static conditions has to be studied by both a numerical simulation and an instability analysis. In order to more clearly discuss the effects of permeability on strain localization, an instability analysis was carried out under two-dimensional conditions within the context of a small strain theory for simplicity (Oka et al., 1999c; Higo et al., 2005a). An instability analysis has been conducted by Oka et al. (1999) in which a simplified linear rigid-viscoplastic model was used.

3.7.3 *Perturbed governing equations*

1) Constitutive equations

A simplified elasto-viscoplastic model is used in this analysis with a small strain field assumption. The strain rate tensor is broken down into an elastic strain rate tensor and a viscoplastic strain rate tensor.

The elastic strain rate is given based on the linear elasticity theory as

$$\dot{\sigma}'_{ij} = 2G\dot{\varepsilon}^e_{ij} + \frac{1}{2}(3K - 2G)\dot{\varepsilon}^e_{kk}\delta_{ij} \tag{3.28}$$

where the superimposed dot denotes differentiation with respect to time t , K is the elastic bulk modulus, G is the elastic shear modulus, and δ_{ij} ($i = 1,2$, $j = 1,2$) is Kronecker's delta.

Viscoplastic strain rate $\dot{\varepsilon}^{vp}_{ij}$ is given as

$$\sigma'_{ij} = 2\mu\dot{\varepsilon}^{vp}_{ij} + \frac{1}{2}\dot{\varepsilon}^{vp}_{mm}\mu'_k\,\delta_{ij} + 2G''\varepsilon_{ij} + \frac{1}{2}\varepsilon_{mm}K'\delta_{ij} \tag{3.29}$$

in which μ and μ'_k are parameters of the viscosity, G'' and K' are the viscoplastic hardening parameters, and the accumulated strain is defined by $\varepsilon^{vp}_{ij} = \int \dot{\varepsilon}^{vp}_{ij} dt$.

When we introduce a second order gradient of the viscoplastic volumetric strain, Eq. (3.29) becomes

$$\sigma'_{ij} = 2\mu\dot{\varepsilon}^{vp}_{ij} + \frac{1}{2}\dot{\varepsilon}^{vp}_{mm}\mu'_k\,\delta_{ij} + 2G''\varepsilon^{vp}_{ij} + \frac{1}{2}\varepsilon^{vp}_{mm}K'\delta_{ij} - \frac{1}{2}a_3\varepsilon^{vp}_{mm,nn}\delta_{ij} \tag{3.30}$$

where a_3 is the gradient parameter.

2) Equations of equilibrium

Let us consider the equilibrium equations, namely, undrained conditions in a perturbed configuration. The equilibrium equations can be written as follows:

$$\sigma_{ij,j} = \sigma'_{ij,j} + u_{w,j}\delta_{ij} = 0 \tag{3.31}$$

where σ_{ij} is the total stress tensor, u_w is the pore-water pressure and, as usual, the commas denote differentiation with respect to spatial coordinates.

3) Pore fluid flow

From the solid-fluid two-phase mixture theory, the governing equation for the pore fluid is given by

$$\dot{\varepsilon}_{mm} = -\frac{k}{\gamma_w}\nabla^2 u_w \tag{3.32}$$

where k is the permeability coefficient and γ_w is the unit weight of the pore water.

4) Perturbed governing equations

The perturbations of pore-water pressure u_w and velocities v_i are assumed to be of the periodic form in a two-dimensional form as

$$[\tilde{u}_w, \tilde{v}_i, \tilde{\sigma}'_{ij}]^T = [u_w^*, v_i^*, \sigma'^*_{ij}]^T \exp[iq(n_k x_k) + \omega t] \tag{3.33}$$

where the perturbed variable is indicated by tilde, q is the wave number ($=2\pi/l$, l : wave length), ω is the speed of the fluctuation growth, n_i is the component of the unit vector n, which is normal to the shear band, and superscript * indicates the amplitude of each variable.

$$n = (-\sin\theta, \cos\theta) = (n_1, n_2) \tag{3.34}$$

The perturbed equilibrium equations are

$$\tilde{\sigma}_{ij,j} = \tilde{\sigma}'_{ij,j} + \tilde{u}_{w,j}\delta_{ij} = 0 \tag{3.35}$$

while the perturbed continuity equation is

$$\dot{\tilde{\varepsilon}}_{mm} = -\frac{k}{\gamma_w}\nabla^2 \tilde{u}_w \tag{3.36}$$

and the perturbed constitutive equations are given as

$$\dot{\tilde{\varepsilon}}_{ij} = \dot{\tilde{\varepsilon}}^e_{ij} + \dot{\tilde{\varepsilon}}^{vp}_{ij} = \frac{1}{2G}\dot{\tilde{\sigma}}'_{ij} + \frac{1}{2}\left(\frac{1}{3K} - \frac{1}{2G}\right)\dot{\tilde{\sigma}}'_{kk}\delta_{ij}$$
$$+\frac{1}{2\mu}\left[\tilde{\sigma}'_{ij} - \frac{1}{2}\mu''_k\tilde{\sigma}'_{kk}\delta_{ij} - 2G''\tilde{\varepsilon}_{ij} - \frac{1}{2}K''\tilde{\varepsilon}_{kk}\delta_{ij}\right] \tag{3.37}$$

Using the following relations,

$$\dot{\tilde{\varepsilon}}_{ij} = \frac{1}{2}\left(\tilde{v}_{i,j} + \tilde{v}_{j,i}\right) \tag{3.38}$$

We can rewrite the equations of equilibrium and pore fluid flow and the constitutive equations in a matrix form as

$$[A]\{y\}^T = \{0\}, \ \{y\} = \{\sigma'^*_{11}, \ \sigma'^*_{22}, \ \sigma'^*_{12}, u_w^*, v_1^*, v_2^*\} \tag{3.39}$$

The eigenvalue is obtained from the condition $\det[A] = 0$.

$$\left(\omega + \frac{G''}{\mu}\right)\left(\omega^3 + \alpha_1\omega^2 + \alpha_2\omega + \alpha_3\right) = 0 \tag{3.40}$$

where α_i (i=1, 2, 3) depends on the material parameters and the wave number.

3.7.4 *Instability of the material system*

In the following, we discuss the instability of the material system. If the growth rate of perturbation ω, which is the root of Eq. (3.40), is positive, the material system is unstable. On the other hand, if ω is negative, the material system is stable. In order to investigate whether ω is negative or positive, we adopt the Routh-Hurwitz criteria. The roots of Eq. (3.40) have negative real parts when the coefficients of the characteristic polynomial satisfy

$$\alpha_1 > 0, \ \alpha_2 > 0, \ \alpha_3 > 0, \ \alpha_1\alpha_2 - \alpha_3 > 0 \tag{3.41}$$

Since similar results have been obtained for the elasto-viscoplastic case, the results for the rigid viscoplastic model will be shown in the following (Higo et al., 2005a).

1) Rigid-viscoplastic model without a gradient term

In order to study the instability of the material system more simply, we herein assume a rigid-viscoplastic constitutive model that is achieved by $G \to \infty$ and $K \to \infty$.

With this assumption and $\det[A] = 0$, we obtain

$$\omega = \frac{-(4G'' + K')}{2\gamma_w/kq^2 + (4\mu + \mu'_k)} \tag{3.42}$$

As shown in Eq. (3.42), in the case of the analysis with a rigid-viscoplastic model, we can discuss not only whether or not speed of fluctuation ω is positive, but also whether or not the quantity of ω is dependent on the permeability. For example, when ω is negative, namely, the material system is stable, the material with a larger ω can reach the stable state earlier than that with a smaller ω. This means that the material with a larger ω (negative) is more stable than that with a smaller ω (negative). On the other hand, the material with a larger ω (positive) is more unstable than that with a smaller ω (positive), since the former becomes unstable earlier than the latter.

In the case of $G'' > 0$, the viscoplastic-hardening case, ω becomes negative. These results are the same as those of the elasto-viscoplastic model, but further discussions can be conducted as follows. When k is relatively smaller, ω becomes smaller. The system then becomes relatively less stable. When k is relatively larger, however, ω becomes larger and the system becomes relatively more stable.

In the case of viscoplastic softening, namely, $G'' < 0$, ω becomes positive. In this case, when k is relatively smaller, ω becomes smaller. The system then becomes relatively less unstable. When k is relatively larger, however, ω becomes larger, and the system becomes relatively more unstable. These results obtained in the viscoplastic softening region are consistent with those for the case of the elasto-viscoplastic model.

An instability analysis using a rigid-viscoplastic model, disregarding the effects of elasticity on instability, provided an additional conclusion that the material with lower permeability levels is relatively less stable than that with higher permeability levels in the strain-hardening range. From Eq.(3.42), it is worth noting that the unbounded growth of the fluctuation does not occur even when $q \to \infty$ or $k \to \infty$ for viscous materials. The presence of viscous effects delays the instability as already pointed out by Leroy (1991) for single materials.

2) Gradient-dependent rigid-viscoplastic model

In the case of the gradient-dependent rigid-viscoplastic model, we have obtained a growth rate of fluctuation ω as

$$\omega = \frac{-(4G'' + K' + a_3q^2)}{2\gamma_w/kq^2 + (4\mu + \mu'_k)} \tag{3.43}$$

Even though $G'' < 0$ in the strain-softening regime, the numerator can be negative when $a_3 > 0$ is large enough and/or q is large, that is, the wave length is small enough. In other words, the material system can be stable even in the case of $G'' < 0$ if the gradient term is large enough. In any case, the gradient term can act as a stabilizer in the analysis, as has been observed in

previous analyses (see Aifantis et al., 1999 and Oka et al., 2000b). Similar results have been obtained for elasto-viscoplastic cases (Higo et al., 2005a).

3.8 *Finite element analysis of a fluid-saturated material modeled by a gradient-dependent elasto-viscoplastic model*

A finite element formulation for two-phase mixtures, based on the finite deformation theory, is shown in this section. Biot's two-phase mixture theory (1962) is adopted to give the governing equations for soil-water coupling problems (Oka et al., 2002b; Kimoto et al., 2004; Higo et al., 2005a). For simplified and practical formulations, both the grain particles and the fluid are assumed to be incompressible.

The strain localization phenomenon is a geometrically nonlinear problem since the deformation of shear bands is large. In addition, the constitutive equation for clay used in this study is nonlinear and is defined in an incremental form. In order to deal with such a nonlinear large deformation problem, using an incremental constitutive model, an updated Lagrangian method with the objective Jaumann rate of Cauchy stress is used for the weak form of the rate type of equilibrium equations. As for the element type, an eight-node quadrilateral isoparametric element with a reduced Gaussian four-point integration is used for the displacement in order to eliminate shear locking as well as to reduce the appearance of a spurious hourglass mode. The pore-water pressure is defined by a four-node quadrilateral isoparametric element. In this section, direct notation is used for vectors and tensors; the notation is indicated by boldface letters. A dot denotes a contraction of inner indices, e.g., $a_i b_i \equiv a \cdot b$, so that $A_{ij}B_{ij} \equiv A : B$.

3.8.1 *Equilibrium equations for the fluid-solid mixture*

In this study, we deal with static and small scale problems, so that the acceleration and the body force can be assumed to be zero. Consequently, this assumption provides a rate type of equilibrium equations for the fluid-solid mixture as follows:

$$\mathrm{div}\dot{S}_t = 0 \tag{3.44}$$

where $\dot{S}_t$ is the total nominal stress rate tensor (Yatomi et al., 1989).

The effective nominal stress rate tensor, $\dot{S}'_t$, is given by the following equation:

$$\dot{S}'_t = \dot{\sigma}' + \sigma' \mathrm{tr}L - \sigma' L^{\mathrm{T}} \tag{3.45}$$

where σ' is Terzaghi's effective stress defined by Eq. (3.16), L is the velocity gradient tensor, and the superimposed dot indicates the time differentiation..

The relation between $\dot{S}_t$ and $\dot{S}'_t$ is given as follows:

$$\dot{S}_t = \dot{S}'_t + \dot{u}_w I + U \tag{3.46}$$

$$U = \mathrm{tr}L u_w I - u_w I L^{\mathrm{T}} \tag{3.47}$$

where u_w is the pore-water pressure and I is the second order identity tensor.

When we consider closed domain D , the weak form of the rate type of equilibrium equations is given as follows:

$$\int_D \mathrm{div}\dot{S}_t \cdot \delta v \, dv = 0 \tag{3.48}$$

in which δv is the virtual velocity vector.

The displacement boundary is denoted by ∂D_u if the displacement is prescribed; ∂D_t denotes a traction boundary if the traction is prescribed.

$$v = \overline{v} \quad \text{on} \quad \partial D_u \,, \quad \dot{S}_t n = \overline{\dot{s}}_t \quad \text{on} \quad \partial D_t \tag{3.49}$$

in which v is the velocity vector, n indicates the unit normal to the body, $\dot{s}_t$ is the nominal traction rate vector, and the specified values are designated by a superposed bar.

Using Eqs. (3.45), (3.46), and (3.47) and taking account of the boundary conditions, the weak form of the rate equilibrium equation, Eq. (3.48), becomes

$$\int_D \dot{\sigma}' : \delta D \, dv + \int_D (\sigma' \mathrm{tr}D) : \delta L \, dv - \int_D (\sigma' L^{\mathrm{T}}) : \delta L \, dv + \int_D \dot{u}_w \mathrm{tr}\delta D \, dv$$

$$+ \int_D U : \delta L \, dv - \int_{\partial D_t} \overline{\dot{s}}_t \cdot \delta v \, ds = 0 \tag{3.50}$$

in which D is the stretching tensor.

The elasto-viscoplastic constitutive model is written as

$$\hat{\sigma}' = C : D - Q \tag{3.51}$$

where $\hat{\sigma}'$ is the Jaumann rate of the effective Cauchy stress tensor, Q is the relaxation stress tensor, and C is the tangential stiffness of the fourth order tensor. Herein, the tangent modulus method (Peirce et al. 1984) is adopted in order to evaluate visco-plastic stretching tensor D^{vp} (see Oka et al., 1992b).

With the definition of Jaumann rate of effective stress, we have

$$\{\dot{\sigma}'\} = [C]\{D\} - \{Q\} + \{W^*\} \tag{3.52}$$

where $[C]$ is the tangential stiffness matrix and $\{Q\}$ is the relaxation stress vector. $\{W^*\} = W_{ik}\sigma'_{kj} - \sigma'_{ik}W_{kj}$ is the vector related to the spin tensor.

By all the matrix and vector relations obtained previously, and based on the theory of virtual displacement, we have obtained the following weak form of the equilibrium equations:

$$[K]\{v^*\} - \int_D [B]^{\mathrm{T}} \{Q\} \, dv + \int_D [B]^{\mathrm{T}} \{W^*\} dv + [K_L]\{v^*\} + [K_v]\{\dot{u}_w^*\} = \{\dot{F}\} \tag{3.53}$$

where $[K]$ is the stiffness matrix, $[B]$ is the B matrix, and $[K_v]$ and $[K_L]$ are related matrixes.

3.8.2 *Continuity equation*

Darcy's law and the conservation of mass for the mixture give the continuity equation as

$$\frac{k}{\gamma_w}\nabla^2 u_w + \mathrm{tr}D = 0 \tag{3.54}$$

where k is the coefficient of permeability, γ_w is the unit weight of the pore water, and D is the stretching tensor.

Considering the test function of $\hat{u}_w$, we can obtain the weak form of the continuity equation as

$$\frac{k}{\gamma_w}\int_D \nabla^2 u_w \hat{u}_w \, dv + \int_D \mathrm{tr}D \, \hat{u}_w \, dv = 0 \tag{3.55}$$

∂D_p is the boundary where the pore pressure is specified and ∂D_v is the boundary where the flow of water is specified.

$$u_w = \overline{u}_w \quad \text{on} \quad \partial D_p \qquad \frac{k}{\gamma_w}\nabla u_w = \overline{v}_f \quad \text{on} \quad \partial D_v \tag{3.56}$$

in which the specified values are designated by a superposed bar and $\overline{v}_f$ is the velocity of the pore water through the boundary surface.

After manipulation, the finite element discretization of the continuity equation is obtained as follows:

$$[K_v]^{\mathrm{T}}\left\{v^*\right\}-[K_h]\left\{u_w^*\right\}=[V] \tag{3.57}$$

$$[K_h]=\frac{k}{\gamma_w}\int_D[B_h]^{\mathrm{T}}[B_h]dv \tag{3.58}$$

3.8.3 *Finite element formulation of the gradient-dependent elasto-viscoplastic model*

For the higher order gradient-dependent constitutive equations, a second order gradient of viscoplastic volumetric strain v^p is used in the constitutive equation. In order to obtain the second order gradient by the finite element method, the discretization of v^p as an independent variable by the eight-node quadrilateral element is needed. Hence, we assume the weak form of the yield function and define viscoplastic volumetric strain v^p at each node in the same manner as that by Aifantis et al. (1999).

In order to obtain the weak form of the yield function, we adopt a Taylor series expansion around the current state and consider the first term. We can rewrite the yield function as

$$\dot{v}^p=G(\sigma'_{ij},\, v^p,\, \nabla^2 v^p) \tag{3.59}$$

Expanding the viscoplastic volumetric strain rate in a Taylor series and disregarding the second and higher order terms, we obtain a linearized yield function in the form

$$\dot{v}^p=\dot{v}_0^p+\left([G_\sigma][\dot{\sigma}']+G_{v^p}\dot{v}^p+G_\beta(\nabla^2\dot{v}^p)\right) \tag{3.60}$$

where

$$G_\sigma=\frac{\partial G}{\partial \sigma'_{ij}},\quad G_{v^p}=\frac{\partial G}{\partial v^p},\quad G_\beta=\frac{\partial G}{\partial(\nabla^2 v^p)} \tag{3.61}$$

$\dot{v}_0^p$ denotes the value of the volumetric strain rate at the current state. Using a Taylor series expansion and truncating the first order term, we obtain the following expression for the total strain rate tensor.

From Eq. (3.60), stress rate tensor $[\dot{\sigma}']$ is obtained as

$$[\dot{\sigma}']=[L][\dot{\varepsilon}]-[L][\dot{\varepsilon}_0^p]-[L][A]\dot{v}^p-[L][A^{**}]\nabla^2\dot{v}^p \tag{3.62}$$

$$[L]^{-1}=[L^*]^{-1}+[A^*] \tag{3.63}$$

where $[\dot{\varepsilon}]$ is the total strain rate tensor, $[\dot{\varepsilon}_0^p]$ is the viscoplastic strain rate tensor at the current state.

3.8.4 *Strain localization analysis by the gradient-dependent elasto-viscoplastic model*

Effects of permeability

In Fig. 3.4, the boundary conditions are shown for the plane strain problem used in the numerical analysis, while the parameters used in the computation are shown in Table 3.2. The gradient parameter, in principle, can be determined by the width of the shear band, namely, the wavelength of the localized pattern. The strain rate of the compression is 1.0%/min. The horizontal displacement at the top and the bottom of the specimen was fixed as a trigger of the localization. All of the boundaries are assumed to be impermeable, while the pore fluid is allowed to flow in the specimen.

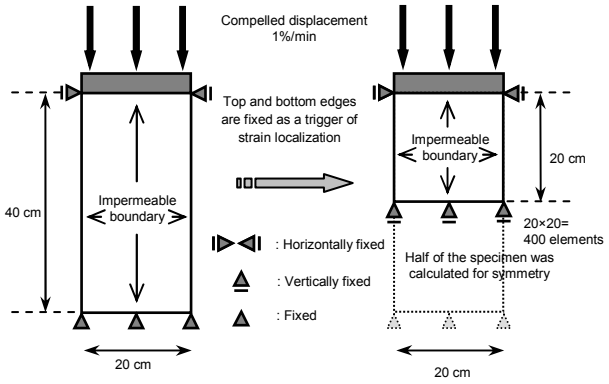

Figure 3.4. Boundary conditions and the size of the specimen.

Table 3.2: Material parameters for the strain localization analysis with different permeability coefficients

Compression index λ	0.172
Swelling index κ	0.054
Initial void ratio e_0	1.28
Initial mean effective stress σ'_{me}	200 (kPa)
Coefficient of earth pressure at rest K_0	1.0
Viscoplastic parameter m'	21.5
Viscoplastic parameter C	4.5×10^{-8} (1/s)
Stress ratio at failure M_f^*	1.05
Elastic shear modulus G	5500 (kPa)
Softening parameter G_2^*	100
Gradient parameter a_3	0.0, 5.0, 30.0 ($\times10^{-4}$m^2)
Coefficient of permeability $k_x=k_y$	1.54×10^{-6}, $\times10^{-8}$, $\times10^{-12}$

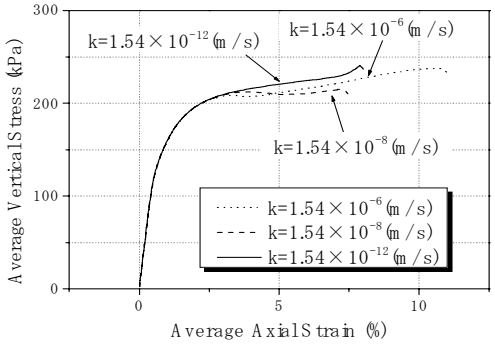

Figure 3.5. Average vertical stress-strain relations with different coefficients of permeability.

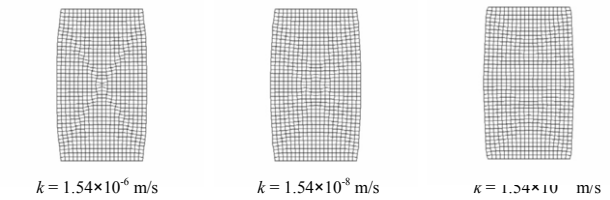

Figure 3.6. Deformed mesh at an average axial strain of 7%.

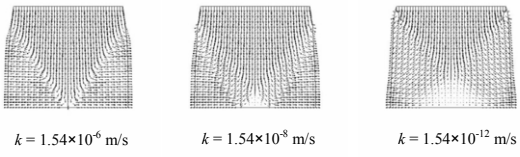

Figure 3.7. Distribution of the velocity vector at an average axial strain of 7%.

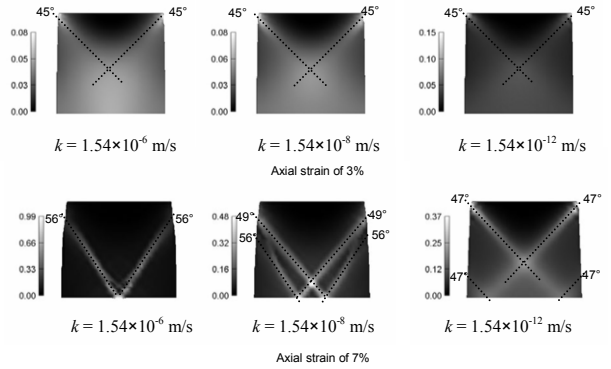

Figure 3.8. Distribution of γ^p at an average axial strain of 3% and 7%.

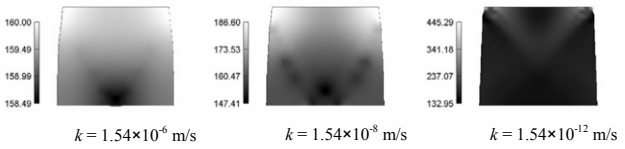

Figure 3.9. Distribution of pore water pressure at an average axial strain of 7% (unit: kPa).

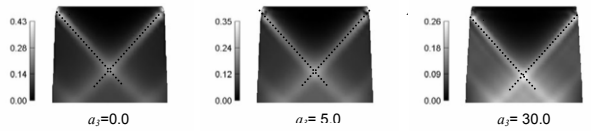

Figure 3.10. Distribution of γ^p at an average axial strain of 7% (k = 1.54 × 10^{-8} cm/s).

The average vertical stress vs. strain relations with different coefficients of permeability are shown in Fig. 3.5. In the early stage of loading, i.e., in the hardening range, little difference can be seen among these three cases. On the other hand, in the strain-softening range, the material with a low permeability level of 1.54×10^{-12} (m/s) is less unstable i.e., it is relatively stable because the average stress is larger than materials with higher permeability levels of $\times10^{-6}$ (m/s) and $\times10^{-8}$ (m/s) before an average axial strain of 5%. This behavior is consistent with the theoretical consideration mentioned in Section 3.7. After an axial strain of 5%, however, the average stress in the case of $\times10^{-8}$ (m/s) is smaller than that in the case of $\times10^{-6}$ (m/s). These results indicate that a material with a small permeability coefficient is not necessarily more stable than one with a larger permeability coefficient.

The calculations with coefficients of permeability of $k=1.54\times10^{-8}$ (m/s) and 10^{-12} (m/s) diverged around 8% of the axial strain. The calculations with $k=1.54\times10^{-6}$ (m/s) also diverged around 11% of the axial strain. This may be because the constraint conditions, i.e., no lateral displacements at either the top or the bottom plates, induce numerical instability near the top and the bottom of the specimen. Fig. 3.6 shows the deformed mesh at an average axial strain of 7% with different coefficients of permeability k . It is shown that the pore fluid has an apparent influence on the formation of shear bands. It is found that a symmetrical deformation can be seen in all cases, in particular, a clear shear band formed in the case of $k=1.54\times10^{-6}$ (m/s). In Fig. 3.7, velocity vectors are shown in half of the specimens at an average axial strain of 7% with different coefficients of permeability k . Discontinuous distributions of velocity fields are found in all cases due to the formation of shear bands. The patterns of distributions of the velocity vectors are consistent with the deformed mesh.

Fig. 3.8 shows the distributions of accumulated viscoplastic shear strain γ^p at an average axial strain of 3% and that of 7% with different coefficients of permeability k . γ^p is defined as follows:

$$\gamma^p=\int d\gamma^p,\quad d\gamma^p=(de_{ij}^p de_{ij}^p)^{1/2} \tag{3.64}$$

where de_{ij}^p is the viscoplastic deviatoric strain-increment tensor. The localized patterns of the figures for 3% are very similar to each other, but the maximum value for γ^p is larger as the coefficient of permeability k decreases. On the other hand, at an average axial strain of 7%, the maximum value for γ^p is larger in the case of higher coefficients of permeability than that of lower coefficients of permeability. It can be said that materials with larger accumulated shear strain are more unstable than those with smaller shear strain. Following this point of view, when the average axial strain is small, i.e., in the viscoplastic-hardening area, materials with lower permeability levels are rather unstable. On the other hand, when the average axial strain becomes large, i.e., in the viscoplastic-softening area, materials with higher permeability levels are relatively unstable. This tendency is also consistent with the results obtained in Section 3.7. In addition, a larger difference between the maximum and the minimum values for γ^p is also seen in the case of higher permeability levels. This suggests that the strain localizes prominently when materials have high permeability levels. It is interesting, however, that two shear bands appear in the case of $k=1.54\times10^{-6}$ (m/s), while the other cases have four shear bands and the distance between two shear bands is larger in the case of small permeability compared with the case of larger permeability.

The inclination angles of the shear bands for all cases are 45 degrees at the small axial strain of 3%. When the axial strain becomes 7%, the angles of the shear bands with higher permeability become larger than those with lower permeability. Oka et al. (1995) demonstrated that the preferred orientation for the shear bands is 45 degrees under plane strain locally undrained conditions, i.e., $k=0$, for Adachi and Oka's viscoplastic model introduced in Section 3.7. The reasons why the angles of shear bands with lower strain are proximate to 45 degrees than materials with lower permeability levels are similar to those under locally undrained conditions. In Fig. 3.9, the distributions of pore-water pressure are shown with different coefficients of permeability k . When permeability k is smaller, the pore-water pressure is more localized. This trend is similar to the results obtained by Oka et al. (1995).

The distributions of mean effective stress, the second invariant of deviatoric stress, and the volumetric viscoplastic strain are all affected by the formation of shear bands and are inhomogeneous. The mean effective stress inside the shear band becomes smaller than that outside the shear band. The maximum values for the deviatoric stress and the volumetric viscoplastic strain become larger with higher permeability levels.

Effects of the strain gradient parameter

Strain gradients, in principle, can describe the thickness of shear bands. In addition, it is found in the instability analysis of Section 3.7 that strain gradients act as stabilizers. In this section, the effects of the strain gradient parameter on the strain localization analysis are investigated. The boundary conditions and the

material parameters are the same as those mentioned in the last section. Fig. 3.10 depicts the distributions of accumulated visco-plastic shear strain γ^p at an average axial strain of 7% with different gradient parameters. In this case, $k = 1.54 \times 10^{-10}$ (m/s). It can be found from the figure that the thickness, the spacing of the shear bands, and the extent of the strain localization also depend on gradient parameter a_3. The accumulated strain is more localized when gradient parameter a_3 is rather small. This suggests that the gradient term makes the system more stable. The distance between shear bands will decrease with gradient parameter a_3, while the angles of the shear bands are consistently 48 degrees.

Effect of the heterogeneity of the soil properties

The boundary conditions are shown in Fig. 3.11, while Table 3.3 shows the material parameters used in the analysis in this section. We assumed three cases of distribution for the stress ratio at failure, M_f^*, as shown in Fig. 3.12. The perturbation of M_f^* was obtained using a pseudo-random number by the linear congruential method.

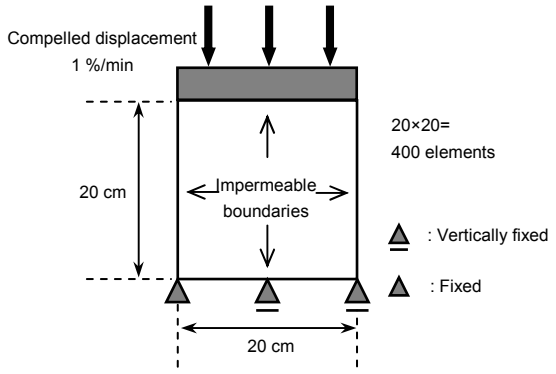

Figure 3.11. Boundary conditions and the size of the specimen (undrained plane strain condition).

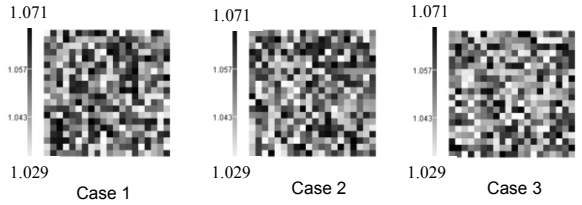

Figure 3.12. Initial distribution of M_f^* (R=2.0%).

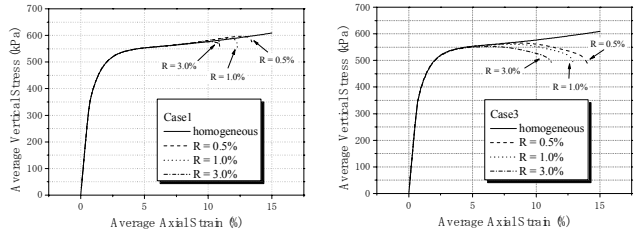

Figure 3.13. Stress-strain curves for Case 1 and Case 3 obtained by different R.

In Fig. 3.13, the stress-strain relations for Cases 1-3 are obtained by the different ranges in perturbation of M_f^*, R; $R = 0.5\%$, 1.0%, and 3.0%. $R = 0\%$ means a homogeneous clay sample. The applied strain rate is 1.0/min. The effects of heterogeneity on the stress-strain relations are dependent on the initial distribution of M_f^*. It can be seen in Case 1 that the average vertical stress of the non-homogeneous clay is a little larger than that of the homogeneous clay, but that it becomes smaller in the failure state. On the other hand, the heterogeneous clay in Case 3 shows softening behavior and the average stress is smaller than that of the homogeneous clay. The axial strain at the failure state is consistently smaller as the range of perturbation R is larger. Fig. 3.14 shows the deformed mesh and the distributions of γ^p for a homogeneous one and for Case 1 with different R at an average axial strain of 10%. Regarding the homogeneous case, the deformation and the distribution of γ^p are uniform in the specimen. On the contrary, localized deformations are seen in the non-homogeneous clay and the shear band of $R = 3\%$ is clearer than the others. Similar results have been obtained by Ehlers and Volk (1998). They showed that a random distribution of the Lamé constant within local deviations of $\pm$ 0.5% provide clear shear bands under plane strain conditions, although the homogeneous specimens do not.

Table 3.3: Material parameters for the strain localization analysis of homogeneous and heterogeneous types of clay

Compression index λ	0.372
Swelling index κ	0.054
Initial void ratio e_0	1.28
Initial mean effective stress σ'_{me}	600 (kPa)
Coefficient of earth pressure at rest K_0	1.0
Viscoplastic parameter m'	21.5
Viscoplastic parameter C	4.5×10^{-8} (1/s)
Stress ratio at failure M_f^*	1.05
Elastic shear modulus G	13210 (kPa)
Softening parameter G_2^*	100
Gradient parameter a_3	0.0 (m^2)
Coefficient of permeability $k_x = k_y$	1.16×10^{-14} (m/s)

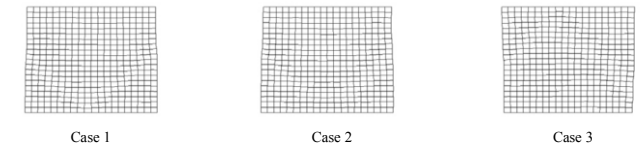

(i) Deformed mesh at an average axial strain of 10%

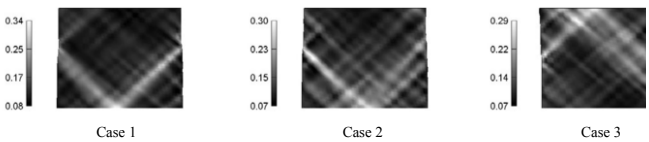

(ii) Distribution of γ^p at an average axial strain of 10%

Figure 3.14. Deformed mesh and the distribution of γ^p for Case 1, 2, and 3 (R=2.0%).

Mesh-size dependency

Finally we should discuss the mesh-size dependency of the present analysis. It is well known that the finite element analysis has an inherent mesh-size dependence and that many researchers have studied regularization methods. One method is to introduce the rate dependency of the material through the use of an elasto-viscoplastic model or regularization in the numerical analysis (e.g. Hughes and Taylor, 1978). The second method is to introduce higher order strain gradients into the constitutive model (e.g. Aifantis, 1984). The third approach is to incorporate a Darcy type of soil-fluid interaction which can alleviate the problem of instability by delaying the onset of material instability (e.g., Rice, 1975). Herein, mesh-size dependency is small since an elasto-viscoplastic model with the second-order strain gradient and a solid-fluid mixture theory was applied. Oka et al. (2002b) found that the analysis method has no significant mesh-size dependency. It is worth noting that Zhang and Shrefler (2000) have shown that gradient dependence and permeability

can regularize the finite element solution and that the second sometimes prevails over the first.

3.9 *Three-dimensional strain localization analysis of water-saturated clay*

Since strain localization is a precursor of failure, strain localization is an important subject in geomechanics. Strain localization has been analyzed for geomaterials by many researchers. Many of them, however, were treated as two-dimensional problems although the phenomena are generally three dimensional. In order to investigate the strain localization behavior of geomaterials under three-dimensional conditions, undrained triaxial compression tests using rectangular specimens and their simulation by a finite element analysis using an elasto-viscoplastic model have been conducted. In the experiments, both normally consolidated and overconsolidated clay samples were tested with different strain rates (Kodaka et al., 2001; Oka et al., 2005c). Using the distribution of shear strain obtained by the image analysis of digital photographs taken during deformation, the effects of the strain rates, the dilatancy, and the overconsolidation on strain localization are studied in detail. The method of numerical simulation is a soil-water coupled finite element method which is based on the finite deformation theory, using an elasto-viscoplastic model for water-saturated clay considering structural changes.

3.9.1 *Undrained triaxial compression tests for clay using rectangular specimens*

Clay samples and the testing program

The clay used in the experiment is Fukakusa clay which is a Pleistocene marine clay produced in the southeastern part of the Kyoto Basin. Liquid limit $w_L = 62$ %, plasticity index $I_p = 33$, and the density of soil solid $\rho_s = 2.69$ g/cm. Reconstituted clay samples were prepared by remolding them in slurry and then pre-consolidating them. The specimens were consolidated one dimensionally at a pre-consolidation pressure of 98 kPa. The pre-consolidated specimens were covered with paraffin and not to be disturbed. The scale of the transverse section is 4cm × 4 cm and the height is 8 cm (see Fig. 3.15). The test cases are listed in Table 3.4. All the specimens used in the present study were saturated by the double vacuum method and were acted upon by 200 kPa of back pressure. The normally consolidated clay specimens were isotropically consolidated to 200 kPa. The overconsolidated clay specimens were isotropically consolidated to 300 kPa, and then isotropically swelled to 50 kPa. Therefore, the overconsolidation ratio (OCR) is 6. After the consolidation or the swelling procedure, axial pressure was applied under undrained conditions by an axial loading device with an axial strain or displacement control system. The three axial strain rates monotonically applied in the tests were 1%/min, 0.1%/min, and 0.01%/min. The tests were stopped at an axial strain of 20%.

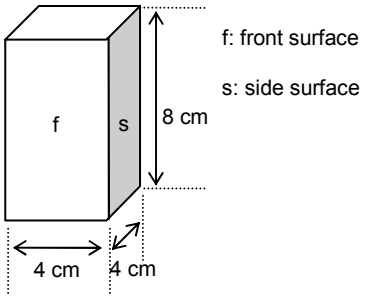

Figure 3.15. Sizes of the specimens.

Table 3.4: Test cases

Normally consolidated clay		
$\sigma'_{m0} = 200$ kPa (Consolidation pressure)		
No.	Sizes (cm)	Strain rate (%/min)
NC-1	4×4×8	1
NC-2	4×4×8	0.1
NC-3	4×4×8	0.01

Overconsolidated clay		
$\sigma'_{mc} = 300$ kPa (Pre-consolidation pressure) $\sigma'_{m0} = 50$ kPa (Swelling pressure), OCR = 6		
No.	Sizes (cm)	Strain rate (%/min)
OC-1	4×4×8	1
OC-2	4×4×8	0.1
OC-3	4×4×8	0.01

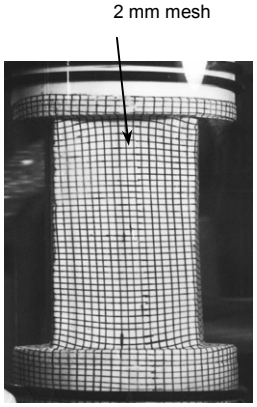

Photo 1. An example of the photographs taken through the acrylic cell

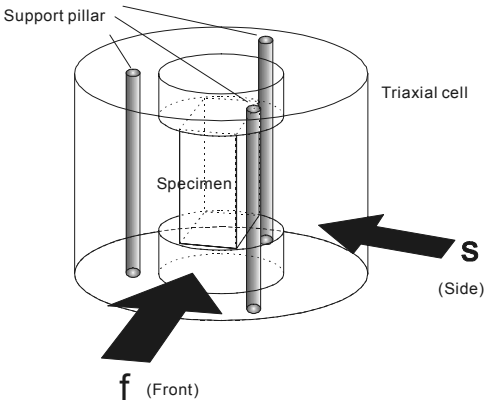

Figure 3.16. Schematic figure of the photography.

Image analysis

We drew 2 mm square meshes on the rubber membranes covering the specimen. A digital camera was used to take photographs of two surfaces of the specimens during the tests**.** Photo 1 and Fig. 3.16 show a sample of the digital photographs taken through the triaxial cell and a schematic figure of the photography, respectively. After correcting the effects of the refraction, we digitized the nodal coordinates of the meshes. Using the coordinates at the initial state, i.e., before the undrained loading, and those of each axial strain level, the nodal displacements were calculated. Adopting the B matrix for the four-node isoparametric finite elements provided the strain of each element (Kodaka et al., 2001; Oka et al., 2005c).

3.9.2 *Three-dimensional soil-water coupled finite element analysis method*

We formulated a three-dimensional finite element method, based on Biot's two-phase mixture theory and the finite deformation theory, to simulate the three-dimensional strain localization tests for rectangular-shaped clay specimens. The strain localization phenomenon is a geometrically nonlinear problem since the deformation in a shear band is large. In addition, the constitutive equation for clay used in this study is nonlinear and is defined in an incremental form. In order to deal with such a nonlinear large deformation problem using an incremental constitutive model, an updated Lagrangian method with the objective Jaumann rate of Cauchy stress is used for the weak form of the rate type of equilibrium equations. As for the element type, a 20-node quadrilateral isoparametric element with a reduced Gaussian four-point integration is used for the displacement in order to eliminate shear locking as well as to reduce the appearance of a spurious hourglass mode. The pore-water pressure is defined by an 8-node quadrilateral isoparametric element. The formulation of the three-dimensional soil-water coupled finite element analysis method is the same as those presented in the last section. Detailed formulations are in the references (e.g., Oka et al., 2002b; Higo, 2003; Higo et al., 2004; Higo et al., 2005b).

3.9.3 *Numerical simulation of triaxial tests for rectangular specimens*

1) Determination of the material parameters

The material parameters required by the constitutive model introduced in the last section are listed in Table 3.5. We determined λ to be 0.191 and κ to be 0.043 using the isotropic consolidation and the swelling test results for Fukakusa clay. For initial void ratio e_0, we used the average of them obtained in each test, i.e., 1.10 for normally consolidated clay and 1.11 for overconsolidated clay, since calculating with different void ratios is not appropriate for a comparison of the simulation results.

Initial elastic shear modulus G_0 is determined by the initial slope of the undrained triaxial compression tests, namely, $G_0 = \Delta q/(3\Delta\varepsilon_{11})$, in which Δq is the increment in deviator stress and $\Delta\varepsilon_{11}$ is the increment in axial strain. In this study, $\Delta\varepsilon_{11}$ was determined to be 0.1%. G_0 is dependent on the strain rate because of the visco-elastic properties. Compression yield stress σ'_{mbi} is assumed to be the pre-consolidation stress. Therefore, that of normally consolidated clay is 200 kPa and that of overconsolidated clay is 300 kPa. The stress ratio at maximum compression M_m^* is defined as the stress ratio whereby maximum compression occurs in the drained compression tests. Herein, M_m^* is assumed to be determined from the stress ratio at the residual state in the undrained triaxial compression tests.

Viscoplastic parameters m' and C can be determined from undrained triaxial tests with different strain rates. Adachi and Oka (1982) noted that viscoplastic parameter m' is estimated from the slope of the relation between the stress ratio and the logarithm of the strain rate. In principle, material parameters are determined from elemental tests. In this study, however, undrained triaxial compression tests using cylindrical specimens were conducted only for a strain rate of 1.0%/min, since we could not prepare sufficient numbers of specimens for the tests using cylindrical specimens which are consolidated under the completely same conditions. Hence, we applied the test results using rectangular specimens (4cm × 4cm × 8cm) to estimate viscoplastic parameter m' (Higo, 2003).

Fig. 3.17 shows the relations between the applied strain rates and stress ratio q/σ'_m in which q is the deviator stress and σ'_m is the mean effective stress. For normally consolidated clay, we plotted the stress ratios at $\sigma'_m = 0.7\sigma'_{m0}$, and estimated m' to be 24.3. As for the overconsolidated clay, m' is estimated to be 20.5 from the stress ratios at $\sigma'_m = 2.0\sigma'_{m0}$. After m' is fixed, viscoplastic parameter C is determined by the peak stress.

Structural parameter σ'_{maf} can be obtained by the deviator stress at the residual stress state, while β, which dominates the decreasing rate of deviator stress.

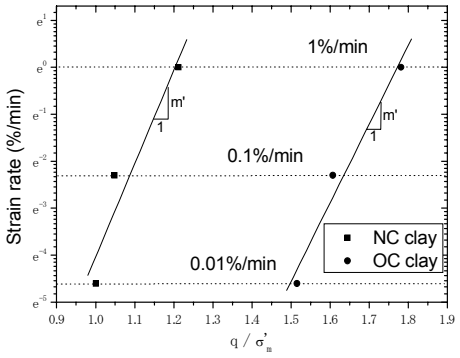

Figure 3.17. Relations between the logarithm of the strain rate and the stress ratio (NC clay: σ'_m =0.7 σ'_{m0}, OC clay: σ'_m =2.0 σ'_{m0}).

Table 3.5: Material parameters used in the numerical simulation

Parameter		N.C. clay	O.C. clay
Compression index λ		0.191	0.191
Swelling index κ		0.043	0.043
Initial void ratio e_0		1.10	1.11
Initial elastic shear modulus G_0	0.01%/min	16300 (kPa)	9190 (kPa)
	0.1%/min	17700 (kPa)	9920 (kPa)
	1%/min	23400 (kPa)	13080 (kPa)
Initial mean effective stress σ'_{m0}		200 (kPa)	50 (kPa)
Compression yield stress σ'_{mbi}		200 (kPa)	300 (kPa)
Coefficient of earth pressure at rest K_0		1.0	1.0
Stress ratio at maximum compression M_m^*		1.14	1.14
Viscoplastic parameter m'		24.3	20.5
Viscoplastic parameter C		5.8×10^{-10} (1/s)	2.7×10^{-9} (1/s)
Structural parameter σ'_{maf}		170 (kPa)	270 (kPa)
Structural parameter β		10	5
Coefficient of permeability k		1.63×10^{-9} (m/s)	2.86×10^{-9} (m/s)

2) Boundary conditions

Fig. 3.18 shows the boundary conditions, which are set up according to the same boundary conditions as those of the undrained triaxial compression tests with displacement control. All the boundaries are assumed to be impermeable, however, the transport of pore water between each element is allowed. Constant displacements (z-direction) of 0.01%/min, 0.1%/min, and 1%/min are applied to the nodes on the bottom surface. The time increment is determined by the increment of average strain $\Delta\varepsilon = 0.05\,\%$. As for the top and the bottom surfaces, frictional force occurs between the top and the bottom surfaces and the top cap and the pedestal. Hence, the top and the bottom surfaces deform. However, it is difficult to accurately estimate the friction force. In addition, the displacements of the top and the bottom surfaces, which were measured after the tests (see Higo, 2003), are rather small. Consequently, we assumed that the horizontal (x-direction and y-direction) displacement of the nodes on both the top and the bottom surfaces is constrained.

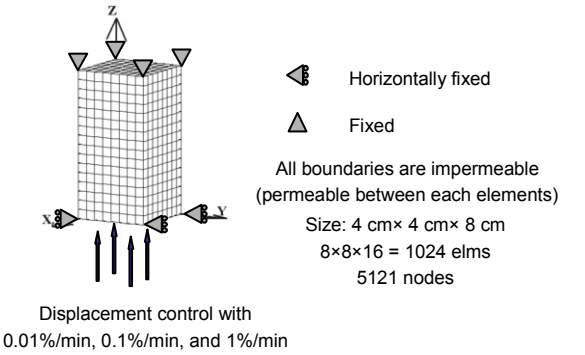

Figure 3.18. Boundary conditions for three-dimensional finite element analysis.

3) Comparison between the experimental results and the simulation results

Undrained triaxial compression tests for normally consolidated clay and overconsolidated clay with different axial strain rates have been simulated. Figs. 3.19 and 3.20 show the experimental results and the simulation results for normally consolidated clay and overconsolidated clay, respectively.

Stress-strain relations and effective stress paths

Figs. 3.19(a) and 3.20(a) illustrate the stress-strain relations for both the simulation and the experiment. The deviator stress, the mean effective stress, and the pore-water pressure used in the stress-strain curves and the effective stress paths for simulation results are calculated in the same manner as the experimental data. The deviator stress and the pore-water pressure are obtained using the average of those nodal values of the top surface.

We can see that the stress-strain relations for both the experiment and the simulation are greatly dependent on the strain rate and the dilatancy characteristics. In the experimental results, we can also observe gradual strain-softening behavior for both normally consolidated clay and overconsolidated clay. On the other hand, in the case of the simulation, it is seen that the stress-strain relations for normally consolidated clay consistently show strain-hardening behavior, while those for overconsolidated clay show strain-softening behavior just after the peak stress around an axial strain of 2%, and then they show a gradual hardening.

It is seen in Figs. 3.19(b) and 3.20(b) that the effective stress paths for normally consolidated clay exhibit negative dilatancy, i.e., a decrease in mean effective stress, while those for overconsolidated clay exhibit positive dilatancy, i.e., an increase in mean effective stress.

We can say that the stress-strain curves and the effective stress paths for normally consolidated clay are well reproduced by the presented analysis method. However, there are some differences between the experiment and the simulation for both cases. We would say that the differences can be improved by the inverse analysis technique to accurately determine the input parameters.

Distribution of shear strain

Figs. 3.19(c) and 3.20(c) show the distributions of shear strain γ for the experiment, and Figs. 3.19(e) and 3.20(e) are those for the simulation. Figs. 3.19(d) and 3.20(d) are the pictures taken after the tests, and Figs. 3.19(f) and 3.20(f) indicate the deformed meshes at an axial strain of 20%. In these figures, 's' and 'f' indicate the 'side surface' and the 'front surface' of the specimens, respectively (see Fig. 3.15).

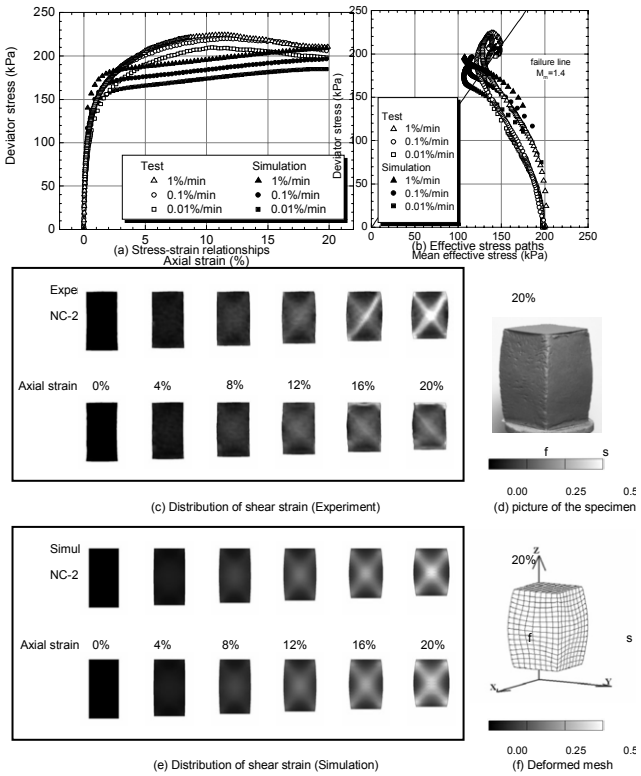

Figure 3.19. Comparison between the experimental results and simulation results (NC clay, 0.1%/min).

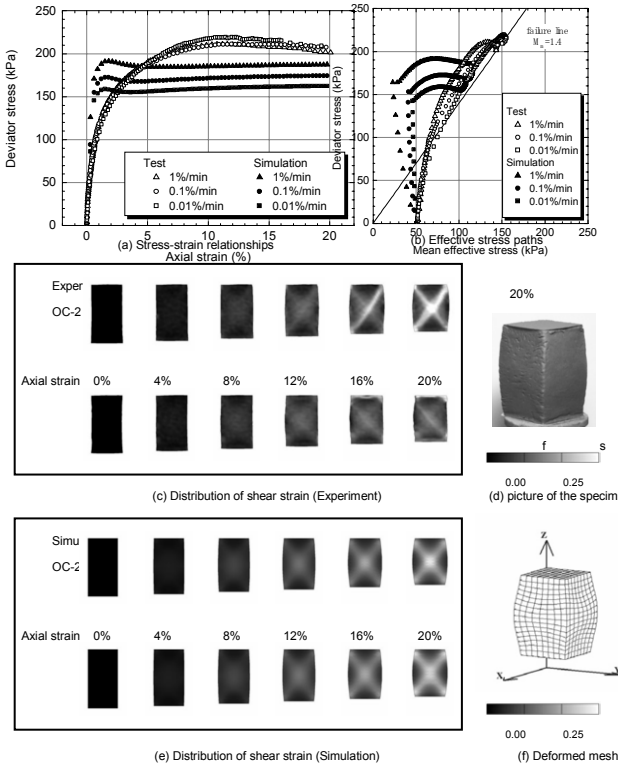

Figure 3.20. Comparison between the experimental results and simulation results (OC clay, 0.1%/min).

In order to obtain the distributions of shear strain γ on the surfaces of the specimens for simulation results, we used a special method, which is the same method as that for experiment.

We can see in the experimental results (Figs. 3.19(c) and 3.20(c)) that strain localization starts at an axial strain of 8% and that shear bands are clearly seen at an axial strain of 12%. In addition, shear bands develop from the edges of the top and the bottom of the specimens since the friction force generated between the specimen and the top cap or the pedestal acts as a trigger of strain localization. As the axial strain becomes large, clear shear bands appear on the side surface and the front surface, and develop with increases in the thickness of the shear bands.

As shown in Figs. 3.19(e) and 3.20(e), the simulation results can well reproduce the strain localization behavior observed in the experiment. Although homogeneous deformations can be seen until an axial strain of 4% is reached, the strain starts to localize at an axial strain of 8%, and then four or two shear bands appear at an axial strain of 12% and develop with an increased thickness on both surfaces. The generating process of the shear bands is well simulated in the both cases for normally consolidated clay and overconsolidated clay.

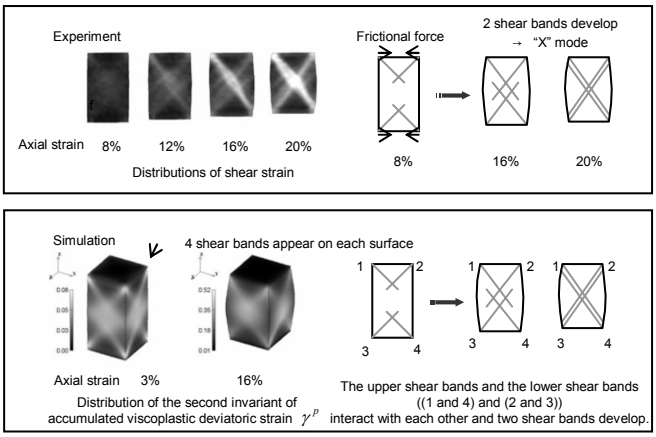

Figure 3.21. Schematics of the estimated process of the "X" mode for the experiment and simulation (OC-1, 1%/min).

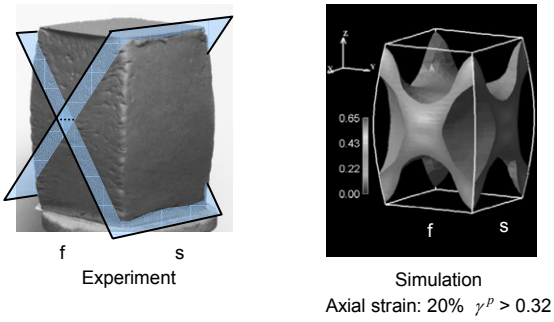

Figure 3.22. Estimated three-dimensional shear bands for experiment and simulation (NC-2, 0.1%/min).

Strain localization pattern

In the experiment and the simulation, we can see a deformation pattern in which two or four shear bands develop from the edges of the top and the bottom of the specimens. This mode is due to the material instability induced by the frictional boundary conditions between the clay specimens and the top caps and the pedestals. The two shear bands intercrossing each other are just like an "X", thus, we call it the "X" mode. Fig. 3.21 shows the schematics of the estimated process generating the "X" mode. The four shear bands generated finally develop two clear and thick shear bands. In the case of the finite element analysis, we depict the distribution of the second invariant of accumulated viscoplastic deviatoric strain γ^p for all cases. In the distributions, by disregarding smaller values of γ^p, we can see localized strain, i.e., three-dimensional shear bands. Note that γ^p is obtained at the Gaussian integration points of the finite element method and is different from the 'shear strain γ' used in the previous figures.

4) Three-dimensional shear bands

Estimated shear bands for case NC-2 (normally consolidated clay, 0.1%/min), tested and simulated, are depicted in Fig. 3.22**.** In the contour for the simulation results, the accumulation of the second invariant of viscoplastic deviatoric strain γ^p is illustrated if γ^p is more than 0.32. Since the shear bands observed on the front surface are clearer than those on the side surface, two shear planes are estimated. It is found, however, that the "X" mode appears just on the surface and that higher levels of shear strain are distributed in the center of the specimen.

5) Effects of the strain rates / Strain rate sensitivity

It is well known that clay exhibits strain rate sensitivity. Oka et al. (2003a) reported the strain rate sensitivity of Fukakusa clay under undrained triaxial compression conditions. As shown in Figs.3.19(a),(b) and 3.20(a),(b), rate sensitivity of the stress-strain relations and the stress paths in both cases of normally consolidated clay and overconsolidated caly can be observed. It can be seen that strain rate sensitivity observed in the experimental results is smaller than that in the simulation results.

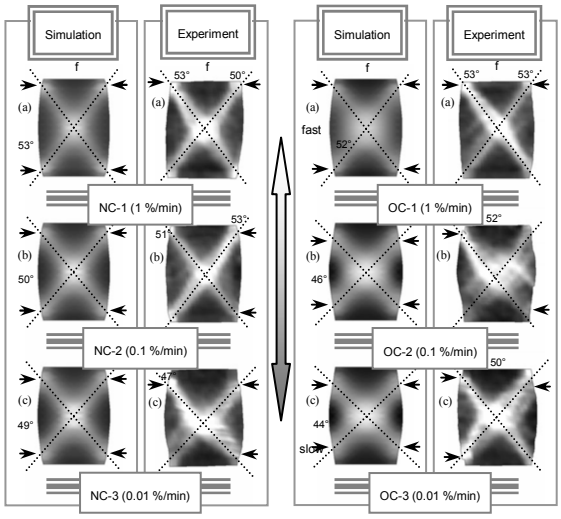

Figure 3.23. Comparison of distributions of shear strain and inclination angles of shear bands for specimen B with different strain rates between simulation result and experimental results (Axial strain: 20%, front surface); (a)shear bands develop from the top edge (b)(c)shear bands develop beneath the top edge.

Strain localization pattern

The shear-strain distributions and the inclination angles of the shear bands for both the simulation and the experiment with different strain rates at an axial strain of 20% are shown in Fig. 3.23**.** The numerical simulation very well reproduces the experimental results with respect not only to the "X" mode, but also to the effects of the strain rates on the strain localization pattern. Shear bands develop from the top and the bottom edges in the case of higher strain rates, while those with lower strain rates develop beneath the top and the bottom edges. Due to this tendency, the angles of the shear bands become smaller as the strain rate decreases. If we could assume that the effect of the strain rate is equal to the effect of permeability, i.e., the higher strain rates correspond to the lower permeability levels, and vice versa, we would then obtain a different trend from the one in the

present study, i.e., angles with higher strain rates are smaller than those with lower strain rates. Note that the constitutive equation used in Oka et al. (2002b) is slightly different from the one used in the present study. In addition, the maximum thickness of shear bands with lower strain rates is larger than that of shear bands with higher strain rates. It should be noted that these types of behavior are more clearly seen in the case of overconsolidated clay.

Effect of the sample shape

The effect of the sample shape has been studied by Kodaka et al. (2001) for normally consolidated clay. For the tall specimen with a high height over width ratio of H/B = 3.0, the bucking type of deformation mode is predominant for normally consolidated clay. On the contrary, for overconsolidated clay with H/B = 3.0, the X type of shear bands were experimentally observed and well simulated by the model (Kodaka et al., 2001; Oka et al., 2005c).

3.10 *Applications and recent advances*

3.10.1 *Bearing capacity and earth pressure problems*

A series of analyses on the footing of a clay deposit with different microstructure parameters was carried out (Siribumrungwong et al., 2004). The results of the analyses show that strain localization can be predicted during the loading of a footing on highly structured soil. This strain localization acts as a "slip line", and it affects the bearing behavior of the strip footing. The effects of footing roughness on the failure mechanism were also discussed.

For a smooth strip footing on clay soil with a constant level of undrained shear strength, both the Hill and the Prandtl failure mechanisms are theoretically possible. For a rough footing, however, the Hill mechanism is not appropriate as it implies horizontal soil movement at the soil-footing interface. It can be seen in Figs. 3.24 and 3.25 that the Hill mechanism (Hill, 1950) is predicted for a smooth footing and the Prandtl mechanism (1920) is predicted for a rough footing. Through a plasticity solution, both mechanisms yield the same value of Nc = 5.14. However, a comparison shows that with a large footing displacement, the reaction force predicted for the smooth footing is lower than that for the rough footing.Fig. 3.26 illustrates the behavior of backfill due to the movement of the wall analyzed by the same elasto-viscoplastic model for clay as that mentioned above. It is well simulated that the strain localization depends on the friction of the wall.

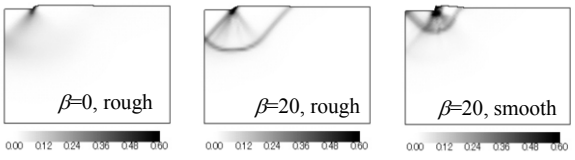

Figure 3.24. Distribution of viscoplastic deviatoric strain at a footing displacement of 10 cm for homogeneous soil case.

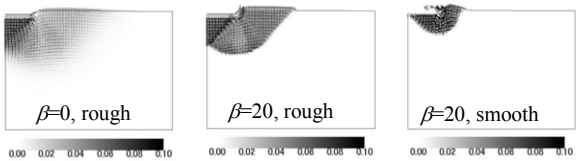

Figure 3.25. Vectors of incremental nodal displacements at a footing displacement of 10 cm for homogeneous soil cases.

3.10.2 *Thermo-hydro-mechanical-coupling problems*

Thermo-hydro-mechanical (THM) coupling problems are very important in the field of Geomechanics. THM has been applied to several problems such as nuclear waste disposal, ground heating, thermal consolidation, clean-up techniques for contaminated grounds and rapid landslides (e.g., Cleall, 2004; Vardoulakis, 2002). Vardoulakis (2002) studied the effect of thermal softening on catastrophic landslides. The temperature-dependent viscoplastic behavior was incorporated into the elasto-viscoplastic model by Yashima et al. (1998) based on the experimental results by Boudali et al. (1994). They showed that viscoplastic parameter m' in Eq. (2.26) is not dependent on the temperature, but viscoplastic parameter C in Eq. (2.27) is temperature dependent. The model was then incorporated into the finite element program and successfully applied to the thermal consolidation analysis using FEM with the energy balance law (Oka et al., 2005b). The other application of the temperature-dependent model is the analysis of the ground deformation due to the dissociation of a methane hydrate (Oka et al., 2005a).

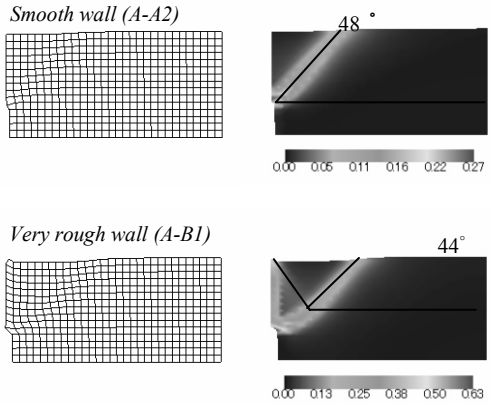

Figure 3.26. Comparison of deformed mesh and the accumulated viscoplastic shear strain from soil with different friction conditions between the soil and the wall in the case of active earth pressure.

3.10.3 *Slope stability*

Based on an elasto-plastic model with strain hardening and strain softening by Oka and Adachi (1985), Adachi et al. (2000) conducted a finite element analysis of a soil-water coupled problem to investigate the progressive failure of a cut slope in a model ground composed of soft rock. The mechanical behavior of the cut slope, such as changes in the excess pore-water pressure, the redistribution of the stress in the ground due to strain softening, the propagation of shear bands, and the progressive failure, were discussed in detail. It was found that a soil-water coupled analysis based on an elasto-plastic model with strain softening can simulate the progressive failure of a cut slope.

(1) Elasto-plastic model with strain softening

Oka (1985) proposed a new method to construct an elasto-viscoplastic model based on a generalized simple body in which a yield function depends on a stress history tensor. Oka's model (1985) can be continuously reduced to the inviscid model in limited cases. Oka and Adachi (1985), Adachi and Oka (1995) derived a strain-softening model for geologic materials based on a stress history tensor in which the stress history is defined by the generalized strain measure. The strain measure adopted in that model is similar to the endochronic concept advocated by Valanis (1971).

Adachi, Oka and Poorooshasb (1990) proposed a new type of viscoplasticity model for frozen sand by introducing a new time measure instead of real stress for frozen sand as

$$dz = g(\dot{\varepsilon}_{ij}^{*})dt, \qquad z = \int dz \tag{3.65}$$

where dz is an increment of the new time measure, dt is the real time increment, function g is a function that describes strain rate dependency to be determined experimentally for the particular medium, and $\dot{\varepsilon}_{ij}^{*}$ is a state parameter for the strain rate history. Under the three-dimensional conditions, Eq. (3.65) can be rewritten as

$$dz = g(F)^a dt \tag{3.66}$$

$$F = F(I_1, I_2)$$

where I_1 and I_2 are the first and the second invariants of the strain rate tensor, namely, $I_1 = \dot{\varepsilon}_{kk}$, $I_2 = \sqrt{\dot{e}_{ij}\dot{e}_{ij}}$, and a is the state parameter for the strain rate history.

When the function of g in Eq. (3.66) depends on the strain rate with a degree of one, dz becomes a rate-independent strain measure.

An elasto-plastic model with strain softening for soft rock introduces a strain measure and is expressed as

$$dz = (de_{ij} de_{ij})^{1/2} \tag{3.67}$$

where dz is an incremental strain measure and de_{ij} is an increment in the deviatoric strain component. Stress history tensor σ^*_{ij} is expressed by introducing a single exponential type of kernel function as

$$\sigma^*_{ij} = \sigma'_{ij}(0) + \frac{1}{\tau}\int_0^z \exp\left(-(z-z')/\tau\right)\left(\sigma'_{ij}(z') - \sigma'_{ij}(0)\right)dz \tag{3.68}$$

where τ is a material parameter expressing the retardation of stress with respect to the strain measure, σ'_{ij} is the stress tensor, and $\sigma'_{ij}(0)$ is the value of the stress tensor at $z = 0$. Total strain increment tensor $d\varepsilon_{ij}$ is composed of elastic $d\varepsilon^e_{ij}$ and plastic $d\varepsilon^p_{ij}$ components.

Plastic strain increment $d\varepsilon^p_{ij}$ is given by the non-associated flow rule as

$$d\varepsilon^p_{ij} = \Lambda\left(\partial f_p / \partial \sigma'_{ij}\right) df_y \tag{3.69}$$

where f_p is the plastic potential function, f_y is the yield function, and Λ is a positive function describing the strain hardening-softening characteristics. The subsequent yield function is defined by

$$f_y = \eta^* - \kappa = 0, \quad \eta^* = \sqrt{s^*_{ij} s^*_{ij}} / \sigma^*_m \tag{3.70}$$

where s^*_{ij} is the deviatoric stress history tensor and σ^*_m is the mean stress history. κ is the strain hardening-softening parameter and it is given by the following evolutional equation:

$$d\kappa = \frac{G'(M^*_f - \kappa)^2}{M^{*2}_f} d\gamma^p \quad \text{and} \quad d\gamma^p = (de^p_{ij} de^p_{ij})^{1/2} \tag{3.71}$$

where de^p_{ij} is an increment in the deviatoric plastic strain tensor. M^*_f is the value of stress history invariant ratio η^* at failure (residual strength state), and G' is the strain-hardening parameter (initial tangent of the curve defined by Eq. (3.71).

It is assumed that the relation expresses the plastic potential function

$$f_p = \bar{\eta} + \bar{M} \ln\left[(\sigma'_m + b)/(\sigma'_{mb} + b)\right] = 0 \tag{3.72}$$

and

$$\bar{\eta} = \left[s_{ij} s_{ij} / (\sigma'_m + b)^2\right]^{1/2} \tag{3.73}$$

where s_{ij} is the deviatoric stress tensor, σ'_m is the mean stress, and $\bar{M}$ is the parameter that controls the development of the volumetric strain.

The following relation expresses a boundary surface, which defines the normally consolidated and the overconsolidated regions:

$$f_b = \bar{\eta} + \bar{M}_m \ln\left[(\sigma'_m + b)/(\sigma'_{mb} + b)\right] = 0 \tag{3.74}$$

in which $\bar{M}_m$ is the value of $\bar{\eta}$ when maximum compression takes place during the shearing process.

Based on relation (3.74), the value of $\bar{M}$ in Eq. (3.72) can be determined based on the boundary surface, namely,

$$\bar{M} = -\bar{\eta} / \ln\left[(\sigma'_m + b)/(\sigma'_{mb} + b)\right] \qquad \text{if } f_b \le 0$$

$$\bar{M} = \bar{M}_m \qquad \text{if } f_b > 0 \tag{3.75}$$

$$\bar{\eta}_{ij} = s_{ij} / (\sigma'_m + b) \tag{3.76}$$

The elastic strain increment is given in a linear elastic form by

$$d\varepsilon^e_{ij} = \frac{ds_{ij}}{2G} + \frac{d\sigma'_m}{3K}\delta_{ij} \tag{3.77}$$

where G is the elastic shear modulus and K is the elastic bulk modulus.

There are eight parameters in the model, namely, G , K , b , σ'_{mb} , $\bar{M}_m$, M^*_f , G' , and τ . The parameters can be determined from the results of conventional triaxial compression tests, and Adachi and Oka (1995) have given detailed descriptions of the determination of these parameters.

(2) Finite element analysis of the progressive failure of cut slopes in an ideal model ground

For strain-softening material, when it is subjected to a shearing force, it will firstly exhibit strain hardening. After it reaches a peak value, strain softening will occur. It will finally reach the residual state if the shearing deformation continues.

In a boundary value problem such as an excavation, a stress concentration will occur which often results in a localized softening zone. Due to strain softening, the stress around the zone in this case will redistribute to satisfy the equilibrium equation. For this reason, the strain-softening zone will develop gradually due to the redistribution of stress. If the development of the zone stops, an overall failure of the slope will not occur. However, if the zone develops to such an extent that the surrounding ground cannot bear any more stress transferred from the softening zone, then an overall failure, called progressive failure, will occur. The material parameters of the ground used in the finite element analysis are as follows:

Young's modulus E (MPa) = 100.0, Poisson's ratio ν = 0.33, strain-softening parameter G' (MPa) = 45.2, residual stress ratio M^*_f = 1.0, plastic potential parameter b (MPa) = 0.87, plastic potential parameter σ'_{mb} (MPa) = 16.0, plastic potential parameter $\bar{M}_m$ = 1.25, material parameter τ = 0.025, density γ' (g/cm^3) = 1.0, and permeability k (cm/sec) = 10^{-6} .

Fig. 3.27 shows the finite element mesh adopted in the analysis of the cut slope in the water. The size of the considered section is 1000 m in length and 360 m in depth. The height and the slope gradient of the cut slope are 150 m and 5:1, respectively. The numbers of the nodes and the 4-node isoparametric elements are 1120 and 1053, respectively.

The boundary conditions are given as: (a) for displacement, it is fixed at the bottom in both x and y directions and it is fixed at the vertical boundaries in the x direction and (b) for excess pore-water pressure, the ground surface is the drainage boundary and the other boundaries are impermeable. The initial stress field is a gravitational field with $K_0 = 0.43$. In the calculation, the excavation of the slope is completed within about 35 days, and it is simulated by releasing the initial stress in 500 steps (0.2 % / step, 6000 sec/step). After the completion of the cut slope, a 30000-step calculation with a time interval of 6000 sec/step is conducted to simulate the dissipation of the excess pore-water pressure caused by the excavation of the slope.

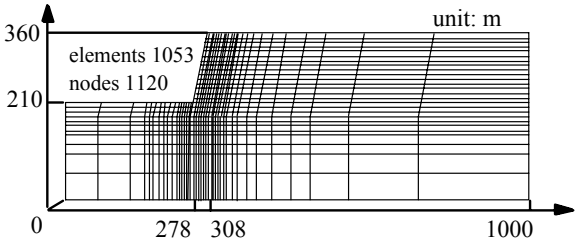

Figure 3.27. Finite element mesh of the cut slope.

In order to study the process of the progressive failure, the following two points are discussed, namely, overall changes in the field quantities such as the plastic strain, the excess pore-water pressure, and the stress state, and the time history of the stress history, the stress ratio, the strain rate, and the dilatation of the individual element.

Overall view of the changes in the field quantities of the progressive failure

Fig. 3.28 shows the changes in the distribution of the stress history ratio. In the residual state, the cohesion or the cementation of the geologic material tends toward zero and only the frictional strength that depends on confining stress remains.

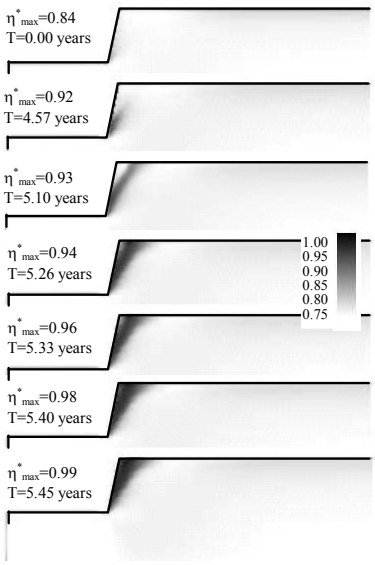

Figure 3.28. Distribution of the stress history ratio with time.

In this case, stress history ratio η^* will be the same as the stress ratio at the residual strength and takes the value of M_f^*. In the figure, $T = 0$ means the time immediately after the completion of the excavation. At the beginning, the value of η^* is kept constant at about 0.80. It increases abruptly 4.57 years after the completion of the excavation at the toe of the slope, and then the phenomenon propagates to other regions. A failure band forms six months later from the toe to the surface where η^* reaches the residual value. Finally, an unstable block appears with the shear band as a boundary connecting the stable area of the ground.

Fig. 3.29 shows the changes in the distribution of the plastic shear strain. Similar to the stress history ratio, the shear strain develops very quickly in the zone at the time of 4.57 years. The propagation of the shear zone in which large shear occurs, takes the same form as the failure zone shown in Fig. 3.28.

Fig. 3.30 shows the changes in the distribution of excess pore-water pressure with time. At the time immediately after the completion of the excavation, a large excess pore-water pressure develops in the ground, resulting in an apparent shear strength that keeps the slope stable. After 4.57 years, it dissipates gradually and the failure zone shown in Fig. 3.28 begins to develop due to the loss in the apparent shear strength. At this moment, the excess pore-water pressure reaches its minimum value. When the shear zone appears, strain softening occurs and dilatancy develops in some zone, resulting in an increase in excess pore-water pressure, as shown in Fig. 3.30.

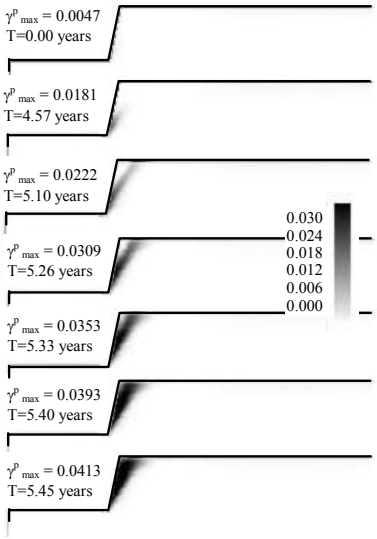

Figure 3.29. Changes in the plastic strain.

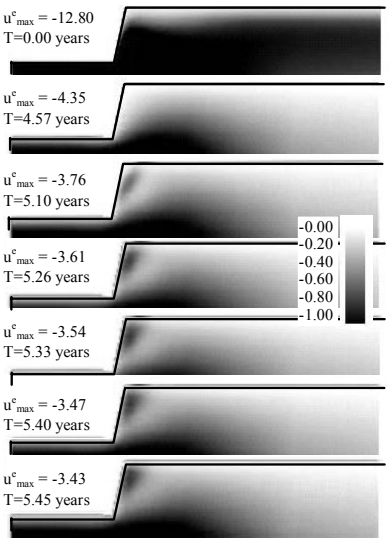

Figure 3.30. Changes in excessive pore-water pressure (× 98kPa).

From Figs. 3.28-3.30, it is clear that because of the dissipation of excess pore-water pressure due to the excavation, the ground of the cut slope loses its apparent strength and strain softening occurs in some areas. Then, a redistribution of stress leads to the start of propagation in the softening zone, resulting in the formation of a failure band and the shear zone. The failure band develops gradually and a global failure of the cut slope finally occurs. From the numerical analysis of the progressive failure of the cut slope, the following results were obtained:

(1) A cut slope in soft rock may remain stable for a long time after the completion of a rapid excavation. However, if a failure band appears abruptly in the slope, the slope may then collapse overwhelmingly after just a few months.
(2) The propagation of the shear zone in a cut slope takes the same form as the propagation of the failure zone.
(3) The progressive failure of a cut slope is caused by the redistribution of stress due to strain softening.

Before the global failure of a cut slope, an acceleration in the strain rate and an increase in negative excess pore-water pressure, that had dissipated a long time before, can be observed in a localized zone.

The progressive failure of a cut slope can be simulated with a soil-water coupled analysis based on an elasto-plastic model with strain softening.

3.11 *Summary*

From the perturbation approach of the viscoplastic instability, the followings have been found. In the hardening range, the growth rate of the perturbation is negative, namely, the material system is stable. In contrast, the material system may become unstable in the softening regime. It was confirmed that materials with higher permeability levels are more unstable than those with lower permeability levels. An instability analysis using a rigid-viscoplastic model gave the additional conclusion that the system is less stable in the hardening regime when the coefficient of permeability is rather small. In addition, the strain gradient term makes the system stable if gradient parameter a_3 is large enough. From the numerical study, it was found that in the range of small strain, i.e., in the viscoplastic strain-hardening range, the viscoplastic material system with low permeability levels is less stable. On the other hand, in the large strain, i.e., in the strain-softening range, the material system is less unstable. These trends are consistent with the theoretical results obtained from the instability analysis. As for the deformation pattern, permeability, namely, the transport of pore water, has a great influence on the formation of shear bands. When gradient term a_3 is large, the accumulated shear strain is less localized. It was confirmed that the gradient term acts as a stabilizer under globally undrained conditions. Material heterogeneity causes strain localization, although the deformation of homogeneous clay becomes uniform. The initial distribution of material parameters affects the deformation pattern.

From the simulation of three dimensional analysis of clay during compression, we have obtained the three-dimensional distributions of strain, stress, and pore-water pressure which are difficult to determine from experiments. Through the three-dimensional distributions, we have discussed the difference in strain localization behavior inside the specimens between normally consolidated clay and overconsolidated clay, e.g., the dilatancy characteristics and the local volume changes.

We confirmed that the simulation methods in this study can be very effectively applied to the strain localization behavior of clay under three-dimensional conditions. In the future, analyses of case studies which are related to strain localization, such as slope failure and excavations, will be necessary in order to practically verify the proposed method.

Finally, the viscoplastic analysis method have been successfully applied to the bearing capacity problem, earth pressure problem, thermo-hydro-mechanical coupling problem and cut slope stability problem. Then classical methods have been re-evaluated.

4 LIQUEFACTION ANALYSIS

Liquefaction is the typical failure mode of water-saturated sandy grounds. Soil liquefaction has been studied by many researchers, both theoretically and experimentally, since the earthquakes in Niigata and Alaska (1964). It has been recognized through in-situ research that civil structures were heavily damaged during such large earthquakes as the 1995 Hyogo-ken Nambu Earthquake due to the occurrence of liquefaction (Shibata et al., 1996).

There are two approaches for conducting a liquefaction analysis. One is a total stress analysis and the other is an effective stress analysis. Effective stress analyses include both coupled and uncoupled analyses. In a coupled analysis, the water flow is taken into account. At present, the fully coupled effective stress analysis is a representative method.

In this chapter, the computational modeling of the liquefaction of a sandy ground during an earthquake is demonstrated using the coupled stress analysis. The fully coupled method, which is based on the effective stress and is used for the dynamic analysis of a ground considering soil liquefaction, has been developed by many researchers. For the fully coupled effective stress analysis of the liquefaction of a ground, a cyclic plasticity model and governing equations are needed for the solid-fluid two-phase mixture. At present, a cyclic elasto-plastic model and a Biot type of mixture theory, the so-called theory of porous media, are used.

4.1 *Equations of motion and the mass balance of two-phase materials*

The following items can be assumed when formulating the governing equations for solid-fluid two-phase mixtures:

(1) When the relative acceleration of the fluid phase to that of the solid phase is much smaller than the acceleration of the solid phase, we can adopt a so-called u-p (displacement - pore pressure) formulation.
(2) When the relative acceleration of the fluid phase to that of the solid phase cannot be neglected, a u-w-p (displacement - relative displacement - pore-water pressure) formulation should be employed.
(3) Grain particles in the soil are incompressible.
(4) The distribution of porosity in the soil is sufficiently smooth.
(5) The densities of the soil skeleton and the pore water are spatially homogeneous.
(6) The body force is evenly distributed throughout the space.

In the theory of the two-phase mixture, the mixture is expressed by the superposition of two phases, namely, the solid phase and the fluid phase. The solid phase and the fluid phase represent the soil skeleton and the spatially distributed pore fluid, respectively.

The apparent densities of the solid and the fluid phases are given by the following relations:

$$\rho = \bar{\rho}^S + \bar{\rho}^F \qquad (4.1),\ \rho = (1-n)\rho^S + n\rho^F \qquad (4.2)$$

$$\bar{\rho}^S = (1-n)\rho^S \qquad (4.3),\ \bar{\rho}^F = n\rho^F \qquad (4.4)$$

where ρ is the density of the fluid saturated soil, ρ^S is the density of the soil particles, ρ^F is the density of the pore fluid, $\bar{\rho}^S$, $\bar{\rho}^F$ are the apparent densities of the solid and the fluid phases, respectively, and n is the porosity.

4.1.1 *Definition of partial stress tensor based on the two-phase mixture theory*

Cauchy's total stress is given by

$$\sigma_{ij} = \sigma_{ij}^S + \sigma_{ij}^F \qquad (4.5)$$

where σ_{ij}^S is the partial stress of the solid phase, σ_{ij}^F is the partial stress of the fluid phase, and δ_{ij} is Kronecker's delta. From the principle of effective stress by Terzaghi, Cauchy's effective stress tensor is given by

$$\sigma_{ij} = \sigma'_{ij} + p\delta_{ij} \qquad (4.6)$$

where p is the pore-water pressure and

$$\sigma_{ij}^F = np\delta_{ij} \qquad (4.7)$$

Hence, from Eqs. (4.5), (4.6), and (4.7),

$$\sigma_{ij}^S = \sigma'_{ij} + (1-n)p\delta_{ij} \qquad (4.8)$$

Equations of motion for the two-phase mixture

Equations of motion for the solid and the fluid phases are given by

$$\bar{\rho}^S \frac{\partial^2 u_i^S}{\partial t^2} = \frac{\partial \sigma_{ji}^S}{\partial x_j} - \frac{n^2 \gamma_w}{k} \frac{\partial \left(u_i^S - u_i^F \right)}{\partial t} + \bar{\rho}^S b_i \tag{4.9}$$

$$\bar{\rho}^F \frac{\partial^2 u_i^F}{\partial t^2} = \frac{\partial \sigma_{ji}^F}{\partial x_j} + \frac{n^2 \gamma_w}{k} \frac{\partial \left(u_i^S - u_i^F \right)}{\partial t} + \bar{\rho}^F b_i \tag{4.10}$$

where u_i^S is the displacement of the soil skeleton, u_i^F is the displacement of the pore fluid, b_i is the body force, k is the coefficient of permeability, and $\gamma_w = \rho^F g$ is the unit weight density of the pore fluid.

From Eqs. (4.9) and (4.10), we obtain

$$\bar{\rho}^S a_i^S + \bar{\rho}^F a_i^F = \frac{\partial \sigma_{ji}^S}{\partial x_j} + \frac{\partial \sigma_{ji}^F}{\partial x_j} + \left(\bar{\rho}^S + \bar{\rho}^F \right) b_i \tag{4.11}$$

Using Eqs. (4.1), (4.4), and (4.5), the above equation becomes

$$\rho a_i^S - n\rho^F \left(a_i^S - a_i^F \right) = \frac{\partial \sigma_{ji}}{\partial x_j} + \rho b_i \tag{4.12}$$

From assumption (1), where we can disregard $a_i^S - a_i^F$, we obtain equations of motion for the two-phase mixture as

$$\rho a_i^S = \frac{\partial \sigma_{ji}}{\partial x_j} + \rho b_i \tag{4.13}$$

4.1.2 *Continuity equation for the pore fluid*

The continuity equation is derived by the mass conservation laws and the equation of motion for the fluid phase. The mass conservation laws for the two phases are

$$\frac{\partial \bar{\rho}^S}{\partial t} + \frac{\partial \left(\bar{\rho}^S \dot{u}_i^S \right)}{\partial x_i} = 0 \tag{4.14}$$

$$\frac{\partial \bar{\rho}^F}{\partial t} + \frac{\partial \left(\bar{\rho}^F \dot{u}_i^F \right)}{\partial x_i} = 0 \tag{4.15}$$

After manipulation, we have

$$\frac{\partial \dot{w}_i}{\partial x_i} + D_{ii}^S + \frac{n}{\rho^F} \left(\frac{\partial \rho^F}{\partial t} + \dot{u}_i^F \frac{\partial \rho^F}{\partial x_i} \right) + \frac{1-n}{\rho^S} \left(\frac{\partial \rho^S}{\partial t} + \dot{u}_i^S \frac{\partial \rho^S}{\partial x_i} \right) = 0 \tag{4.16}$$

where

$$\frac{\partial \dot{u}_i^S}{\partial x_i} = D_{ii}^S \tag{4.17}$$

$$\dot{w}_i = n \left(\dot{u}_i^F - \dot{u}_i^S \right) \tag{4.18}$$

From assumption (3), $\dot{\rho}^S = 0$ and $\dot{\rho}^F = 0$ hold. From assumption (4), it then follows that $\partial n / \partial x_i = 0$. Moreover, $\partial \rho^S / \partial x_i = 0$ and $\partial \rho^F / \partial x_i = 0$ hold from assumption (5). From the above assumptions, Eq. (4.16) becomes

$$\frac{\partial \dot{w}_i}{\partial x_i} + D_{ii}^S = 0 \tag{4.19}$$

From Eq. (4.4), Eq. (4.10) becomes

$$\bar{\rho}^F a_i^F = \frac{\partial \sigma_{ij}^F}{\partial x_j} - \frac{n\gamma_w}{k} \dot{w}_i + \bar{\rho}^F b_i \tag{4.20}$$

Since

$$\frac{\partial \sigma_{ij}^F}{\partial x_j} = \frac{\partial (np)}{\partial x_i} \tag{4.21}$$

holds from Eq. (4.7), Eq. (4.20) can be written from Eqs. (4.4) and (4.21), assumptions (1) and (4), as

$$\rho^F a_i^S = \frac{\partial p}{\partial x_i} - \frac{\gamma_w}{k} \dot{w}_i + \rho^F b_i \tag{4.22}$$

By taking the derivative of Eq. (4.22) with respect to x_i,

$$\rho^F \frac{\partial a_i^S}{\partial x_i} = \frac{\partial^2 p}{\partial x_i^2} - \frac{\gamma_w}{k} \frac{\partial \dot{w}_i}{\partial x_i} + \rho^F \frac{\partial b_i}{\partial x_i} \tag{4.23}$$

From Eqs. (4.19) and (4.23), we have

$$\rho^F \frac{\partial a_i^S}{\partial x_i} = \frac{\partial^2 p}{\partial x_i^2} + \frac{\gamma_w}{k} D_{ii}^S + \rho^F \frac{\partial b_i}{\partial x_i} \tag{4.24}$$

From assumption (6), $\partial b_i / \partial x_i = 0$ holds. Hence, the above equation becomes

$$\rho^F \frac{\partial a_i^S}{\partial x_i} - \frac{\partial^2 p}{\partial x_i^2} - \frac{\gamma_w}{k} D_{ii}^S = 0 \tag{4.25}$$

4.2 *Formulation of the governing equations*

The above governing equations are then spatially discretized by numerical methods such as FEM and FDM, etc. Among the discretization methods, there are three methods, namely, the u-p formulation (Zienkiewicz et al., 1980; Oka 1994b; etc.), the u-U formulation (Prévost 1982; Zienkiewicz 1984), and the u-w-p formulation (Zienkiewicz, 1982; Lin, 2000; Oka, 2002), in which u is the displacement of the soil skeleton, U is the displacement of the pore water, p is the pore-water pressure, and w is the relative displacement between the displacements of the soil skeleton and the water which is defined by Eq. (4.18).

4.2.1 *u-U formulation*

In this formulation, the unknown variables are the displacements of the solid and the fluid phases. The corresponding pore pressure is determined by the constitutive equation for the pore fluid (Prévost 1982, 1985; Zienkiewicz and Shiomi 1984). However, the u-U formulation is not appropriate for cases with incompressible pore fluid. In addition, the degree of freedom becomes larger than with the u-p formulation. The displacement of U is replaced by relative displacement w. This formulation is used by Ghaboussi and Wilson (1972) and is called the u-w formulation.

4.2.2 *u-p formulation*

In this formulation, the unknown variables are the displacements of the soil skeleton and the pore-water pressure. The relative acceleration is small compared with the solid acceleration. This formulation is sufficient. The degree of freedom is comparatively small, and this is a great advantage for the numerical analysis. This u-p formulation has been used in many numerical codes (Zienkiewicz 1982; Zienkiewicz and Shiomi 1984; Simon et al. 1984; Aubry and Moderessi 1989; Oka et al. 1994b; etc.).

4.2.3 *u-w-p formulation*

The unknown variables of this formulation are u, w, and p. As has been studied by Zienkiewicz, Chang and Bettess (1980), a u-w-p formulation is necessary for high- frequency problems and problems with high permeability in which the relative acceleration cannot be disregarded. In the case of a dynamic analysis with high frequency, it is necessary to use a u-w-p formulation. In reality, a u-w-p formulation is recommended for soil composed of gravel and/or improved by a gravel drain. In addition, this u-w-p formulation is applicable for both compressible and incompressible pore fluids (Zienkiewicz, 1982; Lin 2000). The applicability of the u-w-p formulation is numerically evaluated in Fig. 4.1 (Oka 2002).

4.2.4 *Finite deformation theory*

The above formulation is done within the context of an infinitesimal strain theory. However, when we simulate a large deformation of the ground, the formulation has to be carried out using the finite deformation theory (Oka et al., 2001; Oka, 2002).

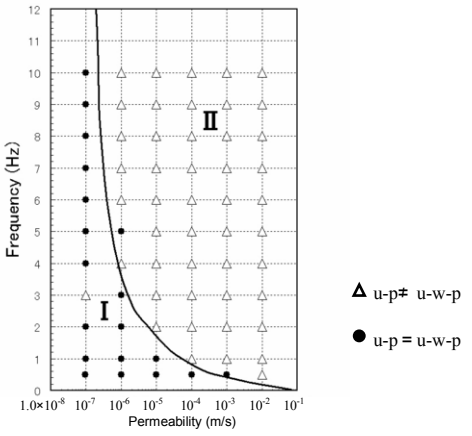

Figure 4.1. Evaluation of u-p and u-w-p methods.

4.3 *Constitutive equations*

4.3.1 *Introduction*

Over the last three decades, many elasto-plastic constitutive models have been proposed. The elasto-plastic theory is known as a representative tool for modeling the non-linear and the hysteretic behavior of soil. In the realm of soil mechanics, an associated flow rule has been used for modeling the behavior of soil, in particular, soil with negative dilatancy such as normally consolidated clay. In contrast, the non-associated flow rule is frequently adopted to model sand with positive-negative dilatancy. One of the well known models for soil is the Drucker-Prager model (1952). The Drucker-Prager model is a model that includes a dependency on the mean effective stress. However, there are several shortcomings with this model, namely, the unreasonable amount of dilatancy, etc. DiMaggio and Sandler (1971) proposed an elasto-plastic model for sand called the "Cap model" to generalize the Drucker-Prager model. The model contains two yield functions, i.e., a modified Drucker Prager model and a model that intersects the mean effective stress axis in the space of the second invariant of the deviatoric stress tensor and the mean effective stress. This model improved the behavior of the soil in the process with an increase in the mean effective stress. Although this Cap model is a simple model, it has been used for a variety of geological materials including rock. Nishi and Esashi (1978) and Vermeer (1978) then proposed a double hardening model based on the non-associated flow rule.

These models are consistent with the experimental results obtained by Poorooshasb et al. (1966). A number of constitutive models for sand have been proposed and then applied to design practices with appropriate numerical methods, such as the finite element method. In order to analyze the dynamic behavior of a liquefiable ground, it is necessary to predict the cyclic behavior of saturated sand.

For the cyclic behavior of sand, many models have been proposed, namely, Ghaboussi and Momen (1979); Oka and Washizu (1981); Pastor and Zienkiewicz (1986); Hashiguchi (1980, 1989); Nishi and Kanatani (1990); Ishihara and Kabilamany (1990); Prévost and Keane (1990); Oka et al. (1992a); Gajo and Muir Wood (1999); Oka et al. (1999a); Li, Dafalias and Wang (1999) have proposed cyclic elasto-plastic models for sand.

Many of them have tried to incorporate their models into computer programs for two-dimensional liquefaction analyses (e.g., Arulanandan et al., 2000). The present author proposed a constitutive model based on the rotational hardening rule (Adachi and Oka, 1982b; Oka, 1982) that can incorporate the Masing rule (Masing, 1926). This model was incorporated into a two-dimensional liquefaction analysis and some practical problems were solved by it (e.g. Oka et al., 1994b). Furthermore, the non-linear kinematic hardening rule originally proposed by Armstrong and Frederick (1966) for metal, and later modified by Chaboche and Rousselier (1983), was introduced (Oka et al., 1992a) into the rotational hardening model (Oka, 1982) for generalizing kinematic hardening. This non-linear kinematic hardening rule is described by an evolutional differential equation which is a generalized Prager's kinematic hardening rule and can take into account the initial anisotropy as well as the Bauschinger effect. The model (Oka et al., 1992a) is based on the non-linear kinematic hardening rule and has shown a better performance for describing the behavior of sand under cyclic loading than the model based on the concept of rotational hardening (Oka and Washizu, 1981, Akai et al., 1981). It has already been applied to several types of liquefaction problems.

The effectiveness of the cement mixing column method and the gravel drain method as countermeasures against liquefaction has been clarified by numerical work and by a two-dimensional liquefaction analysis (Shibata et al., 1992; Kato et al., 1994). The liquefaction of a seabed due to ocean waves (Oka et al., 1993c) and the seepage failure of loose sand layers (Oka et al., 1994a) were also studied with the original kinematic hardening model. The deformation of river embankment due to seepage was numerically analyzed in the context of liquefaction (Kato et al., 2005). Kodaka et al. (2005) developed a cyclic elasto-plastic model for the sand improved by colloidal silica.

In the model proposed by Oka et al. (1999a), a generalized flow rule was incorporated in order to accurately describe the cyclic behavior of sand and the liquefaction strength curve that relates the number of loading cycles to the shear stress amplitude.

The following two important factors have been incorporated into the constitutive model for sand to simulate the liquefaction process:

1) The mean effective stress decreases and becomes approximately zero during undrained cyclic loading with a constant shear stress amplitude for sand with low density. In some model simulations, however, the effective stress path often ends up describing a closed loop with a finite value for the mean effective stress that is much greater than zero even for sand with low density. This type of behavior is not always consistent with the test results for sand.
2) Predictions by some elasto-plastic constitutive models show that the slope of the liquefaction strength curve is quite a bit steeper than that obtained by the experiments.

4.3.2 *A constitutive model for sand with a generalized flow rule*

Oka et al. (1999a) developed an elasto-plastic constitutive model based on the non-linear kinematic hardening rule. Several modifications to the original kinematic hardening model (Oka et al., 1992a) are proposed based on a comparison between the experimental results and the numerical predictions by the model. The first feature of the model is the flow rule, the second one is the introduction of the cumulative plastic strain dependence of the plastic shear modulus, and the third one is the introduction of a fading memory of the initial anisotropy. The non-linear kinematic hardening variables are used in both the yield function and the plastic potential function.

Basic assumptions

The basic assumptions are taken as follows:

· infinitesimal strain theory
· elasto-plastic theory

· non-associated flow rule
· overconsolidated boundary surface
· non-linear kinematic hardening rule

Overconsolidation boundary surface
An overconsolidation boundary surface is adopted which distinguishes the overconsolidated region from the normally consolidated region. The overconsolidation boundary surface, $f_b = 0$, is defined as

$$f_b = \overline{\eta}^*_{(0)} + M^*_m ln\frac{\sigma'_m}{\sigma'_{mb}} = 0 \tag{4.26}$$

$$\overline{\eta}^*_{(0)} = \left\{\left(\eta^*_{ij} - \eta^*_{ij(0)}\right)\left(\eta^*_{ij} - \eta^*_{ij(0)}\right)\right\}^{1/2} \tag{4.27}$$

$$\eta^*_{ij} = s_{ij}/\sigma'_m \tag{4.28}$$

where σ'_m is the mean effective stress, s_{ij} is the deviatoric stress tensor, M^*_m is the value of the stress ratio expressed by $\sqrt{\eta^*_{ij}\eta^*_{ij}}$ when the maximum volumetric strain during shearing takes place and which could be called the phase transformation stress ratio, and $\eta^*_{ij(0)}$ denotes the value of η^*_{ij} at the end of the consolidation.

The condition $f_b < 0$ means that the stress state stays in the overconsolidated region (O.C. region), while $f_b \geq 0$ means that the stress state stays in the normally consolidated region (N.C. region). Herein, σ'_{mb} in Eq. (4.26) is given as follows:

$$\sigma'_{mb} = \sigma'_{mbi}\exp\left(\frac{1+e}{\lambda-\kappa}v^P\right) \tag{4.29}$$

where σ'_{mbi} is the initial value of σ'_{mb}, κ is the swelling index, λ is the compression index, e is the void ratio, and v^P is the plastic volumetric strain.

σ'_{mbi} is determined by considering the volume change characteristics of sand, although it is usually thought that for isotropically consolidated soils, σ'_{mbi} is equal to the preconsolidation pressure in the context of the conventional concept of overconsolidation. The σ'_{mbi} of sand samples is not always equal to σ'_{m0} (the mean effective stress at the end of the consolidation) due to the material anisotropy, the method of the sample preparation, the degree of compaction, aging, etc. $OCR^* = \sigma'_{mbi}/\sigma'_{m0}$ should be called the quasi-overconsolidation ratio (quasi-O.C.R.). Furthermore, σ'_{mc}, which is the mean effective stress at the intersection of the overconsolidated boundary surface and the σ'_m axis, is defined as

$$\sigma'_{mc} = \sigma'_{mb}\exp\left(\frac{\eta^*_{(0)}}{M^*_m}\right) \tag{4.30}$$

The overconsolidated boundary surface, i.e., the surface for isotropically consolidated sand in the $\sqrt{2J_2}$ – σ'_m plane, is shown in Fig. 4.2. J_2 is the second invariant of deviatoric stress tensor s_{ij}, i.e., $J_2 = \frac{1}{2}s_{ij}s_{ij}$.

Fading memory of the initial anisotropy
During cyclic loading in soils, the effect of the initial anisotropy decreases. In the original model, the overconsolidation boundary surface depends on the initial anisotropy of the soils, as shown in Eq. (4.30), so that the existence of the initial anisotropy influences the shape of the overconsolidation boundary surface. Herein, the initial anisotropy is assumed to fade during cyclic loading in soils. To take this into account, the following coefficient, $\zeta = \zeta(\gamma^{P*})$, is used in Eq. (4.30):

$$\sigma'_{mc} = \sigma'_{mb}\exp\left(\zeta\frac{\eta^*_{(0)}}{M^*_m}\right) \tag{4.31}$$

$$\zeta = -C_d\gamma^{P*} = -C_d\int d\gamma^{P*} \tag{4.32}$$

$$d\gamma^{P*} = \left(de^P_{ij}de^P_{ij}\right)^{1/2} \tag{4.33}$$

in which, γ^{P*} is the cumulative plastic shear strain from the initial condition, de^P_{ij} is the plastic deviatoric strain increment tensor, and C_d is a constant which controls the rate of disappearance of anisotropy. When sand is initially in an isotropic state, Eq. (4.31) is equivalent to Eq. (4.30) because the value of $\eta^*_{(0)}$ is zero.

Yield Function
The yield function for changes in the stress ratio, f_{y1}, is denoted as

$$f_{y1} = \left\{\left(\eta^*_{ij} - \chi^*_{ij}\right)\left(\eta^*_{ij} - \chi^*_{ij}\right)\right\}^{1/2} - k = 0 \tag{4.34}$$

where k is a numerical parameter which controls the size of the elastic region and χ^*_{ij} is the non-linear kinematic hardening parameter. χ^*_{ij} has the same dimensions as stress ratio η^*_{ij} and is the so-called back stress parameter. The evolution equation for the hardening parameter is defined by Eq. (4.35), namely,

$$d\chi^*_{ij} = B^*\left(A^*de^P_{ij} - \chi^*_{ij}d\gamma^{P*}\right) \tag{4.35}$$

in which A^* and B^* are material parameters. A^* and B^* are related to the stress ratio at failure, M^*_f, and the initial plastic shear modulus normalized with the mean effective stress, G^P, respectively, as follows:

$$A^* = M^*_f, \quad B^* = \frac{G^P}{M^*_f} \tag{4.36}$$

In general, parameter B^* can be considered to follow the evolution equation as

$$dB^* = C_f(B^*_1 - B^*)d\gamma^{P*} \tag{4.37}$$

in which C_f and B^*_1 are material parameters. $\chi^*_{ij}d\gamma^{P*}$ in Eq. (4.35) is the non-linear term that depends on the magnitude of the increment of plastic shear strain. If $\chi^*_{ij}d\gamma^{P*}$ is negligible, Eq. (4.35) will lead to the well known Prager's linear kinematical hardening rule given by $d\chi^*_{ij} = B^*A^*de^P_{ij} = G^Pde^P_{ij}$.

After the stress state earnest cyclic mobility, the rate of decrease in G^P due to the accumulation of plastic strain is accelerated. Therefore, a decrease in G^P with an increase in $\gamma^{P*}_{(n)}$ is introduced as

$$G^P = (G^P_{\max} - G^P_{\min})\exp(-C_f\gamma^{P*}_{(n)}) + G^P_{\min} \tag{4.38}$$

$$\gamma^{P*}_{(n)} = \int_{(n)} d\gamma^{P*} \tag{4.39}$$

where $G^P_{\max}$ is the initial value of G^P, $G^P_{\min}$ is the lower limit of G^P, and C_f is a constant. Using Eq. (4.38), three parameters, $G^P_{\max}$, $G^P_{\min}$, and C_f, can be identified at each cycle. $\gamma^{P*}_{(n)}$ is the accumulated plastic shear strain between two sequential stress reversal patois at the previous cycle. Cycle n can be easily indebted. In reality, a half cycle is defined as the process between two sequential stress reversal patois. The stress reversal point is judged by the changes in the sign of df_{y1}, the increment of f_{y1} in Eq. (4.34), in the general stress condition. This automatic identification of a cycle is one advantage of using the non-linear kinematic hardening rule. G^P decreases with an increase in $\gamma^{P*}_{(n)}$ (Oka et al., 1999). Herein, the onset of the cyclic mobility condition is judged when stress ratio η^* reaches M^*_m. During cyclic mobility, the value of $G^P_{\max}$ decreases with an increase in $\gamma^{P*}_{(n)\max}$. Hara et al. (1984) also reported the same tendency with

the relationship between $G^P_{\max}$ and $\gamma^{P*}_{(n)\max}$. The remaining parameters, $G^P_{\min}$ and C_f, are also generally found to be dependent on $\gamma^{P*}_{(n)\max}$. In the modeling, however, only $G^P_{\max}$ is assumed to be dependent on $\gamma^{P*}_{(n)\max}$. The two remaining parameters are assumed not to be dependent on $\gamma^{P*}_{(n)\max}$, because $G^P_{\max}$ was found to have a stronger effect on the changes in G^P than the other two parameters. The relationship between $G^P_{\max}$ and $\gamma^{P*}_{(n)\max}$ is assumed as follows:

$$G^P_{\max} = \frac{G^P_{\max 0}}{1+\gamma^{P*}_{(n)\max}/\gamma^{P*}_{(n)r}} \tag{4.40}$$

where $G^P_{\max 0}$ is the initial value of $G^P_{\max}$ and $\gamma^{P*}_{(n)r}$ is the reference value of $\gamma^P_{(n)\max}$ when the value of $G^P_{\max}$ is half the value of $G^P_{\max 0}$. The lower limit of $G^P_{\max}$ is $G^P_{\min}$. The same type of equation is also applied for modeling the reduction in the elastic shear modulus in which $\gamma^{E*}_{(n)r}$ is used as a reference value instead of $\gamma^{P*}_{(n)r}$.

$$G^E = \frac{G^E_0}{1+\gamma^{E*}_{(n)\max}/\gamma^{E*}_{(n)r}} \tag{4.41}$$

where $\gamma^{E*}_{(n)\max}$ is the maximum accumulated elastic shear between sequential stress reversal points at past cycles. G^E_0 is the initial value of G^E, namely, the elastic shear modulus normalized with the mean effective stress.

Changes in yield function f_{y1} in Eq. (4.34) are governed by changes in the stress ratio. As for the analysis under general stress conditions, the second yield function, f_{y2}, which is described based on changes in the mean effective stress, should be taken into account (Oka, 1992).

Plastic strain dependence of the shear modulus

Thus far, three methods have been proposed by which the plastic strain dependence of the plastic shear modulus is described as follows:

1) Method I
   Oka (1993d) proposed a plastic strain dependency of B^* as

$$B^* = (B^*_0 - B^*_1)\exp(-C_f\gamma^{P*}_0) + B^*_1 \tag{4.42}$$

   in which B^*_1 is the lower bound of B^* and γ^{P*}_0 is the accumulated value of the second invariant of the deviatoric plastic strain from the initial state. In Method I, the elastic modulus is assumed not to be dependent on the plastic strain.
2) Method II
   Oka et al. (1999a) proposed the method using Eqs. (4.38), (4.40), and (4.41). Method II is the most general and the most complicated method among the three methods. In Method II, $B^* = G^P/M^*_f$ is updated with the accumulated plastic shear strain between two sequential stress reversal patois at the previous n-th cycle when the stress reverses. Eq. (4.38) can be rewritten with B as

$$B^* = G^P/M^*_f = (B^*_{\max} - B^*_1)\exp(-C_f\gamma^{P*}_{(n)}) + B^*_1 \tag{4.43}$$

   Moreover, $B^*_{\max}$ is reduced with the maximum accumulated plastic shear strain between sequential stress reversal points in the previous n-th cycle after stress ratio η^* has reached M^*_m. Eq. (4.40) can be rewritten with B^*_0 as

$$B^*_{\max} = G^P_{\max}/M^*_f = \frac{B^*_0}{1+\gamma^{P*}_{(n)\max}/\gamma^{P*}_{(n)r}} \tag{4.44}$$

   The elastic modulus is also reduced by using Eq. (4.41) in a similar manner to the plastic modulus.
3) Method III
   B^* is determined by the following equation only when the stress ratio has reached the phase transformation line as

$$B^* = \frac{B^*_0}{1+\gamma^{P*}_{ap}/\gamma^{P*}_r} \tag{4.45}$$

   in which γ^{p*}_{ap} is the accumulated value of the second invariant of the deviatoric plastic strain tensor after it has reached the phase transformation line and γ^{P*}_r is the reference strain. The lower limit of B^* is given by B^*_1. As for elastic shear modulus G^E, a similar relation is adopted for updating it in Method III.
4) Method IV (Oka et al., 2004a)
   In this method, Eq. (4.43) is used for the determination of B^*, but $B^*_{\max}$ is given by Eq. (4.45) as

$$B^*_{\max} = \frac{B^*_0}{1+\gamma^{P*}_{ap}/\gamma^{P*}_r} \tag{4.46}$$

In general, the second method has a high potential to reproduce the cyclic behavior of various types of soil. However, the method needs the special data to identify the parameters. It is not always easy for engineers to determine many parameters. In contrast, when we adopt the first or the third methods, the soil parameters can be determined more simply. It was found that the third method, Eq. (4.45), is effective for modeling the plastic strain dependence of the plastic shear modulus and the elastic shear modulus. From the numerical studies mentioned later, Method IV has been found to be effective for the simulation of loose sand, medium dense sand, and dense sand.

Changes in the yield function, f_{y1} in Eq. (4.34), are governed by changes in the stress ratio.

As for the analysis under general stress conditions, the second yield function, f_{y2}, which is defined on the basis of changes in the mean effective stress, should be taken into account (Oka 1992):

$$f_{y2} = M^*_m\left|\ln\left(\frac{\sigma'_m}{\sigma'_{m0}}\right) - y^*_m\right| - R_d = 0 \tag{4.47}$$

where y^*_m is the scalar kinematic hardening parameter, σ'_{m0} is the unit value of the mean effective stress, and R_d is the scalar variable. Since the strain levels brought about by changes in the mean effective stress are small in the overconsolidated region, it can be assumed that the second static yield function can be disregarded in the overconsolidated region.

Kinematic hardening parameter y_m is decomposed into y^*_{m1} and y^*_{m2}. The evolutional equations for these kinematic hardening parameters are given by

$$dy^*_m = dy^*_{m1} + dy^*_{m2} \tag{4.48}$$

$$dy^*_{m1} = B^*_2(A^*_2 dv^p - y^*_{m1}|dv^p|) \tag{4.49}$$

$$dy^*_{m2} = H^*_2 dv^p \tag{4.50}$$

Plastic potential function

The non-linear kinematic hardening variable is used in the plastic potential function as well as in the yield function. Plastic potential function g is denoted as follows:

$$g = \left\{\left(\eta^*_{ij} - \chi^*_{ij}\right)\left(\eta^*_{ij} - \chi^*_{ij}\right)\right\}^{1/2} + \tilde{M}^*\ln\left(\frac{\sigma'_m}{\sigma'_{ma}}\right) = 0 \tag{4.51}$$

where σ'_{ma} is a constant and $\tilde{M}^*$ is defined by

$$\tilde{M}^* = \begin{cases} -\dfrac{\eta^*}{\ln(\sigma'_m/\sigma'_{mc})} & \text{(O.C. region in which } f_b < 0) \\ M_m^* & \text{(N.C. region in which } f_b \geq 0) \end{cases} \tag{4.52}$$

M_m^* is the stress ratio when a maximum contraction of the material takes place. $\tilde{M}^*$, which is a variable depending on the stress state, controls the direction of the plastic strain increment. When the stress state is inside the overconsolidated region, $\tilde{M}^*$ takes a value that is less than that of M_m^*. In addition, it is assumed that $\tilde{M}^*$ becomes equal to M_m^* once $\tilde{M}^*$ has reached M_m^*. The plastic potential function and the overconsolidated boundary surface are shown in Fig. 4.2.

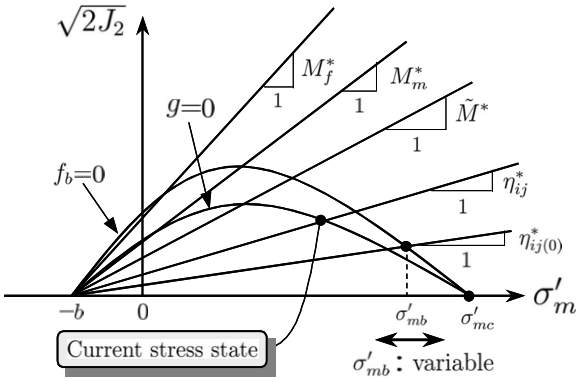

Figure 4.2. Plastic potential and O.C. boundary surfaces.

The stress-dilatancy characteristic which is normally derived from the conventional flow rule sometimes gives a rather steeper slope to the liquefaction strength curve than that obtained from laboratory tests. In order to counteract this shortcoming in the original model, the flow rule is generalized using the fourth rank isotropic tensor, H_{ijkl} (Naghdi and Trapp, 1975), as

$$d\varepsilon_{ij}^P = H_{ijkl}\frac{\partial g}{\partial \sigma'_{kl}} \tag{4.53}$$

$$H_{ijkl} = a\delta_{ij}\delta_{kl} + b(\delta_{ik}\delta_{jl} + \delta_{il}\delta_{jk}) \tag{4.54}$$

namely,

$$de_{ij}^P = 2b\frac{\partial g}{\partial s_{ij}}, \quad d\varepsilon_{kk}^P = (3a+2b)\frac{\partial g}{\partial \sigma'_m} \tag{4.55}$$

Desai and Siriwardane (1980) adopted a similar approach to the general description of $d\varepsilon_{ij}^P$ by introducing the correction factor into the flow rule. Coefficients a and b in Eq. (4.54) generally depend on the state parameters, e.g., stress and strain. From Eqs. (4.51), (4.53), and (4.54), a stress-dilatancy characteristic relation of the generalized model can be derived by the generalized flow rule, Eq. (4.53) as follows:

$$\frac{dv^P}{d\gamma^{P*}} = D^*(\tilde{M}^* - \eta_x^*) \tag{4.56}$$

where

$$D^* = \frac{3a}{2b} + 1 \tag{4.57}$$

D^* is a so-called coefficient of dilatancy which controls the proportion of the plastic deviatoric strain increment to the plastic volumetric strain increment. As for the functional form of D^*, two types of functions are used in this study. The first one is as follows:

$$D^* = D_0^* = const. \tag{4.58}$$

A constant coefficient of dilatancy has often been used, e.g., by Pradhan and Tatsuoka (1989). In the model, D^* is the nonlinear function as

$$D^* = D_0^*\left(\frac{\eta^*}{\eta_r^*}\right)^n = D_0^*\left(\frac{\eta^*}{M_m^* ln(\sigma'_{mc}/\sigma'_m)}\right)^n = D_0^*\left(\frac{\tilde{M}^*}{M_m^*}\right)^n \tag{4.59}$$

where η_r^* is the value of the stress ratio on the overconsolidation boundary surface with a current mean effective stress. When η^* is larger than η_r^*, η^* is kept to the value of η_r^*. In a case where the stress state is inside the overconsolidated region, Eq. (4.59) is the n-th power of the stress ratio invariant. When the value of n is larger than one and the stress conditions are inside the overconsolidated region, the value of the coefficient of dilatancy changes drastically due to changes in the stress ratio.

Stress-strain relation

The total strain increment tensor, $d\varepsilon_{kl}$, is given by adding the elastic strain increment tensor, $d\varepsilon_{kl}^E$, and the plastic strain increment tensor, $d\varepsilon_{kl}^P$, as

$$d\varepsilon_{kl} = d\varepsilon_{kl}^E + d\varepsilon_{kl}^P \tag{4.60}$$

The plastic part of the deviatoric strain increment is derived from Eq. (4.55) and the consistency condition, $df = 0$. The elastic part of the deviatoric strain increment is given as

$$de_{ij}^E = \frac{1}{2(G^E\sigma'_m)}ds_{ij} \tag{4.61}$$

where G^E is the elastic shear modulus normalized to the mean effective stress, namely, σ'_m. The elastic volumetric strain increment is also obtained with swelling index κ and void ratio e as

$$d\varepsilon_{kk}^E = \frac{\kappa}{1+e}\frac{d\sigma'_m}{\sigma'_m} \tag{4.62}$$

4.4 *Performance of the proposed model*

Theoretical simulation of Toyoura sand

A theoretical simulation of the behavior of Toyoura sand under undrained cyclic shear tests was conducted with torsional hollow cylinder test apparatus (Earthquake Engineering Committee JSCE (2003); Oka, Furuya and Uzuoka, 2004c). The specimen was consolidated under an isotropic pressure of 98kPa. The minimum void ratio was 0.605 and the maximum void ratio was 0.977. Figs. 4.3 – 4.6 show the theoretical and the experimental results.

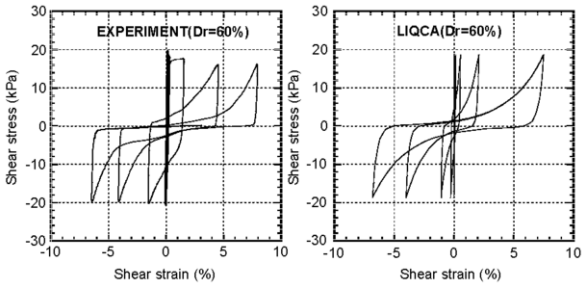

(a) Experiment (b) Theoretical simulation

Figure 4.3. Stress-strain relations (Dr = 60%).

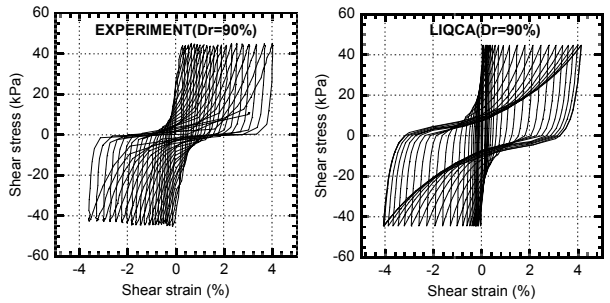

(a) Experiment (b) Theoretical simulation

Figure 4.4. Stress-strain relations (Dr = 90%).

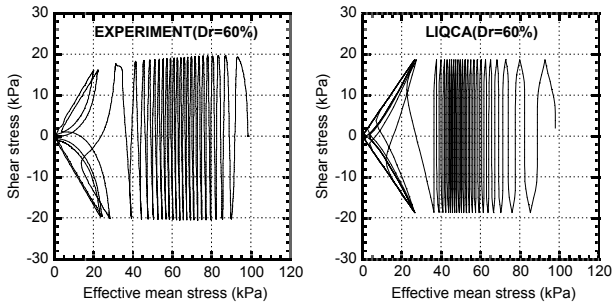

(a) Experiment (b) Theoretical simulation

Figure 4.5. Stress paths (Dr = 60%).

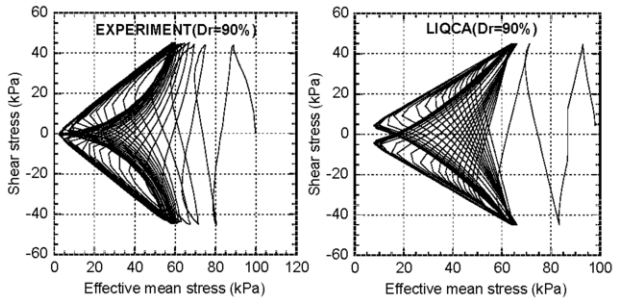

(a) Experiment (b) Theoretical simulation

Figure 4.6. Stress paths (*Dr* = 90%).

From Figs. 4.3 – 4.4, it is seen that the proposed model can successfully simulate the stress-strain relation of medium sand and dense sand (*Dr* = 60 - 90%). Figs. 4.5 – 4.6 indicate the corresponding stress paths. The simulated results are similar to the experimental results. From these numerical results, it can be concluded that the proposed model can well predict the behavior of sand for a wide range of relative densities.

4.5 *Numerical applications*

Oka et al. (1994b) proposed a numerical method based on a u-p formulation with the finite element method and the finite difference method in the infinitesimal strain field. The equation of motion is discretized by FEM and the continuity equation is discretized by the finite difference method (Oka et al., 1994b). As for the time discretization in the time domain, Newmark's β method is used. In addition, Rayleigh's damping is used in the analysis which is proportional to the initial stiffness matrix and the mass matrix. The numerical procedure is implemented in the computer program: LIQCA2D (two-dimensional, Oka et al., 2005) and LIQCA3D (three-dimensional) for the infinitesimal strain field and LIQCAFD for the finite deformation theory (Oka et al., 2001; Oka, 2002). In these programs, a cyclic elasto-plastic model for sand (Oka et al. 1999a), its modified model, and an elasto-viscoplastic model for clay (Oka and Yashima, 1995) are used. In this section, as a numerical example of a three-dimensional liquefaction analysis, a site response analysis on Port Island in Kobe City, Japan during the 1995 Hyogo-ken Nambu Earthquake is presented (Oka, Uzuoka, Tateishi and Yashima, 2003b).

Vertical array records at Port island

Strong borehole motion vertical array observations on Port Island have been conducted by the Development Bureau of Kobe City. Three components of the accelerations which consisted of N-S, E-W, and U-D directions have been recorded at four levels for depths of GL-83 m, GL-32 m, GL-16 m, and GL-0 m, as shown in Fig. 4.7. The depth of GL-83 m corresponds to the base layer which is on top of the diluvial dense sand, namely, Ds. The depth of GL-32 m is on the bottom of the alluvial medium dense sand, namely, As. The depth of GL-16 m is on the bottom of the reclaimed gravelly sand, namely, B3.

The acceleration histories of the main shock during the 1995 Hyogo-ken Nambu Earthquake on January 17 were obtained. The epicenter was the northern edge of Awaji Island and JMA's magnitude was 7.2 (modified; 7.3, 2001). The obtained acceleration histories will be shown later with the simulated results.

Numerical data for the analysis

The computer code "LIQCA-3D" was used in the analysis. This program was developed based on the above-mentioned cyclic elasto-plasticity model for sand and a cyclic elasto-viscoplasticity model developed by Oka and Yashima (1995). The cyclic elasto-plasticity model for sand was applied to layers B1, B2, B3, and As, as shown in Fig. 4.7. In this simulation, we used Method III for the shear modulus reduction depending on plastic shear strain history. The cyclic elasto-viscoplasticity model for clay was applied to the Ac layer in Fig. 4.7. To model the stiff sandy ground and sandy gravel, a generalized Ramberg-Osgood model was used in which the second invariant of the deviatoric stress tensor is incorporated. The Ramberg-Osgood model was applied to the Ds/c, Dc, and Ds layers in Fig. 4.7. In Table 4.1, the material parameters used in the analysis are listed. These parameters are determined by the existing field and the laboratory testing data.

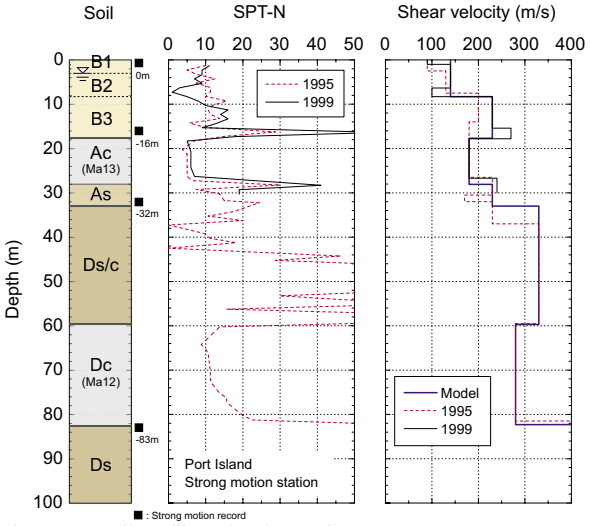

Figure 4.7. Soil profile at the observation.

Basic ground parameters

The soil profile and the ground water table were determined from Fig. 4.7, which was obtained through boring at the observation site. The density and the void ratio were determined from the density measurement of an undisturbed sample obtained after the earthquake.

The coefficient of permeability was determined from laboratory permeability tests on the undisturbed sample obtained after the earthquake. The shear velocity was estimated from the PS logging tests at the observation site in 1995 and 1999.

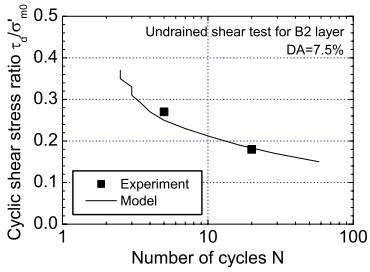

Figure 4.8. Liquefaction strength for reclaimed soil.

Parameters for the elasto-plasticity model

It is important to estimate an appropriate shear modulus in an earthquake response analysis. The actual shear modulus of the elasto-plastic model is given as elasto-plastic shear modulus G^{EP} in the analysis.

The failure stress ratio was determined from the undrained triaxial tests using the undisturbed sample. The phase transformation stress ratio was determined from past laboratory tests by Pradhan et al. (1989a, 1989b).

The remaining parameters were determined by the data adjusting method for the undrained cyclic shear tests. In these tests, the values of the material parameters were selected in order to provide a good description of the stress-strain relations under cyclic loading conditions and liquefaction strength curves. The undrained cyclic shear tests for the reclaimed soil were conducted with an in-situ frozen sample by Suzuki et al. (1997). The experimental and the simulated liquefaction strength levels, which were cyclic shear stress levels producing a double amplitude strain of 7.5% with a particular number of cycles, are shown in Fig. 4.8. The simulated liquefaction strength for the reclaimed B2 layer agrees well with the experimental one.

Parameters for the elasto-viscoplasticity model

All the remaining parameters were determined in the undrained triaxial tests using the clay samples obtained at the observation site. In particular, the viscoplastic parameters were determined from the monotonic shear tests with two different loading rates. We confirmed the applicability of the determined parameters through a simulation for the dynamic strength obtained by the cyclic shear tests.

Parameters for the ramberg-osgood model

The remaining parameters were determined from the strain-dependent shear modulus and the damping ratio, which were obtained by the undrained cyclic shear tests with multi-step loading. The Ds/c, Dc, and Ds layers modeled by the Ramberg-Osgood model (Oka et al., 2004a) had no dilatancy, therefore, these layers generated no buildup of excess pore-water pressure.

FE model and the numerical parameters

A single column ground model composed of three-dimensional solid finite elements was used for the analysis. The number of finite elements was 31 with 128 nodes. The model displacements were fixed at the base. Four nodes at the same depth were assumed to move coincidentally. The lateral and the bottom boundaries were assumed to be impermeable, while the ground water surface was assumed to be permeable. As an input earthquake motion at the base rock, the three components (NS, EW, and UD) of the acceleration records obtained at a depth of -83 m of the vertical array recording site on Port Island were used.

Rayleigh damping, proportional to the initial stiffness, which was determined by assuming that the damping factor is 1%, was used as the convenient method in this study. A time integration step of 0.002 seconds was adopted to obtain sufficient accuracy. β and γ in Newmark's β-method were set to be 0.3025 and 0.6, respectively, to ensure numerical stability.

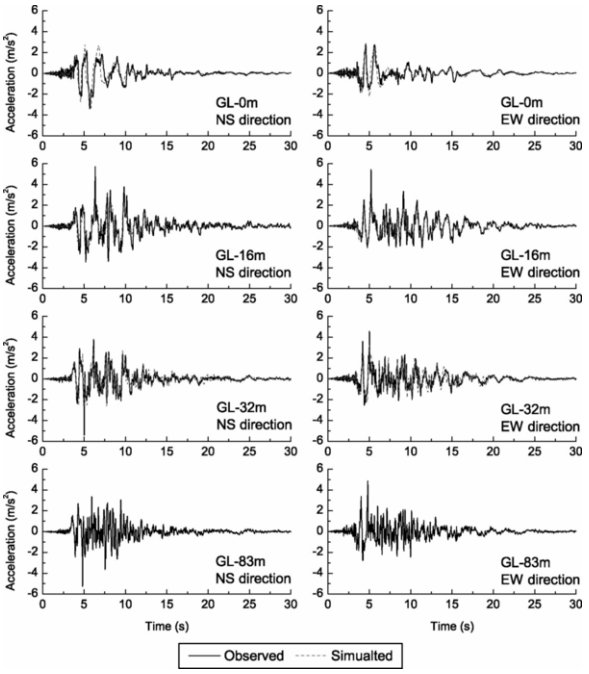

Figure 4.9. Time histories of observed and simulated horizontal acceleration.

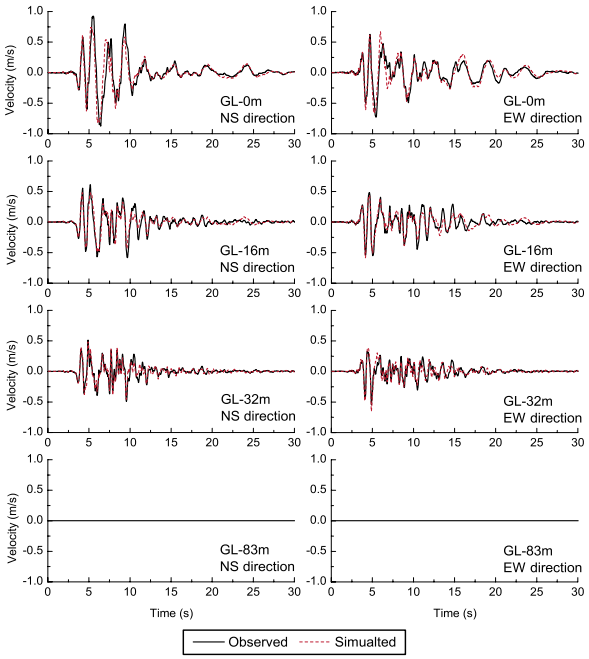

Figure 4.10. Time histories of the observed and the simulated relative horizontal velocities.

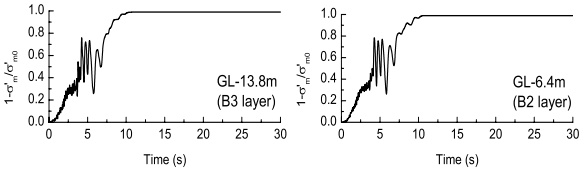

Figure 4.11. Time histories of the simulated effective stress reduction ratio.

Table 4.1: Material parameters for the numerical analysis

Name of soil profile	B1	B2	B3
Soil type	Gravelly sand	Gravelly sand	Gravelly sand
Model type	E-P	E-P	E-P
Density ρ (t/m^3)	1.90	2.10	2.10
Initial void ratio e_0	0.42	0.42	0.42
Coefficient of permeability k (cm/s)	-	0.003	0.003
Compression index λ	0.01	0.01	0.01
Swelling index κ	0.001	0.001	0.001
Poisson's ratio υ	-	-	-
Initial shear velocity V_s (m/s)	140	140	230
Initial shear modulus ratio G_0/σ'_m	2002	730	1019
Failure stress ratio M_f^*	1.34	1.34	1.34
Phase transformation stress ratio M_m^*	0.91	0.91	0.91
Internal friction angle ϕ' (deg)	-	-	-
Hardening parameter B_0^* B_1^*	6000 0	1500 150	2100 140
Control parameter of anisotropy C_d	2000	2000	2000
Reference strain parameter γ_r^{p*} γ_r^{e*}	1000 1000	0.005 0.005	0.004 0.004
Dilatancy parameter D_0^* n	0.0 0.0	1.0 4.0	1.0 4.0

	Ac	As	Ds/c	Dc	Ds
Soil	Marine clay	Sand	Sand with clay	Marine clay	Sand
Model	E-VP	E-P	R-O	R-O	R-O
ρ (t/m^3)	1.67	2.00	2.00	2.00	2.00
e_0	1.41	0.50	0.50	1.20	0.50
k (cm/s)	0.0002	0.002	0.002	0.0001	0.002
λ	0.331	0.01	-	-	-
κ	0.0425	0.001	-	-	-
υ	-	-	0.35	0.35	0.35
V_s (m/s)	180	230	330	280	450
G_0/σ'_m	328	516	-	-	-
M_f^*	1.23	1.26	-	-	-
M_m^*	1.03	0.91	-	-	-
ϕ' (deg)	-	-	45	45	45
B_0^* B_1^*	55 -	5000 100	-	-	-
C_d	-	2000	-	-	-
γ_r^{p*} γ_r^{e*}		0.010 0.100	- -	- -	- -
D_0^* n		- -	0.0 0.0	- -	- -

Numerical results

A comparison of the simulated and the observed absolute acceleration histories are presented in Fig. 4.9. The amplitudes as well as the phases were reproduced in the simulation results, although the peak acceleration at depths of GL-16 m and GL-32 m were underestimated. The simulated peak acceleration was affected by the numerical parameters related to damping. In this simulation, we overestimated the damping of the lower layers more than the reclaimed layer. A comparison of the simulated and the observed relative velocity histories are presented in Fig. 4.10. The relative velocity is given by subtracting the base velocity at a depth of GL-83 m. The observed velocity was obtained by integrating the acceleration histories in the time domain. The simulation reproduced the observed velocity very well for the amplitudes and phases.

The simulated time histories of the effective stress decreasing ratio, which is given by $1.0-\sigma'_m/\sigma'_{m0}$, in reclaimed layers B2 and B3, are shown in Fig. 4.11. Complete liquefaction occurred after a few strong motion cycles around about 8 seconds in the reclaimed layer. Changes in the frequency property in the acceleration and the velocity at the ground surface are due to the liquefaction in the reclaimed layer. It is well known that extensive soil liquefaction was observed on Port Island, which is a man-made island in Kobe City (Shibata et al., 1996). It is seen that the proposed liquefaction method, based on the cyclic elasto-plasticity model, can well simulate the dynamic response of a liquefiable ground.

4.6 *Numerical analysis of the dynamic behavior of a pile foundation considering liquefaction*

Many structures were damaged during the 1995 Hyogo-ken Nambu Earthquake. It was found from the field investigations after the earthquake that not only the pile heads, but also the lower parts of the piles had cracked or failed. This phenomenon indicates that both the inertia force from the upper structures and the kinematic interaction between the piles and the ground play important roles in the mechanical behavior of piles. In particular, when the ground surrounding a structure liquefies due to seismic excitations, the behavior of the piles is more complicated. Damage related to liquefaction may involve cases in which the pile foundation is damaged due to the lateral flow of liquefied soils, and/or the piles fail at the boundary between two different soil layers, of which one liquefies while the other does not. In this study, a series of numerical simulations were conducted to study the dynamic behavior of a single-pile foundation constructed in a two-layer ground, whose upper layer is filled with sandy soil which is dense sand, reclaimed soil, medium dense sand or loose sand, respectively, and whose lower layer is filled with clayey soil employing a three-dimensional liquefaction analysis method (code name: LIQCA3D) to clarify the mechanism of the interactions among the soil-pile-structure (Lu, 2002; Oka, Lu and Zhang, 2004b).

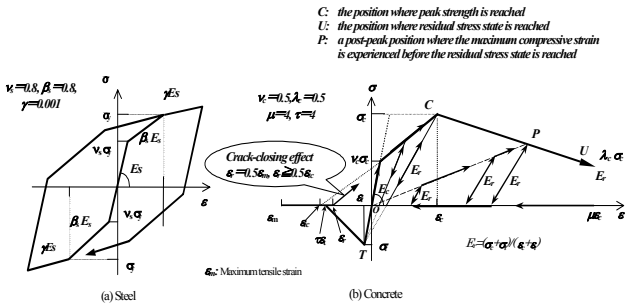

Figure 4.12. Stress-strain relations of steel and concrete adopted in the AFD model for RC material.

4.6.1 *Numerical simulation methods*

The two-layer ground considered in this paper is a typical one near the shore of a major Japanese urban city, such as Kobe. In order to study the influence of the soil characteristics, four different sandy materials are considered for an upper sandy ground, that is, dense sand, medium dense sand, loose sand, and reclaimed soil. Table 4.2 shows the parameters involved in the constitutive models for the different types of soil, in which the constitutive model for sand is described in detail in Section 4.3. On the other hand, an axial force-dependent (AFD) model (Zhang and Kimura, 2002), in which the nonlinear behavior of steel and concrete is properly described and shown in Fig. 4.12, is used to describe the dynamic behavior of the RC pile which is 1.5 m in diameter. The parameters of the RC pile are shown in Table 4.3.

The governing equations for the coupling problems between the soil skeleton and the pore-water pressure are obtained based on the two-phase mixture theory. The liquefaction analysis is formulated using a u-p. The side boundaries of the simulated system are assumed to be equal-displacement boundaries, the bottom of the system is fixed, and the boundaries are impermeable except for the surface of the ground. In this dynamic analy-

sis, a stiffness-matrix-dependent type of Rayleigh damping is adopted and the direct integration method of Newmark- β is used in this dynamic analysis with a time interval of 0.01 sec. The ground water table is 1.5 m beneath the ground surface. The mass of the superstructure is 80,000 kg and the height of pier is 8 m. Fig. 4.13 shows the seismic wave used in this study and Fig. 4.14 shows the configuration of the single-pile system and the finite element mesh used in the calculation.

4.6.2 *Results and discussions*

Fig. 4.15 shows the history of the effective stress decreasing ratio (ESDR = $(\sigma'_{m0}-\sigma'_{m})/\sigma'_{m0}$); σ'_{m0} : initial mean effective stress) of the soil in the middle of different types of sandy layers. Liquefaction occurs when ESDR is equal to 1. It can be seen that loose sand easily liquefies entirely, while medium sand and reclaimed soil almost liquefy at the end of the major seismic event (t = 10 sec). The effective stress of dense sand does not decrease much at all. Fig. 4.16 shows the histories of the bending moment at the pile head and in the pile segment at the boundary between the soil layers. Since the dense sand layer does not liquefy at all, the earthquake wave motion does not deamplify and the largest bending moment occurs at the pile head among the cases. On the other hand, the larger bending moments occur in the pile at the boundary between the layers at t = 4 sec and t = 7 sec for loose sand, and medium dense sand and reclaimed soil, respectively, when the effective stress of the sand layers decreases significantly. Fig. 4.17 shows the distribution of the bending moment when the maximum bending moment takes place in each case and Fig. 4.18 shows the distribution of the bending moment at the end of the seismic event.

The figures show that although the maximum bending moment takes place at the pile head (b15) in every case, the development of the bending moment in the ground varies due to the features of the soil.

The large bending moment takes place in the lower pile segment (b7) in the cases of liquefiable soil, but at the upper pile segment (b15) in the case of dense sand at the end of the seismic event.

4.7 *A case study of damage for a pile foundation due to liquefaction by the 1995 Hyogo-ken Nambu earthquake*

In this section, the mechanical behavior of single-pile and group-pile foundations in a two-layer ground during seismic excitation was carefully studied (Oka et al., 2004f). In reality, however, the upper structure was not an elastic beam element with a mass, but a more complicated structure. Piles should be modeled as more realistic structures. In this chapter, therefore, an actual case record will be discussed using the same numerical technique as that in the previous chapter.

The case study considered in this chapter involves a five-story building, located near East Kobe Harbor, which was damaged by the 1995 Hyogo-ken Nambu Earthquake. The effective stress based numerical analysis was conducted using a full system composed of a five-story building, a group-pile foundation, and the ground. Uzuoka et al. (2001b) studied the damage to the pile foundation employing a bilinear model to represent the M-F relation of the piles and Oka et al. (2002a) showed the influence from the AFD model on the dynamic behavior of the structure. In this study, however, a detailed examination of the seismic behavior of the structure due to the earthquake is presented.

Table 4.2: Material parameters for the soil

Soils	*Density*	M^*_f	M^*_m	G_0/σ'_{m0}	B^*_0, B^*_1, C_f	D_0,n
Loose	2.0	0.80	0.70	500.0	2500,25,0	1.0,1.0
Medium	2.0	1.00	0.80	1060.0	4000,40,0	1.0,2.0
Reclaimed	2.0	1.19	0.91	2140.0	5500,55,0	1.0,4.0
Dense	2.0	1.10	0.85	1980.0	8500,85,0	1.0,2.5
Clay	1.7	1.31	1.28	300.0	500,50,0	----

Table 4.3: Material parameters for the pile

Young's Modulus of concrete E_c (kN/m^2)	2.5×10^7
Diameter of pile D (m)	1.5
Compressive strength of concrete f_c (kN/m^2)	36000.00
Tensile strength of concrete f_t (kN/m^2)	3000.00
Degrading parameter of concrete β_C	0.20690
Young's Modulus of steel E (kN/m^2)	2.1×10^8
Diameter of reinforcement d (m)	0.029
Number of reinforcement N	24
Yielding strength of steel Y_s (kN/m^2)	3.8×10^5

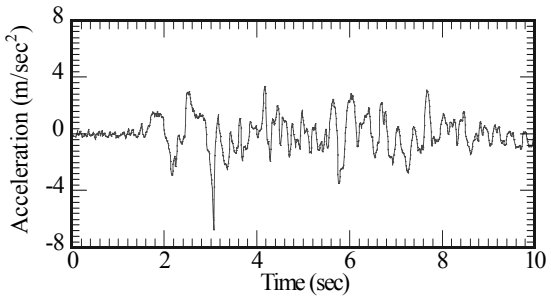

Figure 4.13. Input wave.

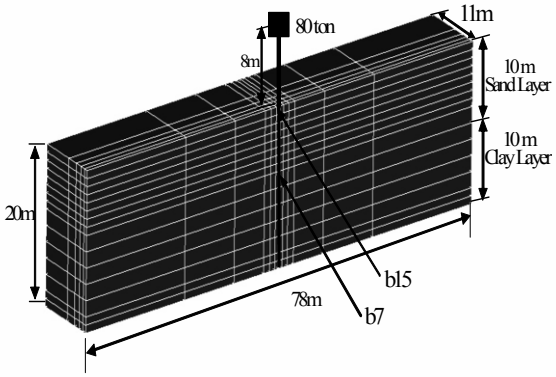

Figure 4.14. Finite element mesh.

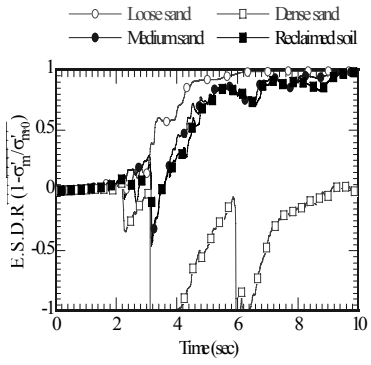

Figure 4.15. Effective stress decreasing ratio time profile.

4.7.1 *Field observations at the site*

The configurations of the piles are shown in Fig. 4.19. The piles marked with circular symbols are the piles that were checked by a soundness investigation after the earthquake. Fig. 4.20 shows the soil profile obtained through the borehole tests. The first layer of the ground is reclaimed soil with a thickness of 11 m. The second layer is alluvial clay and the third is Pleistocene soil. The ground water table is about 2.2 m beneath the ground surface. Fig. 4.21 shows the configuration of the mesh designed for the numerical simulation in this case. In the FE analysis, 4366 elements with 4803 nodes were used. The side boundaries

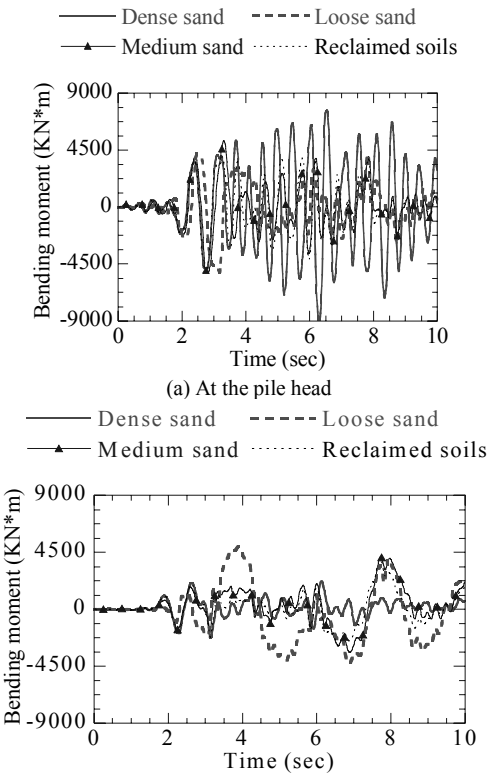

Figure 4.16. Histories of the bending moments in the pile.

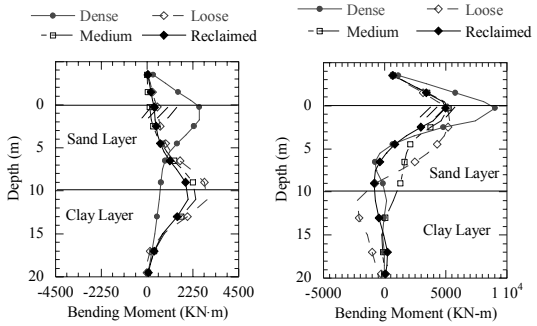

Figure 4.17. Distribution of the bending moment when the maximum bending moment takes place in each case.

Figure 4.18. Distribution of the bending moment at the end of the event.

of the simulated system were assumed to be equal-displacement boundaries. The bottom of the system was fixed and the boundaries, except for the surface of the ground, were impermeable.

The bottom of the system was fixed and the boundaries, except for the surface of the ground, were impermeable. The soil elements and the beam elements, whose numerical results will be discussed in detail later, are also shown in Fig. 4.21.

The building is located on the west side of Fukaehama, reclaimed land that was completed in 1965. The closest distance to the coastal line of the reclaimed land is about 350 m. The five-story building, made of RC material, was constructed in 1988 and is supported by several group-pile foundations. Each pile was installed by connecting several short bars made of SC piles and two PHC-A piles at different depths in the ground in order to meet the requirements of seismic design. Since the piles were made from different materials, the mesh had to be designed to reflect realistic conditions in the numerical analysis. Fig. 4.22 shows the deformation of the ground on which the building stood after the earthquake. The subsidence of the pile heads was found to be about 70 cm. The building inclined to the north at an inclination of 1/80 and to the east at an inclination of 1/30.

The superstructure itself, however, was not destroyed during the earthquake. In order to inspect the soundness of the piles, the direct observation method of the pile shaft surface, the borehole television method, and the velocity logging method were used after the earthquake. Cracks were found on piles Nos. 1, 2, and 3 and an intrusion of the soils was found in pile No. 1. Sand boiling phenomena and subsidence of the ground were also found in the area. Therefore, liquefaction of the ground must have taken place during the earthquake. Furthermore, the damage which occurred in the lower segments, located at the boundary between the sand layer and the clay layer, may have been caused by the influence of the large deformation of the reclaimed layer.

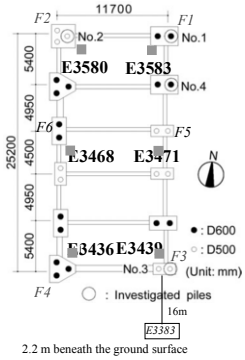

Figure 4.19. Configurations of the pile foundation, the soil elements, and the beam elements.

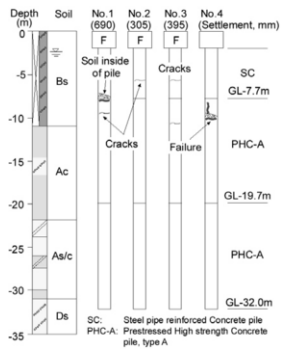

Figure 4.20. Soil profile and damage to the piles.

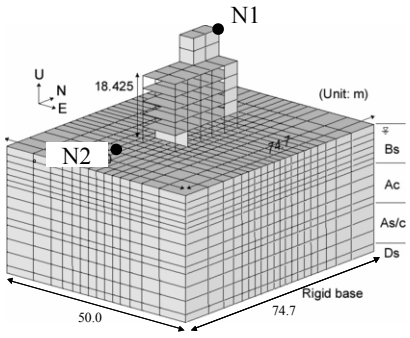

Figure 4.21. Finite element mesh used in the analysis.

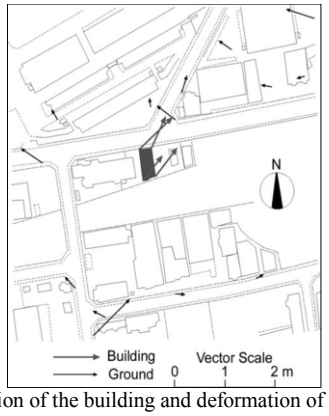

Figure 4.22. Location of the building and deformation of the ground.

4.7.2 *Numerical procedure*

The numerical analysis was conducted based on the above-mentioned technique. The piles were described using the AFD model, the superstructure was represented by an elastic beam element, the slabs and the walls were represented by shell elements, and the weight of each floor was concentrated into each slab. In the present numerical simulation, the piles in one footing were simplified as a single pile whose area and inertia moment over the x-axis and the y-axis were the sums of the original ones. The parameters for the axial force-dependent model of the piles are listed in Table 4.4. For input waves, two components of earthquake motion observed at a depth of 33 meters near the Higashi Kobe bridge during the 1995 Hyogoken-Nambu earthquake; N78E in the x direction and N348E in the y direction were used. The side boundaries of the simulated system were assumed to be equal-displacement boundaries. The bottom of the system was fixed and the boundaries, except for the surface of the ground, were impermeable. In the analysis, a stiffness-matrix-dependent type of Rayleigh damping was adopted and the direct integration method of Newmark-β was used with a time interval of 0.002 sec.

In order to simulate the mechanical behavior of the structure with a group-pile foundation, it was necessary to determine the parameters of the constitutive models for sandy soil and clayey soil. Numerical simulations of the sandy soil and the clayey soil were firstly conducted on one element. The stress paths of the reclaimed soil, which were above the groundwater table, decreased but did not reach zero. On the other hand, the stress path response of the reclaimed soil under the groundwater table (GL-2.2 m ~ GL-10.7 m) lead to a zero effective stress state. Fig. 4.23 shows a comparison between the liquefaction strength levels from the laboratory tests conducted on undisturbed samples from the field and the numerical simulations in which the parameters listed in Table 4.5 are used. In the present case, as expected, the Ac layer that is composed of a clayey soil did not liquefy.

4.7.3 *Results of a simulation by a 3-D dynamic analysis*

Comparison between the results of field observations and a numerical analysis

Fig. 4.24 illustrates a comparison in which the acceleration responses of the ground surface from the observations and the computed accelerations in the EW direction agree well with each other in phase, but slightly disagree in amplitude. The computed results are smaller than the observed ones at 6 sec for the amplitude. Accelerations in the NS direction agree well with each other in both amplitude and phase.

Fig. 4.25 shows a comparison of the velocity responses of the ground surface from the observations and the computation. The results both in NS and EW directions agree well with each other.

Table 4.4: Pile parameters

Pile types	SC	
Outer diameter D (mm)	600	500
Inner diameter D_i (mm)	510	420
Thickness T (mm)	90	80
Thickness of steel pipe t (mm)	6.0	6.0
Thickness of concrete d_c (mm)	45	40
Diameter of reinforcement ϕ (mm)	22.7	20.7
Number of reinforcements N	28	28
Compression strength of concrete σ_c (kPa)	7.84×10^4	7.84×10^4
Tensile strength of concrete σ_t (kPa)	4.7×10^3	4.7×10^3
Yielding strength of steel σ_s (kPa)	2.35×10^5	2.35×10^5
Failure bending moment M_u (kNm)	803.5	578.3
Failure curvature (1/m)	2.75×10^{-3}	3.77×10^{-3}

Pile types	PHC-A	
Outer diameter D (mm)	600	500
Inner diameter D_i (mm)	510	420
Thickness T (mm)	90	80
Thickness of steel pipe t (mm)	0.0	0.0
Thickness of concrete d_c (mm)	45	40
Diameter of reinforcement ϕ (mm)	7.1	7.1
Number of reinforcements N	19	14
Compression strength of concrete σ_c (kPa)	7.84×10^4	7.84×10^4
Tensile strength of concrete σ_t (kPa)	4.7×10^3	4.7×10^3
Yielding strength of steel σ_s (kPa)	1.27×10^6	1.27×10^6
Failure bending moment M_u (kNm)	681.1	465.9
Failure curvature (1/m)	2.48×10^{-3}	3.48×10^{-3}

E_c=4.50×10^7(kPa), E_s=2.1×10^8(kPa)

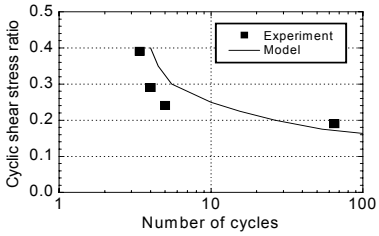

Figure 4.23. Liquefaction strength.

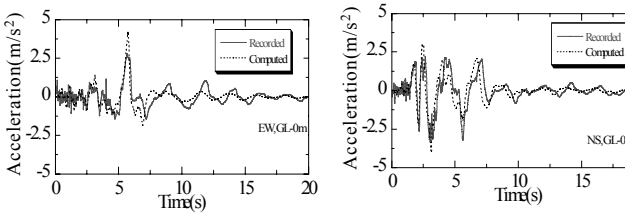

Figure 4.24. Comparisons of the acceleration responses of the ground surface.

Table 4.5: Parameters used in the analysis

Name of the soil profile	Bs	Ac
Density (t/m^3)	2.0	1.7
Initial void ratio	0.42	1.41
Coefficient of permeability (m/sec)	2.2×10^{-5}	3.8×10^{-11}
Compression index	0.0100	0.3310
Swelling index	0.0010	0.0425
Initial shear modulus ratio	1686.0	401.0
Failure stress ratio M^*_f	1.20	1.23
Phase transformation ratio M^*_m	0.91	1.03
Hardening parameter B_0, B_1, C_f for sand, B_0, B_s, C_t for clay	3500.0, 70.0, 0.0	55.0, 0.0, 0.0
Parameter of anisotropy C_d	2000.0	
Dilatancy parameter D_0, n	1.0, 4.0	
Viscoplastic parameter m', C_{01}, C_{02} (1/sec)		14.0, 5.54×10^{-6}, 7.76×10^{-7}

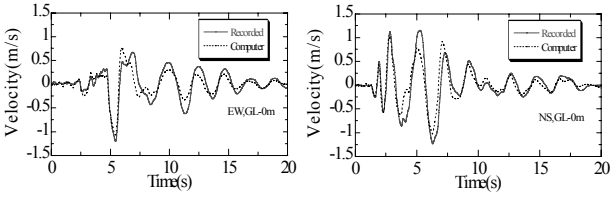

Figure 4.25. Comparisons of the velocity responses of the ground surface.

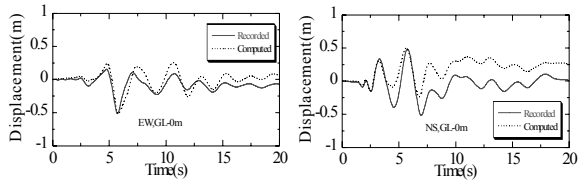

Figure 4.26. Comparisons of the displacement responses of the ground surface.

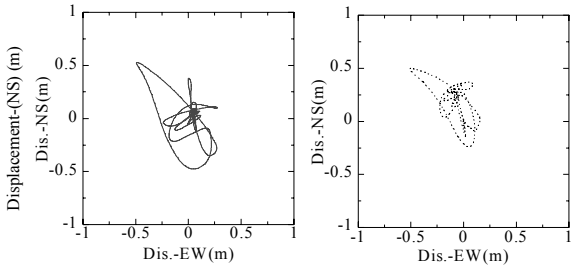

(Measured) (Computed)

Figure 4.27. Comparisons of the orbits of the displacement responses of the ground surface.

Fig. 4.26 shows a comparison of the displacement responses of the ground surface from the observations and the computation. The general tendency is for the computed results to be larger than the observed ones in the whole time duration in both NS and EW directions. The phases of the displacement responses, however, are in good agreement. It is also known that in the EW direction, the residual displacement obtained from the computation has an opposite tendency to that of the recorded data.

Fig. 4.27 shows a comparison of the orbit of the displacements of the computed and the recorded results. The computed and the observed results are in good agreement with respect to tendency.

Acceleration and lateral displacement responses

The acceleration responses of the superstructure and the ground surface at a faraway field are shown in Fig. 4.28. It was found that the acceleration responses of the building were larger than the acceleration responses of the ground. After liquefaction, the acceleration responses of both the structure and the ground surface decreased significantly.

The lateral displacements of the superstructure and the pile heads are shown in Fig. 4.29. The displacement responses of the superstructure are similar to those of the ground surface. At the end of the calculation (t =20 sec), the building inclined and remained in a residual displacement towards the NW, which is different from the observed tendency in which the building inclined towards the NE. The reason is that the computation of the analysis only considered the behavior of the pile foundation and the ground during an extensive earthquake (t= 20 sec), in which the consolidation after the major waves, which would influence the inclination of the pile foundation at an actual site, was not computed.

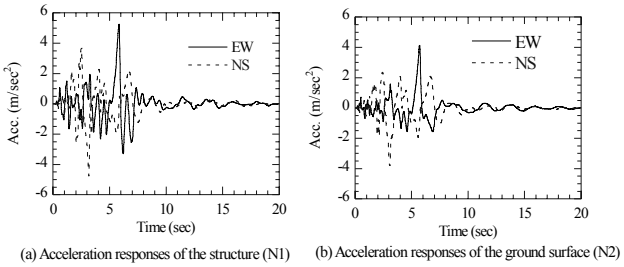

(a) Acceleration responses of the structure (N1) (b) Acceleration responses of the ground surface (N2)

Figure 4.28. Acceleration responses.

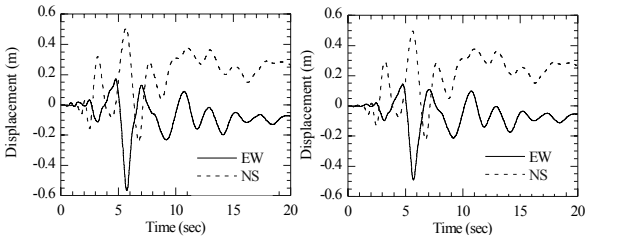

(a)Displacement responses of the structure (N1) (b) Displacement responses of the ground surface (N2)

Figure 4.29. Displacement responses in the EW and NS directions.

Effective stress decreasing ratio (ESDR)

Fig. 4.30 shows the ESDR of the soil elements around the piles at the corners, at the neighboring areas of the pile foundation, and at the faraway field shown in Fig. 4.2, respectively. It can be seen that liquefaction took place at about 8 sec and that the excess pore-water pressure ratio of the soil elements around footings F2 and F5 developed significantly, while the others did not. It shows that the interaction between these soil elements and the piles remained intensive after liquefaction. It was also found that the liquefaction of the soils within the foundation occurred faster than that of the soils at the faraway field. One possible reason for this is that the soil within the foundation was not firmly confined by the group piles, which were separated from each other at quite large distances.

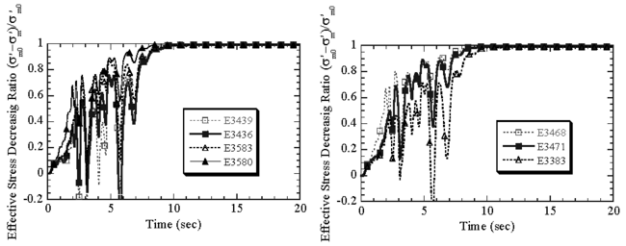

(a) Surrounding the piles at the corners (b) Within foundation and at faraway field

Figure 4.30. Decreasing effective stress ratio of different soil elements.

Curvature responses

Fig. 4.31 shows a so-called resultant curvature, whose value is equal to the root of the summation of the square of the curvature in the x direction plus the square of the curvature in the y direction, at the pile head and at the bottom of the reclaimed layer for F1 to F4, respectively. The curvature reached a large value at about the 6 sec point, when a large acceleration in the x direction also took place at N1. The curvature responses show a longer period after liquefaction and a large residual curvature remaining on F3, which corresponds to the location of the cracks examined by the investigation at pile No. 3. In Fig. 4.31(b), the curvature responses express a large value at about the 7 sec point. Compared to the upper part of the piles, the curvature of the piles at the bottom of the reclaimed layer after liquefaction vibrated for a relatively shorter period, indicating that the kinematic behavior of the interaction between the soil and the piles at the bottom of the Bs layer is different from that at the pile head.

According to Table 4.4, the failure curvatures of D = 500 mm and D = 600 mm of the SC pile and the PHC-A pile are 2.48×10^{-3} and 3.48×10^{-3} (1/m), respectively. In Fig. 4.31(a), the curvature response at the pile heads exceeds both failure curvatures of D =500 mm and D = 600 mm, which shows that the pile segments would be damaged due to the earthquake. In addition, it can be seen that the curvature responses of the segment at the bottom of the reclaimed (Bs) layer exceed the failure curvatures for both D = 500 mm and D = 600 mm.

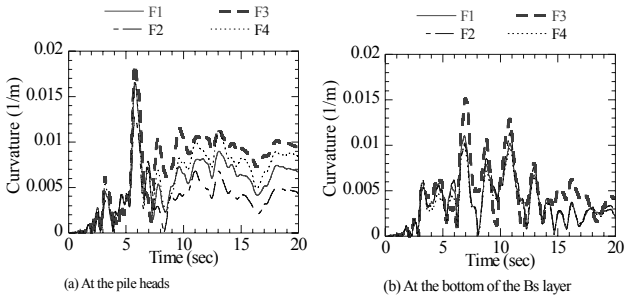

Figure 4.31. Time histories of the curvature responses at different locations.

4.8 *Summary*

In the first part of the present chapter, studies on the liquefaction analysis method and the constitutive model for sand, which are applicable for a liquefaction analysis, were reviewed. Then, the liquefaction analysis method was presented with a cyclic elasto-plastic model for sand. Finally, the application of the method to the liquefaction of a ground and a soil pile foundation-structure were demonstrated and discussed.

A cyclic elasto-plastic model for sand was successfully applied to medium to dense sand. It was confirmed that the model is applicable for the behavior of sand with a wide range of relative densities. Then, three-dimensional dynamic finite element analyses were conducted for a single pile foundation, based on the model and Biot's theory, to investigate the mechanical behavior of the pile foundation when its surrounding ground had experienced liquefaction. The following conclusions were obtained:

1) The maximum bending moment at pile heads in a non-liquefied ground are larger than those in a liquefiable ground;
2) The liquefaction process may greatly increase the bending moment and the shear force of the piles at the boundary between two different layers;
3) The responses in the cases of a medium dense sand and reclaimed soil are similar to those in the case of dense sand at the beginning;
4) After the effective stress decreases significantly in the cases of medium dense sand and reclaimed soil, the response becomes similar to that of loose sand.

A case study, in which a building located on reclaimed land in Fukaehama, near Kobe City, was damaged in the 1995 Hyogo-ken Nambu Earthquake, was presented by a 3-D effective stress analysis using FEM. In order to properly simulate the mechanical behavior of the soil, the parameters used in the constitutive models for the soil were carefully investigated with laboratory tests and the liquefaction strength curve was examined. As a result, the computed acceleration responses, velocity responses, and displacement responses of the ground surface agreed well with the observations. The following points can be clarified:

1) The occurrence of liquefaction shelters the upper structure from being excited by an earthquake.
2) The occurrence of liquefaction causes a large bending moment and shear stress to develop in the pile segment at the boundary between the liquefied and the non-liquefied soil layers which may damage the piles.
3) The distance between the piles installed in the footing influences the buildup of excess pore-water pressure.
4) The damage to both the pile heads and the low segments of the pile at the boundary takes place before the completion of the liquefaction during these major earthquakes.
5) Even if the lateral spread of the ground does not occur, the damage to the piles due to liquefaction may still take place.

ACKNOWLEDGMENTS

The author wishes to express his sincere thanks to Emeritus Professor H.Aboshi of Hiroshima University, Emeritus Professor T.Adachi of Kyoto University, Professor, S.Leroueil of Laval University, Dr. YoungSeok Kim, and Mr. Md.R.Karim, Mr. B.Siribumrungwong Doctoral course students of Kyoto University (Hereinabove for chapter 2); Emeritus Professor T.Adachi of Kyoto University, Professor A.Yashima and Associate Professor F.Zhang of Gifu University, Associate Profesor T.Kodaka, and Dr. S.Kimoto of Kyoto University, Dr. Y.Higo, Mr. T.Takyu, Mr. T.Satomura, Mr. N.Nishimatsu, and Ms. T.Ichinose, former students of Kyoto University (Hereinabove for chapter3); Associate Professor R. Uzuoka of Tohoku Univ., Dr. K.Sekiguchi of JFE, Dr. A.Tateishi , Dr. Y.Taguchi of Taisei Corporation, Dr. S.Sunami of NIKKEN SEKKEI LTD, Dr. M.Kato of Konoike Construction Company, Professor A.Yashima of Gifu University, Dr. C.-W.Lu of National Kaohsiung First University of Science and Technology, Kaohsiung Taiwan R.O.C., and Associate Professor F.Zhang of Gifu University, Dr. O.Matsuo of PWRI, Mr. K.Yamada of Kobe City, Mr. Nishiraku of SHO-BOND Construction, Inc., Mr. Koike of A & D Design Consultant, Inc. (Hereinabove for Chapter 4), Associate Professor T.Kodaka and Dr. S.Kimoto of Kyoto University, and graduate students of the Geomechanics Laboratory of Kyoto University for their contributions and discussions.

REFERENCES

Abghari, A. and Chai, J. 1995. Modeling of soil-pile-superstructure interaction in the design of bridge foundations, Performance of Deep Foundation under Seismic Loading, J.Turner, ed., *Geotechnical Special Publication* No 51, ASCE, New York, N. Y., 45-49.

Aboshi, H. 1973. An Experimental investigation on the similitude of consolidation of a clay including secondary creep settlement, *Proc. 8th ICSMFE*, 4(3), 88.

Aboshi, H. and Matsuda, H. 1981. Secondary compression of clays and its effect on settlement analysis, *Tsuchi-to-Kiso JSSMFE*, 29(3), 19-24 (in Japanese).

Aboshi, H. 1988. Private communication.

Aboshi, H. 1995. Case records of long-term measurement of consolidation settlement and their predictions, *Proc. Int. Symp. on Compression and Consolidation of Clayey Soils*, H.Yoshikuni and O.Kusakabe eds., Balkema, 2, 847-872.

Aboshi, H. 2004. Long-term effect of secondary consolidation on consolidation settelement of marine clays, *Advances in Geotechnical Engineering: The Skempton Conference2004*, Thomas Telford, London, 345-356.

Adachi, T. and Okano, M. 1974. A constitutive equation for normally consolidated clay, *Soils and Foundations*, 14(4), 55-73.

Adachi, T. and Oka, F. 1982a. Constitutive equations for normally consolidated clay based on elasto-viscoplasticity, *Soils and Foundations*, 22(4), 55-70.

Adachi, T. and Oka, F. 1982b. Constitutive equations for sands and overconsolidated clays and assigned works for sand. Results of the International Workshop on Constitutive Relations for Soils, Grenoble, 141-157.

Adachi, T., Oka, F. and Mimura, M., 1985. Descriptive accuracy of several existing constitutive models for normally consolidated clays, *Proc. 5th Int. Conference on Numerical Methods in Geomechanics*, Nagoya, T.Kawamoto, and Y.Ichikawa eds., Balkema, 1, 259-266.

Adachi, T., Oka, F. and Mimura, M. 1987a. An elasto-viscoplastic theory for clay failure, *Proc. 8th Asian Regional Conference on Soil Mechanics and Foundation Engineering*, Kyoto, 1, JSSMFE, 5-8.

Adachi, T., Oka, F. and Mimura, M. 1987b. Mathematical structure of an overstress elasto-viscoplastic model for clay, *Soils and Foundations*, 27(3), 31-42.

Adachi, T., Oka, F. and Mimura, M. 1988. Elasto-viscoplastic constitutive equations for clay and its application to consolidation analysis, *Proc. Symposium on Constitutive Modeling for Engineering Materials with Applications*, ASME Winter Annual Meeting, Chicago, PVP-No.153, D.Hui and T.J.Kozik eds., ASME, 41-50.

Adachi, T., Oka, F. and Mimura, M. 1990. Elasto-viscoplastic constitutive equations and its application to consolidation analysis, *J. of Engineering Materials and Technology*, ASME, 112, 202-209.

Adachi, T., Oka, F. and Poorooshasb, H.B. 1990. A constitutive model for frozen sand, *J. of Energy Resources Technology*, ASME,112, 208-212.

Adachi, T. and Oka, F. 1995. An elasto-plastic constitutive model for soft rock with strain softening, *Int. J. Numerical and Analytical Methods in Geomechanics*, 19, 233-247.

Adachi, T., Oka, F., Osaki, H. and Zhang, F., 2000. Soil-water coupling analysis of progressive failure in cuts with a strain softening model, *Constitutive modeling of granular materials*, D.Kolymbas ed., Springer, 471-490.

Adachi,T. and Oka, F. and Koike, M. 2003. An elasto-viscoplastic constitutive model with strain softening for a sedimentary soft rock, *Proc. of Int. Workshop on Prediction and simulation methods in Geomechanics*, Athens, F.Oka, I.Vardoulakis, A.Murakami and T.Kodaka eds., JGS, 5-8.

Adachi, T., Oka, F. and Koike, M. 2005. An elasto-viscoplastic constitutive model with strain-softening for soft sedimentary rocks, *Soils and Foundations*, to appear.

Aifantis, E.C. 1984. On the microstructural origin of certain inelastic models, *Journal of Engineering Materials and Technology*, ASME, 106, 326-330.

Aifantis, E.C., Oka, F., Yashima, A. and Adachi, T. 1999. Instability of gradient dependent elasto-viscoplasticity for clay. *Int. J. Num. Anal. Meth. in Geomechanics* , 23, 973-994.

Akai, K., Adachi, T. and Oka, F. 1981. Constitutive models for clays and sands, *Proc. Int. Workshop on Limit Equilibrium*, Plasticity and Generalized Stress-Strain in Geotechnical Engineering, Montreal, ASCE, 815-838

Alonso, E.E., Gens, A. and Josa, A. 1990. A constitutive model for partially saturated soils, *Géotechnique*, 40(3), 405-430.

Anand, L. 1983. Plane deformations of ideal granular materials, *J. Mech. Phys. Solids*, 31(2), 105-122.

Anandarajah, A., Rashidi, H. and Arulanandan, K. 1995. Elasto-plastic finite element analysis of a soil-structure system under earthquake excitation, *Computers and Geotechnics*, 17, 301-325.

Armstrong, P. J. and Frederick, C.O. 1966. A mathematical representation of the multiaxial Baushinger effect, Report RD/B/N 731.

Arthur, J.R.F., Dustan, T., Al-Ani, Q.A.J. and Assadi, A. 1977. Plastic deformatin and failure of granular media, *Géotechnique*, 27, 53-74.

Arulanandan, K., Shen, C.K. and Young, R.B. 1971. Undrained creep behaviour of a coastal organic clay, *Géotechnique*, 21(4), 359-375.

Arulanandan, K., Li, X.S. and Sivathasan, K. 2000. Numerical simulation of liquefaction-induced deformations, *J. Geotech. and Geoenvironmental Engng.*, ASCE, 126(7), 657-666.

Asaoka, A., Nakano, M. and Noda, T. 1997. Soil-water coupled behavior of heavily overconsolidated clay near/at critical state, *Soils and Foundations*, 37(1), 13-28.

Asaoka, A. 2003. Consolidation of clay and compaction of sand-an elasto-plastic description, *Proc. 12th Asian Conference on SMGE, Singapore*, C.F.Leuong, K.K.Phoon, Y.K.Chow and C.I.Teh and K.Y.Yong eds., World Scientific, 2, 1157-1195.

Aubry, D., Kodaissi, E. and Meimon, Y. 1985. A viscoplastic constitutive equation for clays including a damage law, *Proc. 5th Int. Conf. on Numerical Methods in Geomechanics*, Nagoya, T.Kawamoto and Y.Ichikawa eds., Balkema, 1, 421-428.

Aubry, D. and Moderessi, H. 1989. A model for the non-linear dynamic analysis of saturated soils, Revue Francaise *Géotechnique,* 46, 43-75.

Baladi, G.Y. and Rohani, B. 1984. Development of an elasto-viscoplastic constitutive relationship for earth materials, *Mechanics of Engineering*, C.S.Desai, and R.H.Gallerger eds., J. Wiley and Sons Ltd., 23-43.

Bauer, E. and Huang, W. 2001. Evolution of polar quatities in a granular Cosserat materisl under shearing, *Proc. 5th Int. Workshop on Bifurcation, Localization Theory in Geomechanics*, H.B.Mühlhaus et al. eds., Balkema, 227-238.

Benallal, A. and Comi, C. 2002. Material instabilities in inelastic saturated porous media under dynamic loadings, *Int. J. Solids and Structures*, 39, 3693-3716.

Benallal, A. and Comi, C. 2003. Perturbation growth and localization in fluid-saturated inelastic porous media under quai-static loadings, J. *Mech. Phys. Solids*, 51, 851-899.

Bigoni, D. and Hueckel, T. 1991. Uniqueness and localization –I, Associative and non-associative plasticity, *Int. J. Solids and Structures*, 28, 197-213.

Biot, M.A. 1956. Theory of propagation of elastic waves in a fluid-saturated porous solid, *J. Acoustic Society of America,* 28(2): 168-178.

Biot, M.A. 1962. Mechanics of deformation and acoustic propagation in porous media, *J. Appl. Phys.*, 33(4), 1482-1498.

Bishop, A.W. 1960. The measurement of pore pressure in the triaxial test, *Proc. Conf. on Pore pressure and suction in soils, British Nat. Soc. of ISSMFE*, Butterworth, 38-46.

Bishop, A.W. and Lovenbury, H.T. 1969. Creep characteristics of two undisturbed clays, *Proc. 7th Int. Conf. on Soil Mechanics and Foundation Engrg.*, Mexico City, 1, 29-37.

Boehler, J.P. and Sawczuk, A. 1977. On yielding of oriented solids, *Acta Mechanica*, 27, 185-206.

Bolzon, G., Schrefler, B.A. and Zienkiewicz, O.C. 1996. Elasto-plastic soil constitutive laws generalized to semisaturated states, *Géotechnique*, 46(2), 279-289.

Borja, R.I. 2004. Computationa modeling of deformation bands in granular media, II Numerical simulations, *Methods in Applied Mechanics and Engineering*, 193, 2699-2718.

Borja, R.I. and Aydin, A. 2004. omputationa modeling of deformation bands in granular media, I Geological and mathematical framework, *Computer Methods in Applied Mechanics and Engineering*, 193, 2667-2698.

Boudali, M., Leroueil, S. and Murthy, S. 1994. Viscous behaviour of natural soft clays, *Proc. 13th ICSMFE*, 1, 411-416.

Brown, D.A., Morrison, C. and Reese, L.C. 1988. Lateral load behavior of pile group in sand, *Journal of Geotechnical Engineering*, ASCE, 114(11), 1261-1276.

Castellanza, R. and Nova, R. 2003. Compaction bands in oedometeric tests on cemented granular soils, *Proc. of Int. Workshop on Prediction and Simulation Methods in Geomechanics*, Athens, F.Oka, I.Vardoulakis, A.Murakami and T.Kodaka eds., JGS, 37-40.

Chaboche, J.L. and Rousselier, G. 1983. On the plastic and viscoplastic constitutive equations, part I and part II, *J. Pressure Vessel Techno. Trans.* ASME, 105, 153-164.

Chambon, R., Desrues, J., Charlier, R. and Hammad, W. 1994. Cloe, a new rate type constitutive model for geomaterials, Theoretical basis and implementation, *Int. J. Num. Anal. Meth. in Geomechanics*, 18, 4, 253-278.

Chambon, R., Crochepeyre, S. and Desrues, J. 2000. Localization criteria for non-linear constitutive equations of geomaterials, *Mechanics of Cohesive-Frictional Materials*, 5, 61-82.

Chowdhury, E.Q. and Nakai, T. 2001.An unconventional approach of elastoplastic modeling of soils, *Bifurcation and Localization Theory in Geomechanics*, H.-B.Mühlhaus, A.V.Dyskin, and E.Pasternak eds., Balkema, 193-200.

Cleall, P.J., Thomas, H.R., Seetharam, S.C. and Melhuish, T.A. 2004. *Proc. 9th Numerical Models in Geomechanics*, G.N.Pande and S.Pietruszczak eds., Balkema, 311-317.

Cui, Y.J. and Delage, P. 1996. Yielding and plastic behaviour of an unsaturated compacted silt, *Géotechnique,* 46(2), 291-311.

Cundall, P.A. and Strack, O.D.L. 1979. A discrete numerical model for granular assemblies, *Géotechnique*, 29(1), 47-65.

Dafalias, Y. 1982. Bounding surface elasto-viscoplasticity for particulate cohesive media, *Proc. of IUTAM Conf. on Deformation and Failure of Granular Materials,* P.A.Vermeer and H.J.Luger eds., Balkema, 97-107.

Darve, F. 2000. Instabilities in granular materials and application to landslides, *Mech. Cohesive-Frictional Materials*, 5(8), 627-652.

Darve, F. 2001. Modes of rupture in geomaterials, *Proc. Int. Workshop on Deformation of Earth Materials*, TC34, ISSMGE, Sendai, F.Oka ed., 39-50.

de Boer, R. 1996. *Theory of porous media*, highlight in the historical development and current state, Springer.

de Josselin de Jong, G. 1977. Mathematical elaboration of the double-sliding, free-rotating model, *Archs Mech.*, 29, 561-591.

Desai, C. S. and Siriwardane, H. J. 1980. A concept of correction functions to account for non-associative characteristics of geologic media. *Int. Journal for Numerical and Analytical Methods in Geomechanics*, 4, 377-387.

Desrues, J. 1990. Shear band initiation in granular materials:experiments and theory, *Geomaterials Constitutive Equations and Modeling*, F.Darve ed., Elsevier Appl. Science, 283-310.

Desrues, J., Chambon, R., Mokni, M. and Mazerolle, F. 1996. Void ratio evolution inside the shear band in triaxial sand specimen studied by computer tomography, *Géotechnique*, 46(3), 529-546.

Di Benedetto, H., Tatsuoka, F. and Ishihara, M. 1997. Time-dependent deformation characteristics of sand and their constitutive modeling, *Soils and Foundations*, 42(2), 1-22.

DiMaggio, F.L. and Sandler, I.S. 1971. Material model for granular soils, *J. Engineering Mech*., ASCE, 97, EM 3, 935-950.

Dragon, A. and Mroz, Z. 1979. A model for plastic creep of rock-like materials accounting for the kinematics of fracture, *Int. J. Rock Mech. Min. Sci. and Geomecahncis*, Abstr., 16, 253-259.

Drucker, D.C. and Prager, W. 1952. Soil Mechanics and plastic analysis or limit design, *Q. Appl. Math*., 10, 157-164.

Duvaut, G. and Lions, J.L. 1976. *In equalities in mechanics and physics*, Springer-Verlag.

Earthquake Engineering Committee, JSCE, 2003. Soil liquefaction under level II earthquake motion subcommittee, Report on the Soil Liquefaction under Level II Earthquake Motion (F.Oka, K.Furuya and R.Uzuoka), 157-201.

Ehlers, W. and Volk, W. 1998. On the theoretical and numerical methods in the theory of porous media based on polar and non-polar elasto-plastic solid materials, *Int. J. Solids and Structures*, 35(34)-(35), 4597-4617.

Ehlers, W. 2002. Foundations of multiphasic and porous media, *Porous media: Theory, Experiments and Numerical Applications*, W.Ehlers and J.Blume eds., Springer, 3-86.

Eyring, H. 1936. Viscosity, plasticity, and diffusion as example of absolute raction rates, J. *Chemical Phys.*, 4(4), 283-291.

Finn, W.D.L. and Shead, D. 1973. Creep and creep rupture of an undisturbed sensitive clay, *Proc. 8th ICSMFE*, 1.1, 135-142.

Finn, W. D. L., Thavaraj, T. and Wu, G. 1997. Nonlinear Seismic Response of Pile Foundations during Strong Earthquake Shaking", *Proc. of Int. Symp. Seismic Behavior of Ground and Getechnical Structure*, Seco e Pinto ed., Balkema, 195-204.

Finno, R.J., Viggiani, G., Harris, W.W. and Mooney, M.A. 1998. Localization of strains in plane strain compression of sand, *Proc. 4th Int. Workshop on Localization and Bifurcation Theory for Soils and Rocks*, T.Adachi, F.Oka and A.Yashima eds., Gifu, Balkema, 249-258.

Frantziskonis, G. 1993. Crack pattern related universal constants, *Probabilities and Materials*, Tests, Models and Applications, D.Breysse ed., Kluwer Academic Pub. 361-376.

Fredlund, D.G. and Morgenstern, N.R. 1977. Stress state variables for unsaturated soils, *J.Geotech.Eng.* Div. ASCE, 103, GT5, 447-466.

Gajo, A. and Muir Wood, D. 1999. A kinematic hardening constitutive model for sands: the multiaxial formulation. *Int. J. Num. and Anal. Meth. in Geomech.*, 23, 925-965.

Ghaboussi, J. and Wilson, E.L. 1972. Variational formulation of dynamics of fluid saturated porous elastic solids, ASCE, EM, 98, EM4, 947-963.

Ghaboussi, J. and Momen, H. 1979. Plasticity model for cyclic behaviour of sands. *Proc. 3rd Int. Conf. on Numerical Methods in Geomechanics*, Aachen, 423-434.

Gudehus, G. and Nübel, K. 2004. Evolution of shear bands in sand, *Géotechnique*, 54(3), 187-201.

Hara, K., Tatsuoka, F. and Sato, T. 1984. Detailed stress-strain behaviour of sand under cyclic undrained torsional shear. *Proc. of 19th Annual Meeting on SMFE, Matsuyama*, 577-580 (in Japanese).

Hashiguchi, K. 1980. Constitutive equations of elastoplastic materials with elastic-plastic transition, *J. Appl. Mechanics*, ASME, 47, 266-272.

Hashiguchi, K. 1989. Subloading surface model in unconventional plasticity, *Int. J. Solids and Structures,* 25, 917-945.

Hashiguchi, K. and Tsutsumi, S. 2003. Shear band formation analysis in soils by the subloading surface model with tangential stress rate effect, *Int. J. Plasticity,* 19, 1651-1677.

Higo, Y. 2003. Instability and strain localization analysis of water-saturated clay by elasto-viscoplastic constitutive models, Doctoral thesis, Kyoto University.

Higo, Y., Oka, F., Jiang, M. and Fujita, Y. 2005a. Effects of transport of pore water and material heterogeneity on strain localization of fluid-saturated gradient-dependent viscoplastic geomaterial, *Int. J. Num. and Anal. Meth. in Geomechanics*, 29, 495-523.

Higo, Y., Oka, F., Kodaka, T. and Kimoto, S. 2005b. Three-dimensional strain localization of water-saturated clay and numerical simulation using an elasto-viscoplastic model, *Philosophical Magazine*, submitted.

Higuchi, M., Kawakami, Y., Yashima, A. and Zhang, F. 2001. 3-D finite element analysis of ground-pile foundation-super structure System using an effective stress method, *Proc. of 36th Japan National Conference on Geotechnical Engineering*, 1780-1781 (in Japanese).

Hill, R. 1950. The mathematical theory of plasticity, Oxford Clarendon Press.

Hill, R. 1958. A general theory of uniquness and stability in elastic-plastic solids, *J. Mech. and Phys. of Solids*, 6, 239-249.

Hill, R. Acceleration waves in solids. 1962. *J. Mech. Phys. Solids*; 10: 1-16.

Hill, R. and Hutchinson, J.W. 1975. Bifurcation phenomena in the plane strain test, *J. Mech. Phys. Solids,* 23, 239-264.

Hohenemser, K. and Prager,W. 1932. Uber die Ansatze der Mechanik isotroper Kontinua, ZAMM, 12, 216-226.

Hori, M. 1974. Fundamental study of wave propagation characteristics through soils, Doctoral Thesis, Kyoto University.

Houlsby, G.T. 1997. The work input to an unsaturated granular material, *Géotechnique*, 47(1), 193-196.

Hughes, T.J.R. and Taylor, R.J. 1978. Unconditionally stable algorithms for quasi-static elasto-viscoplastic finite element analysis. *Computers and Structures*, 8, 169-173.

Imposimato, S. and Nova, R. 1998. An investigation on the uniquness of the incremental response of elasto-plastic models for virgin sand, *Mech. Cohesive - Frictional Materials*, 3, 65-87.

Ishihara, K. and Kabilamany, K. 1990. Stress dilatancy and hardening laws for rigid granular model of sand. *Soil Dynamics and Earthquake Engineering,* 9(2), 66-77.

Iwasaki, T. and Tatsuoka, F. 1977. Effects of grain size and grading on dynamic shear moduli of sands, *Soils and Foundations,* 17(3), 19-35.

Jommi, C. 2000. Remarks on the constitutive modeling of unsaturated soils, *Experimental evidence an theoretical approaches in unsaturated soils*, A.Tarantio and C.Mancuso eds., Balkema, 139-153.

Kabbaj, M., Oka, F., Leroueil, S. and Tavenas, F. 1985. Consolidation of natural clays and laboratory testing, Consolidation of Soils: Testing and Evaluation, ASTM Special Technical Publication 892, R.N.Yong and F.C.Townsend eds., 378-404.

Kabbaj, M., Tavenas, F. and Leroueil, S. 1988. In situ and laboratory stress-strain relationships, *Géotechnique,* 38(1), 83-100.

Karim, Md. R. and Oka, F. 2005. Simulation of consolidation behavior of soft sensitive clay using an elasto-viscoplastic constitutive model, *Proc. 40th Annual Meeting of JGS*.

Kato, M., Oka, F., Yashima, A. and Tanaka, Y. 1994. Dissipation of excess pore water pressure by gravel drain and its analysis. *Tsuchi-to-Kiso*, JSSMFE, 42(4), 39-44 (in Japanese).

Kato, R., Oka, F., Kodaka, T., Sunami, S. and Kimoto, S. 2005. Unsaturated seepage flow deformation coupled analysis of river dike embankment, *Proc. 40th Annual Meeting of JGS* (in Japanese).

Katona, M.G. 1984. Evaluation of visoplastic cap model, *J.Geotech. Engng*., ASCE, 110(8), 1106-1125.

Kim, YoungSeok, Kimoto, S., Oka, F. and Kodaka, T. 2005. Numerical simulation of the triaxial compression behaviour of unsaturated silt using an elasto-viscoplastic model, *Proc. 11th IACMAG*, Trino, to appear.

Kim, YoungSeok. 2004. Elasto-viscoplastic modeling and analysis for cohesive soil considering suction and temperature effects, Doctoral thesis, Kyoto University.

Kimoto, S. 2002. Constitutive models for geomaterials considering structural changes and anisotropy, Doctoral thesis, Kyoto University.

Kimoto, S. and Oka, F. 2004. Numerical study on the effects of strain rate and structure on the consolidation process of soft clay deposits, *Proc. Int. Symp. on Engineering Practice and Performance of Soft Deposits*, T.Matsui et al. eds., IS-Osaka, JGS, June 2nd-4th, 105-108.

Kimoto, S., Oka, F. and Higo, Y. 2004. Strain localization analysis of elasto-viscoplastic soil considering structural degradation, *Int. J. Computer Methods in Applied Mechanics and Engineering*, 193(27-29), 2845-2866.

Kimoto, S. and Oka, F. 2005. An elasto-viscoplastic model for clay considering destructuration and consolidation analysis of unstable behavior, *Soils and Foundations,* to appear.

Kimura, M. and Zhang, F. 2000. Seismic evaluations of pile foundations with three different methods based on three dimensional elasto-plastic finite element analysis, *Soils and Foundations*, 40(5), 113-132.

Kishino, Y. 1988. Discrete model analysis of granular media, M.Satake and J.T.Jenkins eds., *Poromechanics and granular media*, Elsevier, 285-292.

Kodaka, T., Higo, Y. and Takyu, T. 2001. Deformation and failure characteristics of rectangular clay specimens under three-dimensional condition, *Proc. 15th ICSMGE,* Istanbul, 1, 167-170.

Kodaka, T., Ohno, Y. and Takyu, T. 2005. Cyclic shear characteristics of treated sand with colloidal silica grout, *Proc. 16th ICSMGE*, Osaka September 2005.

Kohgo, Y., Nakano, M. and Miyazaki, T. 1993. Theoretical aspects of constitutive modeling for unsaturated soils, *Soils and Foundations*, 33(4), 49-63.

Kolymbas, D. and Rombach, G. 1989. Shear band formation in generalized hypoplasticity.Ingenieur-Archive, 59, 177-186.
Kolymbas, D. 1991. An outline of hypoplasticity, *Arch. Applied Mechanics*, 61, 143-151.
Kondner, R.L. and Ho, M.M.K. 1965. Viscoelastic response of a cohesive soil in the frequency domain, *Trans. Soc. of Rheology*, 9(2), 329-342.
Ladd, C.C., Foott, R., Ishihara, K., Schlosser, F. and Poulos, H.G. 1977. SOA-Report, Stress-deformation and strength characteristics, *Proc. 9th ICSMFE*, Tokyo, JSSMFE, 2, 421-494.
Lade, P. 1992. Static instability and liquefaction on loose fine sandy slopes, *J. Geotech. Engng*., ASCE, 118, 51-71.
Lade, P. 2003. Analysis and prediction of shear banding under 3D conditions in granular materials, *Soils and Foundations*, 43(4),161-172.
Leroueil, S. 1988. Recent developments in consolidation of natural clays, Tenth Canadian Geotechnical Colloquium, *Can. Geotech. J.*, 25, 85-107.
Leroueil, S. 1995. Could it be that clays have no unique way of behaving during consolidation?, *Proc. Int. Symp. on Compression and Consolidation of Clayey Soils*, H.Yoshikuni and O.Kusakabe eds., Balkema, 2, 1039-1048.
Leroueil, S. and Hight, D.W. 2003. Behaviour and properties of natural soils and soft rocks, *Characterization and Engineering Properties of Natural Soils*, T.S.Tan et al. eds., Swets and Zeitlinger, 29-254.
Leroy, Y. 1991. Linear stability analysis of rate dependent discrete systems, *Int. J. Solids and Structures*, 27(6), 783-808.
Li, K.N. and Otani, S. 1993. Multi-spring Model for 3-dimensional Analysis of RC Members, *Journal of Structural Engineering and Mechanics,* 1(1), 17-30.
Li, K.N., Kubo, T. and Xiao, Y. 1999a. Analysis of circular RC member in MS/FIBER model, summaries of technical papers of annual meeting (Hiroshima), St. II, AIJ, 573-574.
Li, X.S., Dafalias, Y. F., and Wang, Z.L. 1999b. State-dependent dilatancy in critical-state constitutive modeling of sand. *Can. Geotech. J.,* 36, 2, 599–611.
Lin, C.-H. 2000. Dynamic theory of mixtures and its finite element implementation for non linear analysis of round motion induced by seismic shaking, Ph D Thesis, Stanford Univ.
Loret, B. and Prévost, J.H. 1991. Dynamic strain localization in fluid-saturated porous media. *J. Engng. Mech*., ASCE, 11, 177-190.
Lu, C.-W. 2002. Numerical study of soil-pile interaction during earthquakes considering liquefaction, Doctoral thesis, Kyoto University.
Makris, N., Gazetas, G. and Delis, G. 1996. Dynamic soil-pile-foundation-structure interaction: Records and Predictions, *Géotechnique*, 46(1), 33- 50.
Mandel, J. 1964. Conditions de stabilite et postulat de Drucker, *Proc. IUTAM Symp. on Rheology and Soil Mechanics*, J.Kravtchenko and P.M.Sirieys eds., Springer, 58-67.
Masing, G. 1926. Eigenspannungen und verfestigung beim messing. *Proc. 2nd Int. Congr. Appl. Mech.,* Zurich, 332-335.
Matiotti, R., di Prisco, C. and Nova, R. 1995. Experimental observations on static liquefaction of loose sands, *Earthquake Engineering*, K.Ishihara ed., Balkema, 817-822.
Matsui, T. and Abe, N. 1985. Elasto/viscoplastic constitutive equation of normally consolidated clays based on flow surface theory, *Proc. 5th ICONMG*, 1, 407-413.
Matsuoka, H. and Nakai, T. 1974. Stress-Deformation and strength characteristics of soil under three different principal stresses, *Proc. JSCE*, 232, 59-70.
Matsuoka, H. and Nakai, T. 1985. Relationship among Tresca, Mieses, Mohr-Coulomb and Matsuoka-Nakai failure criterion, *Soils and Foundations*, 25(4), 123-128.
Mehrabadi, M.M. and Cowin, S.C. 1978. Initial planar deformation of dilatant granular materials, *J. Mech. Phys. Solids,* 26, 269-284.
Mesri, G. and Rokhsar, A. 1974. Theory of consolidation of clays, JGED, ASCE, 100, GT8, 889-904.
Mesri, G. and Choi, Y.K. 1979. Excess pore water pressure during consolidation, *Proc. 6th Asian Regional Conf. on SMFE*, 1, 151-154.
Mesri, G. and Choi, Y.K. 1985. The uniqueness of the end-of-primary (EOP) void ratio-effective stress relationship, *Proc. 11th ICSMFE*, San Francisco, 2, 587-590.
Mesri, G., Shahien, M. and Feng, T.W. 1995. Compressibility parameters during primary consolidation, *Proc. Int. Symp. on Compression and Consolidation of Clayey Soils*, H.Yoshikuni and O.Kusakabe eds., Balkema, 2, 1021-1037.
Mitchell, J.K., Singh, A. and Campanella, R.G. 1968. Soil creep as a rate process, *J. Soil Mech. and Foundations Div.,* ASCE, 94, SM1, 231-253.
Mitchell, J.K. 1986. Practical problems from surprising soil behavior, 20th Terzaghi Lecture, ASCE, *J. Geotech. Engrg.*, 112(3), 259-289.
Mollema, P.M. and Antonellini, M.A. 1996. Compaction bands: A structural analog for anti-mode I cracks in aeolian sandstone, *Tectonophysics*, 267, 209-228.
Mühlhaus H.-B. 1986. Shear band analysis in granular materials by Cosserat theory, *Ing. Archiv.,* 56, 389-399.
Mühlhaus, H.-B. and Vardoulakis, I. 1987. The thickness of shear bands in granular materials. *Géotechnique,* 37, 271-283.
Mühlhaus, H.-B. and Aifantis, E.C. 1991. A variational principle for gradient plasticity, *Int. J. Solids and Structures,* 28(7), 845-857.
Mühlhaus, H.-B. and Oka, F. 1995. A continuum theory for random packings of elastic spheres, Fracture of Brittle and Disordered Materials, *Proc. IUTAM Symp. on Fracture of Brittle and Disordered Materials,* Concrete, Rocks and Ceramics, Brisbane, Australia, G.Baker and B.L.Karihaloo eds., E & FN Spon, 285-298.
Mühlhaus, H.-B. and Oka, F. 1996. Dispersion and wave propagation in discrete and continuous models for granular materials. *Int. J. Solids and Structures,* 33(19), 2841-2858.
Muir Wood, D. 2002. Some observations of volumetric instabilities in soils, *Int. J. Solids and Structures*, 39, 3429-3449.
Murayama, S. and Shibata, T. 1964. Flow and stress relaxation of clays, *Proc. IUTAM Symposium on Rheology and Soil Mech.*, J.Kravtchenko and P.M.Sirieys eds., Springer-Verlag, 99-129.
Murayama, S. 1983. Formation of stress-strain-time behavior of soils under deviatoric stress condition*, Soils and Foundations*, 23(2), 43-57.
Naghdi, P.M. and Trapp, J.A. 1975. Restrictions on constitutive equations of finitely deformed elastic-plastic materials. *Quarterly Journal of Mech. and Appl. Math.*, Vol.XXVII, Pt.1.
Nakai, T. and Mihara, Y., 1984. A new mechanical quantity for soils and its application to elasto-plastic constitutive models, *Soils and Foundations,* 24(2), 82-94.
Nemat-Nasser, S. 1983. On finite plastic flow of crystalline solids and geomaterials, Trans. of ASME, *J. Applied Mechanics*, 50, 1114-1126.
Nishi, K. and Esashi, Y. 1978. Stress-strain relationships of sand, *Proc. JSCE*, 280, 111-122.
Nishi, K. and Kanatani, M. 1990. Constitutive relations for sand under cyclic loading based on elasto-plasticity theory. *Soils and Foundations*, 30(2), 43-59.
Nova, R. 1982. A viscoplastic constitutive model for normally consolidated clay, *Proc. of IUTAM Conf. on Deformation and Failure of Granular materials,* P.A.Vermeer and H.J.Luger eds., Balkema, 287-295.
Nova, R. 1994. Controllability of the incremental response of soil specimens subjected to arbitrary loading programmes, *J. Mechanical Behaviour of Materials*, 5(2), 193-201.
Oda, M. and Kazama, H. 1998. Micro-structure of shear band and its relation to the mechanism of dilatancy and failure of granular soils, *Géotechnique*, 48(1), 1-17.
Oka, F. 1981. Prediction of time-dependent behaviour of clay, *Proc. 10th Int. Conf. on Soil Mech. and Foundation Eng.,* 15-19 June, Stockholm, Balkema, 1, 215-218.
Oka, F. and Washizu, H. 1981. Constitutive equations for sand and overconsolidated clays, *Proc. Int. Conference on Recent Advances in Earthquake Engineering and Soil Dynamics*, St. Louis, S.Prakash ed., 1, 71-74.
Oka, F. 1982. Constitutive equations for granular materials in cyclic loadings. *IUTAM Conference on Deformation and Failure of Granular Materials*, Delft, P.A.Vermeer and H.J.Luger eds., Balkema, 297-306.
Oka, F. 1985. Elasto/viscoplastic constitutive equations with memory and internal variables, *Computers and Geotechnics*, 1, 59-69.
Oka, F. and Adachi, T. 1985. A constitutive equation of geologic materials with memory, *Proc. 5th Int. Conf. on Numerical Method in Geomechanics*, Balkema, 1, 293-300.
Oka, F., Adachi, T. and Okano, Y. 1986. Two-dimensional consolidation analysis using an elasto-viscoplastic constitutive equation, *Int. J. Numerical and Analytical Methods in Geomechanics*, 10, 1-16.
Oka, F. 1988. The validity of the effective stress concept in soil mechanics, Micromechanics of Granular Materials, Studies in Applied Mechanics, 20, *Proc. U. S./Japan Seminar on the Micromechanics of Granular Materials*, Sendai, Japan, Oct. 1987, M.Satake and J.T.Jenkins eds., Elsevier Sci. Pub., 207-214.
Oka, F., Leroueil, S. and Tavenas, F. 1991. An elasto-viscoplastic FEM analysis of sensitive clay foundation beneath embankment, *Proc. 7th International Conference on Computer Methods and Advances*

in Geomechanics, Cairns, G.Beer, J.R.Booker and J.P.Carter eds., Balkema, 2, 1023-1028.
Oka, F., 1992. A cyclic elasto-viscoplastic constitutive model for clay based on the non-linear-hardening rule, *Proc. 4th International Symposium on Numerical Models in Geomechanics*, Swansea, G.N.Pande and S.Pietruszczak eds., Balkema, 1, 105-114.
Oka, F., Yashima, A. and Kato, M. and Sekiguchi, K. 1992a. A constitutive model for sand based on the non-linear kinematical hardening rule and its application, *Proc. 10th World Conference on Earthquake Engineering*, Madrid, Balkema, 2529-2534.
Oka, F., Yashima, A., and Kohara, I. 1992b. A finite element analysis of clay foundation based on finite elasto-viscoplasticity., *Proc. 4th Int. Symposium on Numerical Models in Geomechanics*, Swansea, UK, G.N.Pande, and S.Pietruszczak eds., Balkema, 915-922.
Oka, F. 1993a. An elasto-viscoplastic constitutive model for clay using a transformed stress tensor, *Mechanics of Materials*, 16, 47-53.
Oka, F. 1993b. Anisotropic and pseudo-anisotropic elasto-viscoplastic constitutive models for clay, Modern Approaches to Plasticity, P*roc. of a Workshop held in Horton*, June 1992, D.Kolymbas ed., Elsevier Sci. Pub., 505-526.
Oka, F., Yashima, A. and Kato, M. 1993c. Numerical analysis of wave-induced liquefaction in seabed. *Proc. 3rd Int. Offshore and Polar Engineering Conf*., Singapore, 6-11 June, 591-598.
Oka, F., Yashima, A., Kato, M. and Goto, H. 1993d. A modified constitutive model for sand based on non-linear kinematic hardening rule. *Proc. of 28th Annual Meeting on SMFE*, Kobe, 489-490 (in Japanese).
Oka, F., Yashima, A., Kato, M. and Nakajima, Y. 1994a. An analysis of seepage failure using an elasto-plastic constitutive equation and its application. *Journal of JSCE*, 493, III-27, 127-135 (in Japanese).
Oka, F., Yashima, A., Shibata, T., Kato, M., and Uzuoka, R. 1994b. FEM-FDM coupled liquefaction analysis of porous soil using an elasto-plastic model, *Applied Scientific Research*, 52, 209-245.
Oka, F., Adachi, T., Yashima, A. and Chu, L.L. 1994c. Strain localization analysis by elasto-viscoplastic softening model for frozen sand, *Int. J. Numerical and Analytical Methods in Geomechanics,* 18, 813-832.
Oka, F., Adachi, T. and Yashima, A. 1994d. Instability of an elasto-viscoplastic constitutive model for clay and strain localization. *Mechanics of Materials,* 18, 119-129.
Oka, F. and Yashima, A. 1995. A cyclic elasto-viscoplastic model for cohesive soil, *Proc. XI European Conference on Soil Mechanics and Foundation Engineering, Copenhagen,* The Danish Geotechnical Society, 6, 6.145-6.150.
Oka, F., Adachi, T. and Yashima, A. 1995. A strain localization analysis using a viscoplastic softening model for clay. *Int. J. of Plasticity*, 11(5): 523-545.
Oka, F. 1996. Validity and limits of the effective stress concept in geomechanics, *Mechanics of Cohesive-Frictional Materials*, 1(2), 219-234.
Oka, F., Yashima, A., Tateishi, A., Taguchi, Y., Yamashita, S. 1999a. A cyclic elasto-plastic constitutive model for sand considering a plastic-strain dependence of the shear modulus, *Géotechnique*, 49(5), 661-680.
Oka, F. and Yashima, A. 1999b. Effect of soil improvement on liquefaction of man-made island, *Geotechnical Engineering for Transportation Infrastructure,* Barend et al. eds., *Proc. 12th ECSMGE*, Balkema, 2, 823-828.
Oka, F., Jiang, M., and Higo, Y. 1999c. Effect of transport of water on strain localization analysis of fluid-saturated strain gradient dependent viscoplastic geomaterial, *Proc. 5th Int. Workshop on Bifurcation and Localization*, Perth, Australia, H.-B.Mühlhaus, A.V.Dyskin, and E.Pasternak eds., Balkema, 77-83.
Oka, F. 2000. Elasto-viscoplastic constitutive models of geomaterials, Morikita Shuppan, p.103 (in Japanese).
Oka, F., Sugito, M., Yashima, A., Furumoto, Y. and Yamada, K. 2000a. Time-dependent ground motion amplification at reclaimed land after the 1995 Hyogo-Ken-Nanbu Earthquake, *Proc. 12th WCEE*, Paper No. 2046.
Oka, F., Yashima, A., Sawada, K. and Aifantis, E.C. 2000b. Instability of gradient-dependent elastoviscoplastic model for clay and strain localization. *Computer Methods in Applied Mechanics and Engineering ,* 183, 67-86.
Oka, F. 2001. *Liquefaction of Ground*, Kinmiraisha Book Company, Nagoya, 58-63 (in Japanese).
Oka, F., Kodaka, T., Koizumi,T. and Sunami, S. 2001. An effective stress based liquefaction analysis based on finite deformation theory, *Proc. 10th IACMAG*, Tucson Arizona, C.S.Desai et al. eds., Balkema, 1113-1116.
Oka, F. 2002. A liquefaction analysis method based on finite deformation theory using a cyclic elasto-plastic model for sand, *Proc. of 5th WCCM*, Vienna, Austria, H.A.Mang, F.G.Rammerstorfer and J.Eberhardsteiner eds.
Oka, F., Lu, C.-W., Uzuoka, R. and Zhang, F. 2002a. Design method and performance of liquefaction problem liquefaction analysis of group-pile foundation-structure system, *Tsuchi-to-Kiso,* JGS, 50(8), Ser. No. 535, 9-11 (in Japanese).
Oka, F., Higo, Y., and Kimoto, S. 2002b. Effect of dilatancy on the strain localization of water-saturated elasto-viscoplastic soil. *International Journal of Solids and Structures*, 39(13-14), 3625-3647.
Oka, F., Kimoto, S., Kobayashi, H. and Adachi, T. 2002c. Anisotropic behavior of soft sedimentary rock and a constitutive model, *Soils and Foundations*, 42(5), 59-70.
Oka, F., Kodaka, T., Kimoto, S., Ishigaki, S. and Tsuji, C. 2003a. Step-changed strain rate effect on the stress-strain relations of clay and a constitutive modeling, *Soils and Foundations*, 43(4), 189-202.
Oka, F., Uzuoka, R. Tateishi, A. and Yashima, A. 2003b. A cyclic elasto-plastic model for sand ant its application to liquefaction analysis, Constitutive Modeling of Geomaterials, selected contributions from the Frank L. DiMaggio Symp., *Inelastic Behavior Committee Engineering Mechanics Division*, ASCE, CRC Press, 75-99.
Oka, F., Kodaka, T. and Kim, Y.-S. 2003c. A cyclic viscoelastic-viscoplastic constitutive model for clay and liquefaction analysis of multi-layered ground, *Int. J. Numerical and Analytical Methods in Geomechanics*, 28, 131-179.
Oka, F. et al. 2004a. Users manual of LIQCA2D04, http: //www.nakisuna2.kuciv.kyoto-u.ac.jp/liqca.htm.
Oka, F., Lu, C.-W. and Zhang, F. 2004b, Effects of liquefaction on the numerical analysis of a single pile-soil interaction during earthquakes, *Proc. 15th Int. Conf. on Case Histories in Geotechnical Engineering*, New York, S.Prakash ed., Paper No. 12A-8, April, 13-17.
Oka, F., Furuya, K. and Uzuoka, R. 2004c. Numerical simulation of cyclic behavior of dense sand using a cyclic elasto-plastic model, *Proc. Int. Symposium on Cyclic Behavior of Soils and Liquefaction Phenomena,* Th.Triantafyllidis ed., Balkema, 85-90.
Oka, F., Higo, Y., Kim, Y.-S., Imura, Y. and Kimoto, S. 2004d. Thermo-hydro-mechanically coupled finite element analysis of cohesive soil using an elasto-viscoplastic model, *COMPUTATIONAL MECHANICS* (Abstracts) *WCCM VI*, Beijing, China, Tsinghua University Press & Springer-Verlag, 266.
Oka, F., Kodaka, T. and Kim, Y.-S. 2004e. A cyclic viscoelastic-viscoplastic constitutive model for clay and liquefaction analysis of multi-layered ground, *Int. J. Numer. Anal. Meth. Geomech.*, 28, 131-179.
Oka, F., Lu, C.-W., Uzuoka, R. and Zhang, F. 2004f. Numerical study of structure-group pile foundations using an effective stress based liquefaction analysis method, *Proc. 13th WCEE*, Vancouver, Canada, August 1-6, Paper No.3338.
Oka, F., Kimoto, S., Kodaka, T., Takada, N., Fujita, Y. and Higo, Y. 2005a. A finite element analysis of the deformation behavior of multi-phase seabed ground due to the dissociation of natural gas hydrate, *Proc. 11th IACAMG*, to appear.
Oka, F., Kimoto, S., Kim, Y.-S., Takada, N. and Higo, Y. 2005b. A finite element analysis of the thermo-hydro-mechanically coupled problem of cohesive deposit using a thermo-elasto-viscoplastic model, *Proc. 3rd Biot conf.,* to appear.
Oka, F., Kodaka, T., Kimoto, S., Ichinose, T. and Higo, Y. 2005c. Strain localization of rectangular clay specimen under undrained triaxial compression conditions, *Proc. 16th ICSMGE*, Osaka.
Oka, F., Kimoto, S. and Adachi, T. 2005d. Calibration of elasto-viscoplastic models for cohesive soils, *Proc. 11th IACMAG*, to appear.
Oliver, J., Cervera, M., and Manzoli, O. 1999. Strong discontinuities and continuum plasticity models: the strong discontinuity approach. *Int. J. Plasticity,* 15, 319–351.
Olsson, W.A. 1999. Theoretical and experimental investigation of compaction bands in porous rock, *J. Geophysical Res.*, 104, B4, 7219-7228.
Palmer, A.C. and Rice, J. 1973. The growth of slip surfaces in the progressive failure of overconsolidated clay, *Proc. Roy. Soc. London,* A269, 500-527.
Papamichos, E. and Vardoulakis, I. 1995. Shear band formation in sand according to non-coaxial plasticity model, *Géotechnique*, 45(4), 649-661.
Pastor, M. and Zienkiewicz, O.C. 1986. A generalized plasticity, hierarchical model for sand under monotonic and cyclic loading. *Proc.of*

2nd Int. Sym. on Numerical Models in Geomechanics, G.N.Pande and W.F.Van Impe eds., M.Jackson & Son, 131-150.
Pastor, M., Zienkiewicz, O.C. and Chan, A.C. 1990. Generalized Plasticity and the Modelling of Soil Behavior. *Int. J. Numer. Anal. Methods Geomech.*, 14, 151-190.
Peirce, D., Shih, C., and Needleman, A. 1984. A tangent modulus method for rate dependent solids. *Computers and Structures*, 18(5), 845-887.
Perrin, G. and Leblond, J.B. 1993. Rudnicki and Rice's analysis of strain localization revisited, J. *Applied Mechanics*, 60, 842-846.
Perzyna, P. 1963. The constitutive equations for work-hardening and rate sensitive plastic materials, *Proc. Vibrational Problems*, Warsaw, 4(3), 281-290.
Phillips, A. and Wu, H.-C. 1973. A theory of viscoplasticity, *Int. J. Solids and Structures,* 9, 15-30.
Poorooshasb, H.B. and Holubec, I. and Scherbourne, A.N. 1966. Yielding and flow of sand in triaxial compression: Part I, *Canadian Geotechnical Journal*, 3(4), 179-190.
Poorooshasb, H.B. and Holubec, I. and Scherbourne, A.N. 1967. Yielding and flow of sand in triaxial compression: Part II and Part III, *Canadian Geotechnical Journal,* 4(4), 376-397.
Pradhan, T.B.S. and Tatsuoka, F. 1989a. On stress-dilatancy equations of sand subjected to cyclic loading. *Soils and Foundations*, 29(1) 65-81.
Pradhan, T.B.S., Tatsuoka, F. and Sato, Y. 1989b. Experimental stress-dilatancy relations of sand subjected to cyclic loading, *Soils and Foundations*, 29(1), 45-64.
Prandtl, L. 1920. Über die Harte plashecher Körper, Nachr. *Math-phys.* KL. Gottingen, 74.
Prévost, J. 1982. Nonlinear transient phenomena in saturated porous media, *Computer Methods in Applied Mechanics and Engineering*.
Prévost, J.H. and Keane, C.M. 1990. Multi-Mechanism Elasto-Plastic Model for Soils. *J. Eng. Mech.*, ASCE, 116, EM9, 1924-1944.
Prévost, J.H. 1995. DYNAFLOW: A nonlinear transient finite element analysis program. Technical report, Dept. of Civil Eng. and Op. Research, Princeton University, Princeton, NJ.
Regueiro, R. and Borja, R. 2001. Plane strain finite element analysis of pressure sensitive plasticity with strong discontinuity, *Int. J. Solids and Structures*, 38, 3647-3672.
Rice, J.R. 1975. On the stability of dilatant hardening for saturated rock masses. *J. Geophys. Res.*, 80(11), 1531-1536.
Rice, J.R. 1976. The localization of plastic deformation, *Proc. 14th Int. Congress on Theoretical and Applied Mechanics*, W.T.Koiter ed., North-Holland, 207-220.
Roscoe, K.H., Schofield, A.N. and Thrairajah, A. 1963. Yielding of clays in states wetter than critical, *Géotechnique*, 13(3), 211-240.
Roscoe, K.H., Burland, J.B. 1968. On the generalised stress-strain behaviour of 'wet' clay, *Engineering plasticity (Cambridge: Cambridge University Press*), J.Heyman and F.A.Leckie eds., 535-609.
Roscoe, K.H. 1970. The influence of strains in soil mechanics, *Géotechnique,* 20(2), 129-170.
Rudnicki, J.W and Rice, J.R. 1975. Condition for the localization of deformation in pressure-sensitive dilatant material. *J. Mech. Phys. Solids*, 23, 371-394.
Rudnicki, R.W. and Olsson, W.A. 1998. Reexamination of fault angles predicted by shear localization theory, *Int. J. Rock Mech. Min. Sci*., 35 (4/5), 512-513.
Sawada, K., Yashima, A. and Oka, F. 2001. Numerical analysis of deformation of saturated clay based on Cosserat type elasto-viscoplastic model, J. of the Society of Material Science Japan, 50, 6, 585-592 (in Japanese).
Schrefler, B.A., Majorana, C.E. and Sanavia, L. 1995. Shear band localization in saturated porous media. *Arch. Mech.* 47(3), 577-599.
Schrefler, B.A., Sanavia, L. and Majorana, C.E. 1996. A multiphase medium model for localization and postlocalization simulation in geomaterials. *Mech. Cohesive-Frictional Materials,* 1, 95-114.
Scott, R.F. 1987. Failure, *Géotechnique*, 37(4), 423-466.
Sekiguchi, H. 1977. Rheological characteristics of clays, *Proc. 9th ICSMFE*, 1, Tokyo, 289-292.
Sekiguchi, H. and Ohta, H. 1977. Induced anisotropy and time dependency in clays, 9th ICSMFE, *Proc. Specialty Session 9*, Tokyo, 229-238.
Shibata, T., Oka, F., Yashima, A., Goto, H., Goto, K. and Takezawa, K. 1992. A numerical simulation of shaking table test of coal fly ash deposit with cement mixing column. *Numerical Models in Geomechanics*, G.N.Pande and S.Pietruszczak eds., Balkema, 411-420.
Shibata, T., Oka, F. and Ozawa, Y. 1996. Characteristics of ground deformation due to liquefaction, *Soils and Foundations,* Special issue on Geotechnical Aspects of the Jan. 17 1995 Hyogoken-Nambu Earthquake, 65-79.
Simon, B.R., Zienkiewicz, O.C. and Paul, D.K. 1984. An analytical solution for the transient response of saturated porous elastic solids, *Int. J. Num. Anal. Meth. Geomech.*, 8, 381-398.
Singh, A. and Mitchell, J.K. 1968. General stress-strain-time function for soils, *J. Soil Mechanics and Foundation Engng.,* ASCE, 94, SM1, 21-46.
Singh, A. and Mitchell, J.K. 1969. Creep potential and creep rupture of soils, *Proc. 7th ICSMFE,* Mexico, 379-384.
Siribumrungwong, B., Oka, F., and Kimoto, S. 2004. Numerical study of the effect of degradation on bearing capacity of clay using an elasto-viscoplastic model, *Proc. of 17th KKCNN Symposium on Civil Engineering*, December 13-15, 2004, Thailand, 589-594.
Sokolovsky, V.V. 1942. *Statics of earthy media* (Russian), Moscow, Izdatelstiv Akademii Nauk.
Spencer, A.J.M. 1964. A theory of the kinematics of ideal soils under plane strain conditions, *J.Mech. Phys. Solids,* 12, 337-351.
Spencer, A.J.M. 1987. Isotropic polynominal invariants and tensor functions, *Applications of tensor functions in solid mechanics*, J.P.Boehler ed., Springer, 141-164.
Sugito, M., Oka, F., Yashima, A., Furumoto, Y. and Yamada, K. 2000. Time-dependent ground motion amplification characteristics at reclaimed land after the 1995 Hyogoken Nambu Earthquake, *Engineering Geology,* 56, 137-150.
Suzuki, Y., Hatanaka, M. and Uchida, A. 1997. Drained and undrained shear strengths of a gravelly fill of weathered granite from Kobe Port Island. J. Struct. Constr. Eng., AIJ, 498, 67-73 (in Japanese).
Taguchi, Y., Tateishi, A., Oka, F., and Yashima, A. 1995. A cyclic elasto-plastic model for sand based on generalized flow rule and its application, *Proc. 5th Int. Symp. on Numerical Models in Geomech.,* G.N.Pande and S.Pietruszczak eds., Balkema, Davos, 57-62.
Taguchi, Y., Tateishi, A., Oka, F., and Yashima, A. 1996. Three-dimensional liquefaction analysis method and array record simulation in great hanshin earthquake, *11th World Conference on Earthquake Engineering,* Acapulo, Sociedad Mexicana de Ingenieria Sismica, Balkema (CD-ROM), Paper No. 1042.
Taguchi, Y., A. Tateishi, Oka, F. and Yashima, A. 1997. Numerical simulation of soil-foundation interaction behavior during subsoil liquefaction, *Proc. 6th Int. Symp. on Numerical Models in Geomechanics*, S.Pietruszczak and G.N.Pande eds., Balkema, 561-566.
Tamaganini, R., Viggiani, G. and Chambon, R. 2001. Some remarks on shear band analysis in hypoplasticity, *Bifurcation and localization theory in geomechanics*, H.B. Mühlhaus, A.V.Dyskin and E.Pasternak eds., Balkema, 85-93.
Tang, Y.X. and Imai, G. 1995. A constitutive relation with creep and its application to numerical analysis of one dimensional consolidation, *Int. Symp. on Compression and Consolidation of Clayey Soils*, H.Yoshikuni and O.Kusakabe eds., Balkema, 1, 465-472.
Tatsuoka, F., Nakamura, S., Huang, C.C. and Tani, K. 1990. Strength anisotropy and shear band direction in plane strain tests of sands, *Soils and Foundations*, 30(1), 35-54.
Tatsuoka, F., Di Benedetto, H. and Ishihara, M. 2002. Time-dependent shear deformation characteristics of sand and their constitutive modeling, *Soils and Foundations*, 42(2), 1-22.
Tavenas, F., Chapeau, C., LaRochell, P. and Roy, M. 1974. Immediate settlements if three test embankments on Champlain clay, *Can. Geotech. J.*, 11(1), 109-141
Tavenas, F., Mieussens, C. and Bourges, F. 1979. Lateral displacements in clay foundations under embankments, *Can. Geotech. J.*, 16, 532-550.
Taylor, D.W. 1948. *Fundamentals of Soil Mechanics*, John Wiley & Sons.
TC34 of ISSMGE. 2005. The State-of-the-Art report, Prediction methods in large strain geomechanics, *Proc. 16th ICSMGE*, Osaka September 2005.
Teichman, J. and Wu, W. 1993. Numerical study of patterning of shear bands in a Cosserat continuum, *Acta Mechanica*, 69, 61-74.
Thornton, C. 1998. Numerical simulations of deviatoric shear deformation of granular media, *Géotechnique,* 50(2), 43-53.
Tokuoka, T. 1971. Yield conditions and flow rules derived from hypo-elasticity, *Arch. Rat. Mech. Anal*., 42, 239-252.
Uzuoka, R. 2000. Analytical study on the mechanical behavior and prediction of soil liquefaction and flow, Doctor of Engineering, Dissertation, Department of Civil Engineering, Gifu Univ., Gifu, Japan. 49- 76 (in Japanese).
Uzuoka, R., Sento, N., Yashima, A. and Zhang, F. 2001a. 3-dimensional effective stress analysis of damaged pile foundation adjacent to quay wall, *Journal of JAEE*, 1-14 (in Japanese).

Uzuoka, R., Kubo, T., Yashima, A. and Zhang, F. 2001b. 3-dimensional effective stress analysis of damaged pile foundation during the 1995 Hyogoken-Nambu earthquake, *Proc. of 36th Japan National Conference on Geotechnical Engineering*, 1727-1728 (in Japanese).

Vaid, Y.P. and Campanella, R.G. 1977. Time-dependent behaviour of undisturbed clay, *J. Geotech. Engng.*, ASCE, 103, GT7, 693-709.

Valanis, K.C. 1971. A theory of viscoplasticity without a yield surface, *Arch. Mech. Stos.,* 23(4), 517-533.

Valdoulakis, I. 1977. Scherfugenbildung in Sandkörpern als Verzweigunsproblem.Dissertation, Universität Karlsruhe, Veröffentlichungen IBF, Heft Nr. 70.

Vardoulakis, I. 1980. Shear band inclination and shear modulus of sand in biaxial tests, *Int. J. Num. Anal. Meth. in Geomechanics,* 4, 103-119.

Vardoulakis, I. and Aifantis, E.C. 1991. A gradient flow theory of plasticity for granular materials, *Acta. Mech.*, 87, 197-217.

Vardoulakis, I. and Sulem, J. 1995. *Bifurcation analysis in geomechanics*, Glasgow, Blackie.

Vardoulakis, I. 1996a. Deformation of water-saturated sand:I uniform undrained deformation and shear banding, *Géotechnique*, 46(3), 441-456.

Vardoulakis, I. 1996b. Deformation of water-saturated sand:II effect of pore water flow and shear banding, *Géotechnique*, 46(3), 457-472.

Vardoulakis, I. 2002. Dynamic thermo-poro-mechanical analysis of catastrophic landslides, *Géotechnique*, 52(3), 157-171.

Vermeer, P. 1978. A double hardening model for sand, *Géotechnique*, 28(4), 413-433.

Vermeer, P. 1982. A simple shear band analysis using compliance, *Proc. IUTAM Conference on Deformation and Failure of Granular Materials*, P.A.Vermeer and H.J.Luger eds., Balkema, 493-499.

Wheeler, S.J. and Karube, D. 1995. Constitutive modeling, *Proc. 1st Int. Conf. on unsaturated soils*, Paris, E.E.Alonso and P.Delage eds., 1323-1356.

Wu, W. and Bauer, E. 1994. A simple hypoplastic constitutive model for sand, *Int. J. Num. Anal. Meth. in Geomechanics*, 18, 833-862.

Yashima, A., Leroueil, S., Oka, F. and Guntoro, I. 1998. Modelling temperature and strain rate dependent behavior of clays: one dimensional consolidation, *Soils and Foundations*, 38(2), 63-73.

Yashima, A., Shigematsu, H., Oka, F. and Nagaya, J. 1999. Mechanical behavior and microstructure of Osaka upper-most pleistocene marine clay, *J. Geotechnical Engng.,* JSCE, 624, III-47, 217-229 (in Japanese).

Yashima, A., Oka, F. and Kanami, H. 2000. 3-D analysis to evaluate the effect of soil improvement on liquefaction of man-made island, *Proc.12th WCEE,* Paper No.2116.

Yatomi, C., Yashima, A., Iizuka, A., and Sano, I. 1989. General theory of shear bands formation by a non-coaxial Cam-clay model. *Soils and Foundations*, 29(3), 41-53.

Yin, J.-H., and Graham, A. 1999. Elastic visco-plastic modeling of time-dependent stress-strain behaviour of soils, *Canadian Geotechnical Journal*, 34(4), 736-745.

Yong, R.N. and Yapp, R.D. 1969. Stress-strain behavior of clays in dynamic compression, *Vibration effects of earthquakes on soils and foundations*, ASTM, STP450, 233-262.

Zhang, H.W., Sanavia, L. and Schrefler, B.A. 1999. An internal length scale in dynamic strain localization of multiphase porous media. *Mechanics of Cohesive-Frictional Materials*, 4, 443-460.

Zhang, H.W. and Schrefler, B.A. 2000. Gradient-dependent plasticity model and dynamic strain localization analysis of saturated and partially saturated porous media: one dimensional model, *European Journal of Mechanics A/Solids*, 19(3), 503-524.

Zhang, H.W. and Schrefler, B.A. 2001. Uniqueness and localization analysis of elasto-plastic saturated porous a, *Mechanics of Cohesive-Frictional Materials*; 25, 29-48.

Zhang, F. and Kimura, M. 2002. Numerical prediction of the dynamic behaviors of an RC group-pile foundation, *Soils and Foundations*, 42(3), 77-92.

Zhang, F., Kimura, M. and Lu, C.-W. 2002. 3-D dynamic finite element analysis on group-pile foundation based on an axial-force dependent model for RC, *Proc. of Numerical Methods in Geotechnical Engineering*, Paris, P.Mestat ed., Balkema, 1009-1016.

Zienkiewicz, O.C., Humpheson, C. and Lewis, R.W. 1975. Associated and non-associated viscoplasticity and plasticity in soil mechanics, *Géotechnique*, 25(4), 671-689.

Zienkiewicz, O.C., Chang, C.T. and Bettess, P. 1980. Drained, undrained, consolidating and dynamic behaviour assumptions in soils, *Géotechnique*, 30(4), 385-395.

Zienkiewicz, O.C. 1982. Field equations for porous media under dynamic loads, *Num. Meth. in Geomechancis*, D.Reidel, Boston, USA.

Zienkiewicz, O.C. and Shiomi, T. 1984. Dynamic behaviour of saturated porous media:The generalized Biot formulation and its numerical solution, *Int. J. Num. Anal. Meth. Geomech*., 8, 71-96.